DEVELOPMENT AND APPLICATIONS OF FEATURE-GUIDED CARDIAC MOTION ESTIMATION METHOD FOR 4D CARDIAC PET

by

Jizhe Wang

A dissertation submitted to Johns Hopkins University in conformity with the requirements for the degree of Doctor of Philosophy

Baltimore, Maryland

July, 2016

❖ Abstract

The aim of this dissertation research is to develop, implement and evaluate methods to extract useful information about cardiac motion and myocardial contractility from 4D cardiac PET images with much improved image quality.

First, to reduce the influence of respiratory motion and improve the quality of cardiac PET images used in motion estimation, data-driven respiratory gating methods are proposed to allow accurate extraction of respiratory motion signal from the list-mode data. Time-of-flight PET information is incorporated into respiratory signal extraction, and background correction method is developed to improve the quality and accuracy of the extracted respiratory signal. The methods were applied and evaluated using clinical list-mode cardiac PET data.

With improved image quality, anatomical feature such as papillary muscles and the interventricular sulcus become increasingly detectable in gated cardiac PET images. For more accurate cardiac motion estimation, these anatomical features in human heart were extracted and used in combination with *a priori* knowledge of cardiac function to guide the cardiac motion estimation process. Initial estimates of the cardiac motion vector field were obtained based on the motion of the features for the traditional optical-flow algorithm. For further improvement, motion of the anatomical feature was used as additional constraint in the motion estimation algorithm to reduce the effect of the classical aperture problem. Different from previous cardiac motion extraction and estimation studies that only provide qualitative evaluation of the motion estimation results due to unavailability of ground truth for clinical cardiac datasets, this study employed simulation data from a realistic digital phantom with known cardiac motion for both qualitative and quantitative evaluation. Motion estimation results from simulation data indicate the feature-based cardiac motion estimation method is able to improve the accuracy of the cardiac motion field estimates, especially for motion components parallel to edges and therefore difficult to estimate using the conventional optical-flow based method.

The proposed research will allow PET imaging to provide unprecedented cardiac motion information in addition to its functional information thus improving diagnosis of cardiac diseases including perfusion and

motion abnormalities, and patient care with reduced cost. Also, more accurate estimation of cardiac motion will help to further improve the quality of 4D cardiac PET imaging with cardiac motion compensation.

Advisor: Dr. Benjamin M.W. Tsui (first reader)

Second reader: Dr. Jingyan Xu

❖ Preface

Having been a PhD candidate in JHU since 2011, I am happy as well as reluctant to say goodbye. During my five years in DMIP, I have been working on several interesting research projects, from which I benefit a lot.

I would like to express my deepest gratitude to my advisor, Dr. Benjamin Tsui, for his profound knowledge of medical imaging, excellent teaching skills, and patience. I have learnt a lot from him more than I could elaborate. I would like to thank Dr. Xu and Dr. Fung for the support and guidance for my research. They have been very kind to me especially when I encounter problems. DMIP has provided an active and friendly research environment for me, and I am very grateful for this opportunity. Many thanks to all the members who have provide very good suggestions and discussions on my research topics.

I would also like to thank my parents who are supportive even though they are on the other side of the ocean. It is a shame that I cannot spend more time with them during my PhD years. Moreover, I am very lucky to meet my husband Tao Feng in DMIP. It is nice to have company on this difficult journey.

CONTENTS

LIST OF FIGURES

LIST OF TABLES

CHAPTER 1. INTRODUCTION

1. OVERVIEW

As an important functional imaging technique, positron emission tomography (PET) produces three-dimensional information of the functional processes in the body. PET has been widely used in medical practices and for research purpose. Its application in medical area includes clinical oncology, clinical diagnosis of brain diseases, as well as heart function. Besides, it also helps the development and evaluation of new drugs and radioactive tracers.

In PET imaging procedure, certain amount of biologically active molecule labeled with positron-emitting radionuclide, also called radioactive tracer, is introduced into the body. The chemical compound participates in certain biochemical reactions such as those involved in metabolic processes of the cells. Therefore, its distribution in different organs and tissues reveals the functional condition of the body. The radioisotope undergoes positron emission decay, also known as positive beta decay, during which a positron is emitted. Two photons, each with 511 KeV energy, are generated when the positron annihilates with an electron, and travel in the opposite direction until being detected by the scanner simultaneously as one coincidence, which identifies a line-of-response (LOR). The LORs from all the coincidence events will form the projection data for image reconstruction. The PET data is often acquired in list-mode format, which is event-by-event data acquisition that contains both spatial and timing information. It can also be stored in sinograms or projections by binning the events in the same LOR.

Image reconstruction is required to calculate the distribution of the radioactive tracer from list-mode or sinogram data. Analytical image reconstruction methods such as filtered back projection (FBP) use the analytical model of the scanner to recover the activity distribution. Although being fast and simple to implement, analytical methods have difficulty handling the noise and other image quality degrading factors as scatter and detector response. On the other hand, statistical image reconstruction methods, which often require iterative calculation such as maximum likelihood expectation maximization (ML-EM) and ordered subset expectation maximization (OS-EM), are based on the statistical model of the imaging process. This

group of methods provides more accurate modeling of resolution degradation factors and has stronger noise handling ability.

With the development of high resolution PET imaging systems and advance in image reconstruction algorithms, PET images of higher resolution are becoming available, which lays the foundation for this research.

2. PET SYSTEMS

INSTRUMENTATION

The common configuration followed by most human PET imaging systems for research and clinical purpose consists of gamma photon detector rings, electronics for pulse processing and coincidence detection, and image reconstruction module, as demonstrated in Figure 1-1. The detector rings are an annulus of scintillation detectors surrounding the patient body in order to detect pairs of 511 KeV gamma photons in coincidence. The rings typically have an inner diameter of 85-90 cm, and an axial coverage of 15-25 cm. The rings are comprised by several blocks of detectors each containing a segmented block of scintillating crystals coupled to an array of photomultiplier tubes (PMTs) which together generate electrical signal for incoming gamma photons. The gamma photons excite free electrons in the crystal through Compton scattering and photoelectric effect. Scintilator materials commonly used in PET scanners include Luterium Oxyorthosilicate (LSO), Bismuth germinate (BGO) and Sodium Iodide (NaI). When the excited electrons return to lower energy state, visible light photons are generated and then collected by the PMTs coupled to the end of the crystal. Light signals are transformed to electrical signal and amplified by the PMTs. Signals from the PMTs provide information about the position, energy and time of a gamma ray interaction in the scintillator.

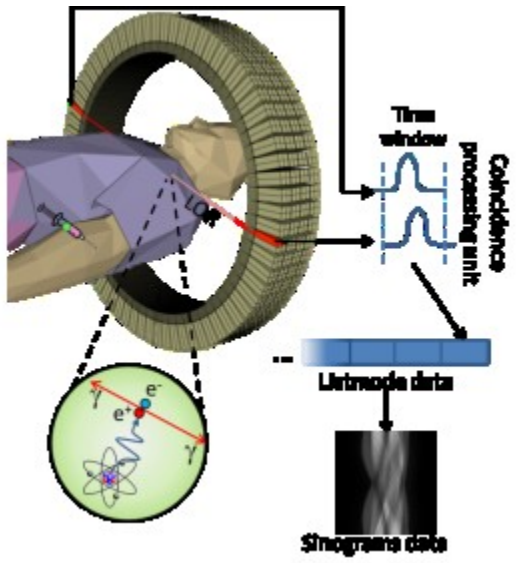

Figure 1-1 Illustration of a PET imaging system

Current improvement in the hardware of PET imaging systems includes development of better crystals with desirable properties such as strong stopping power, high light output, good energy resolution, and short decay time. There is also a trend towards excellent time resolution by introducing the "time-of-flight" (TOF) technique, which allows accurate measurement of the time difference between the arrival of the photon pair. With this information, the location of annihilation can be identified with higher accuracy, leading to higher system resolution. A typical TOF resolution of 500 ps can be achieved by current TOF PET scanners. The acquisition time for the whole body using clinical PET scanner is usually less than 20 min, while a cardiac scan takes around 5-10 min.

PET DATA FORMAT

There are two data formats to store the information of detected coincidences. One is the list-mode acquisition, in which the information of the event including energy, ring number, detector bin, etc., are all recorded one event by one event sequentially. Time stamps and Electrocardiography (ECG) signal used for cardiac gating are also recorded in the list-mode data. Therefore, the list-mode PET data require large storage size. On the other hand, the sinogram format stores the PET data by summing all the events in the same LOR. A typical sinogram of 3D PET is shown in Figure 1-2, in which each voxel represents the summation of all events with the same specific detector bin number, angle, and detector ring number. List-

mode format contains more information such as time and energy than the sinogram format. Therefore, transforming the list-mode data into sinogram format is feasible but the not the reverse. TOF information can be preserved from list-mode to sinogram format with specially designed rebinning algorithms.

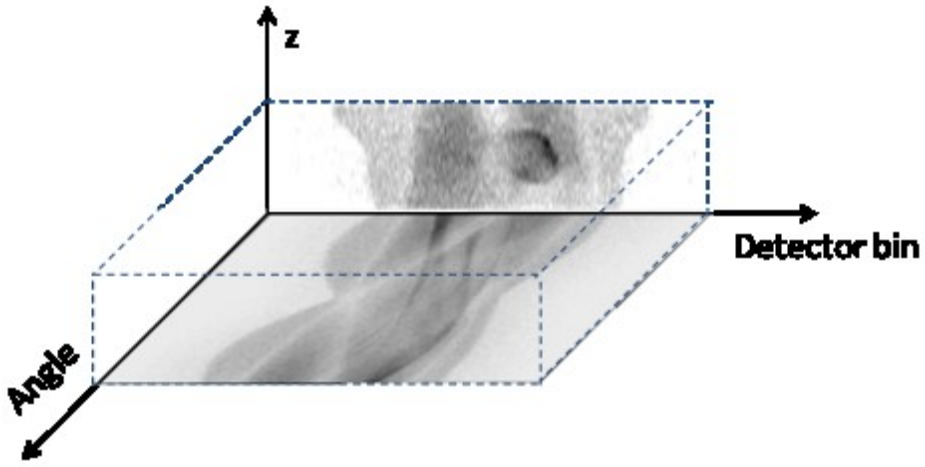

Figure 1-2 Illustration of 3D sinogram

MULTIMODALITY IMAGING SYTEM

A rapidly growing field of research in medical imaging is the development of multimodality imaging systems. PET/CT and PET/MR systems were designed and became clinically available in the 20 years. The integration of PET and CT in one system is relatively simple. In current commercial PET/CT scanners, essentially unmodified standalone PET and CT scanners are mounted in-line in a common gantry, which allows sequential acquisition of spatially registered PET and CT data. Attenuation map can be derived from the CT image for attenuation correction for PET data, which obviate the need for lengthy transmission scans. Since the CT scan takes negligible time compared with the PET acquisition, PET/CT scanners have similar or even better patient throughput.

Unlike simple the PET/CT integration, the system integration of PET and MRI is more challenging, especially for simultaneous PET/MRI system. The major challenge is to redesign a compact and MRI-compatible PET scanner so that its performance is not significantly degraded by the magnetic field from the MRI scanner. Solid-state photodetectors have been introduced to substitute PMT, which can severely influenced in even a weak magnetic field. Conversely, the introduction of PET detectors inside the gradient coil and magnet of the MRI scanner also introduce undesirable influences to the MRI acquisition.

Shielding and use of MRI compatible scintillators are possible solutions, but there is still no method to cancel the interference between two systems completely.

Compared with PET/CT, PET/MR is more advantageous in that the both spatially and temporally co-registered MR image to improve the quality of PET data, while the snap-shot CT and blurred PET result in attenuation activity mismatch. However, in applications such as staging lung cancer, PET/CT is a better choice since MRI performs poorly in the lungs.

3. PHYSICS IN PET IMAGING

RADIATION PHYSICS

POSITRON DECAY AND POSITRON-ELECTRON ANNIHILATION

Radioisotope ${}^{A}_{Z}X$ used in PET imaging releases positron e^+ during the beta decay:

$$ {}^{A}_{Z}X \rightarrow {}^{A}_{Z-1}X' + e^+ + v_e $$

1-1

The positron is the antimatter counterpart of the electron with an positive charge of $+1\,e$ and the same mass as an electron. Annihilation occurs when the positron collides with an electron from the surrounding material, producing two (most case) or more gamma ray photons:

$$ e^- + e^+ \rightarrow \gamma + \gamma $$

1-2

This process obeys conservation of momentum and total energy. Therefore, the two gamma ray photons travel in the opposite direction and each has energy of 511 KeV.

INTERACTION OF GAMMA PHOTONS WITH MATERIAL

While traveling through the patient body and the detector crystals, the gamma photons interact with the material mainly in three ways. The first type of interaction happens between the gamma photon and the bounded orbital electrons of an atom in the absorbing material. During this interaction, the gamma photon deposits all its energy to the bounded electron so that the electron gains enough energy to break the binding

from the nuclide of the atom. The kinetic energy of the ejected electron is equal to the energy of the gamma photon, in PET 511 KeV, minus its binding energy. The possibility of photoelectric absorption is characterized by the following equation:

$$p \propto \frac{Z_{eff}^4}{E_r^3},$$

1-3

where E_r is the photon energy, and Z_{eff} is the effective atom number of the material.

The last two types of interaction happen between the gamma photon and the free electron in the material. One is Compton scattering in which the incident gamma photon transfers part of its energy to the electron and change motion direction. It is demonstrated in Figure 1-3. This process also obeys the conservation of energy and momentum. The relationship between the energy of the gamma photon after and before the Compton scattering is characterized by the following equation:

$$\frac{E_{\gamma\prime}}{E_\gamma} = \frac{1}{1+\frac{E_\gamma}{m_e c^2}(1-cos\theta)}.$$

1-4

In which m_e is the rest mass of an electron and θ is the scattering angle with respect to the incident direction. The probability of Compton scattering is approximately proportional to the density of free electron.

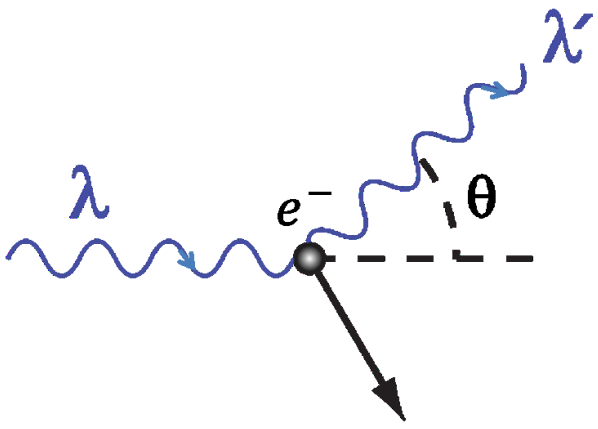

Figure 1-3 Compton scattering

Gamma photon can also interact with free electron through coherent scattering. It can be seen as a coherent collision in which the gamma photon changes travelling direction but does not loss energy.

All three types of interaction contribute to the attenuation of the gamma photon in the patient body. Compton scattering is the most prominent factor among three interaction types. However, photoelectric absorption becomes dominant after the energy of gamma photon reduces to around 20 KeV after multiple Compton scattering.

IMAGE DEGRADING FACTORS AND THEIR CORRECTION

POSITRON RANGE

The position emitted from beta decay has a small amount of momentum. It travels in the material and decelerates to nearly stationary before annihilate with an electron. As a result, there is a small distance in the range of 1~4mm [1], depending on the radioisotope, between the annihilation location and the beta decay location. Therefore, the reconstructed image is not exactly the distribution of the radiotracer, but the distribution of annihilation events. This intrinsically limits the spatial resolution of the PET scanner. The positron range can be reduced by applying a strong magnetic field [2]. Another approach is to correct for positron range and improve image resolution by modeling it in the reconstruction process [3, 4].

NON-COLLINEARITY

When the annihilation happens, the positron may not be stationary. The momentum left after traveling through the positron range is preserved by the two gamma photons. As a result, they do not travel in exactly 180 degree opposite. A study by K. Shibuya [5] showed the distribution of the difference angle was approximately a Gaussian distribution with FWHM of 0.54 degree centered at 180 degree, resulting in ~2.1mm for a system with scanner diameter being 80 cm. Positron range and non-collinearity are demonstrated by the following figure.

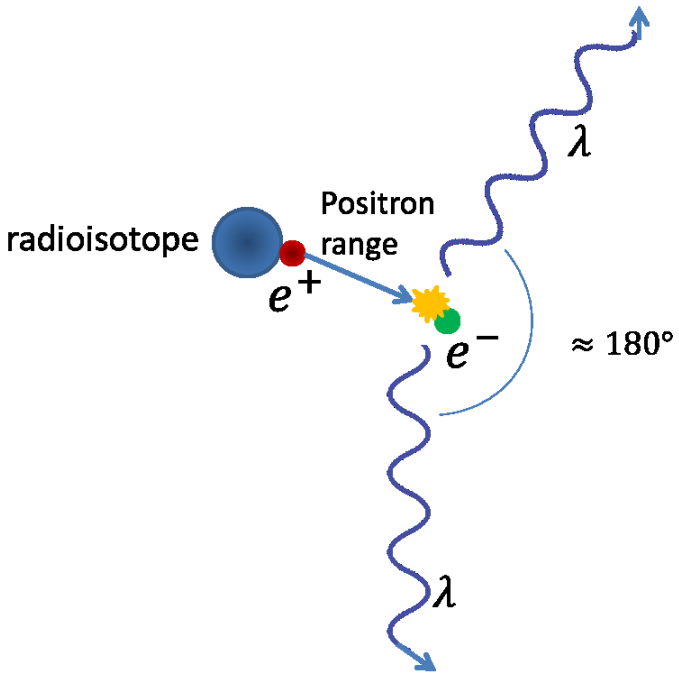

Figure 1-4 Positron range and non-collinearity

ATTENUATION

The interaction of the gamma photon with the patient body reduces the possibility of this photon being able to escape the body and arrive at the detector. The reduction in this probability is called attenuation. The ability of the material to absorb the passing photon is characterized by the attenuation coefficient. The attenuation of a pair of gamma photon is demonstrated by Figure 1-5. Using the narrow beam mono-energetic photon model, the attenuation of the gamma photon pair in the patient body can be calculated by the following equation:

$$P = P_1 \cdot P_2 = e^{-\int_0^{l_1} \mu(l) d\vec{l}} \cdot e^{-\int_0^{l_2} \mu(l) d\vec{l}} = e^{-\int_{-l_1}^{l_2} \mu(l) d\vec{l}}$$

1-5

In which P_1 and P_2 are the probabilities that photon 1 and 2 escape the patient body without being absorbed, $\mu(l)$ is the attenuation coefficient at location l, $\vec{l}$ is the line defined by the LOR. Therefore, for a fixed LOR, the attenuation effects does not depend on the exact location of annihilation, in this case, the attenuation effects can be compensated on the LOR prior to image reconstruction.

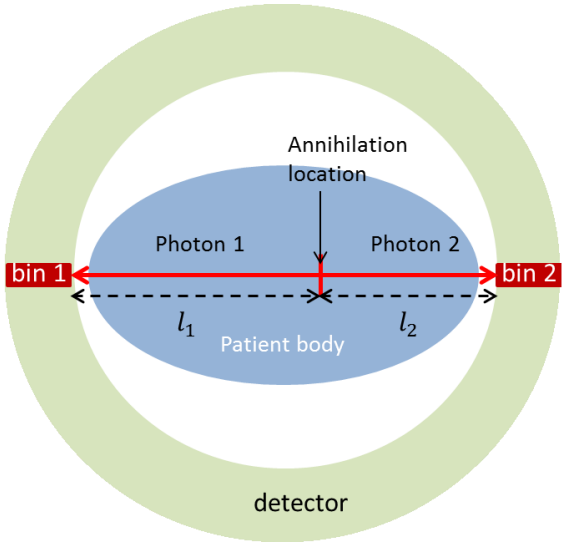

Figure 1-5 The attenuation of a pair of gamma photons in patient body

The attenuation of the gamma photon by patient body leads to underestimation of the radiotracer distribution. The essential idea of attenuation correction is to remove the attenuation factor in the equation using knowledge about the attenuation coefficient of the patient body. For 2D PET developed in early days, information of the attenuation is obtained by transmission emission scan. A rod source is rotated around the patient body inside the PET scanner, and the attenuation factors are measured from projection data to directly recover the original intensity for each LOR [6]. However, noise in the detected counts and the additional radiation dose from the rod source limits the application of this method. It is also inconvenient to use for 3D PET. Attenuation factor of the patient body required in attenuation correction of PET data can be obtained from other imaging modalities such as CT and MRI. Attenuation map for 511 KeV gamma photon can be directly derived from CT images[7], while it requires specially designed algorithm to calculate it from the anatomical information provided by MRI image [8, 9] since MRI does not measure the attenuation coefficient. Recent development of multimodality scanners such as PET/CT and PET/MR enables accurate co-registration of attenuation map and PET image, leading to more convenient attenuation correction and higher image quality.

RANDOM AND SCATTERED COINCIDENCE

PET imaging relies on the identification of photon path of the gamma photon pair. The coincidence detection circuits are designed specifically for this purpose. Two photons received by two detector bins

within the same timing window are regarded as one coincidence event. If they do come from the same annihilation and their paths are not changed by interaction with the body, this is called true coincidence. However, although the two gamma photons from one annihilation event do arrive at the detector rings almost simultaneously if not absorbed by the patient body, one or two of them may change direction and/or lose energy during their trip in the body. This situation is called scattered coincidence. Scatter coincidences are unable to provide correct information about the annihilation location. In another undesirable situation, the two or even more gamma photons that arrived at the detector within the same timing window may not come from the same positron-electron annihilation. This is called random coincidence. The rate of random coincidence along theLOR connecting detector i and j is mathematically modeled using the following equation:

$$R = 2\tau R_i R_j \tag{1-6}$$

Where $\boldsymbol{\tau}$ is the coincidence timing window, $\boldsymbol{R_i}$ and $\boldsymbol{R_j}$ are the rates of detecting single gamma photons at detector $\boldsymbol{i}$ and $\boldsymbol{j}$. This relation stands as long as the single rates are much larger than the coincidence rate, and small compared to the reciprocal of the timing window. Figure 1-6 demonstrates three types of coincidence.

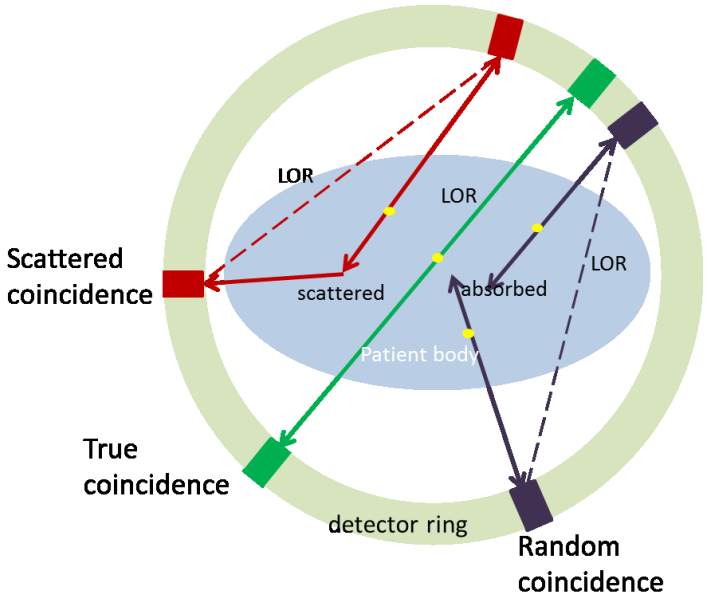

Figure 1-6 Three types of coincidence

Scattered coincidence and random coincidence degrades image quality by reducing image contrast and increase image noise. Theoretically, subtracting scattered and random coincidence from the total detected events should recover the count of true coincidence. However, the number of scattered coincidence and random coincidence is unknown. Methods have been developed to obtain accurate estimation of the two coincidence types from the PET data itself. 1-6 provides one method to approximately calculate the random coincidence rate for any two detector bins. Another method called the delayed coincidence channel method [10] uses the number of coincidences acquired with a delayed time window to approximate the number of random coincidences. The delayed coincidence channel collects gamma photon pairs detected by the scanner with one photon delayed by 3~5 times of the width of coincidence timing window, therefore contains no true coincidence.

Scatter correction for 3D PET is an active research topic. There are generally there groups of methods: The model-based approach, Monte-Carlo-based approach, and measurement-based approach. Proposed methods include but not limited to: model-based scatter correction algorithms [11], the "Gaussian fit" approach [12], convolution-subtraction method [13], Monte-Carlo modelling methods [14], multiple energy window method [15], and direct measurement method [16]. Based on the emission data, the attenuation map as well as model of the imaging system, the model-based approach uses the Klein-Nishina formula to calculate the scatter coincidence rate. One example is the single scatter simulation method [17] which calculates the counts of single scattered coincidences along each LOR based on the assumptions that only one of the two detected gamma photons is scattered once. The convolution of the single scatterd coincidence counts and proper kernel can be used to model multiple-scattered coincidence rates. Compared with model based methods, Monte-Carlo based methods are generally more accurate but at higher computationally cost.

DETECTOR RESPONSE AND DETECTOR NON-UNIFORMITY

The resolution of PET scanner is also limited by the interaction between the gamma photon and the detector as shown in Figure 1-7.

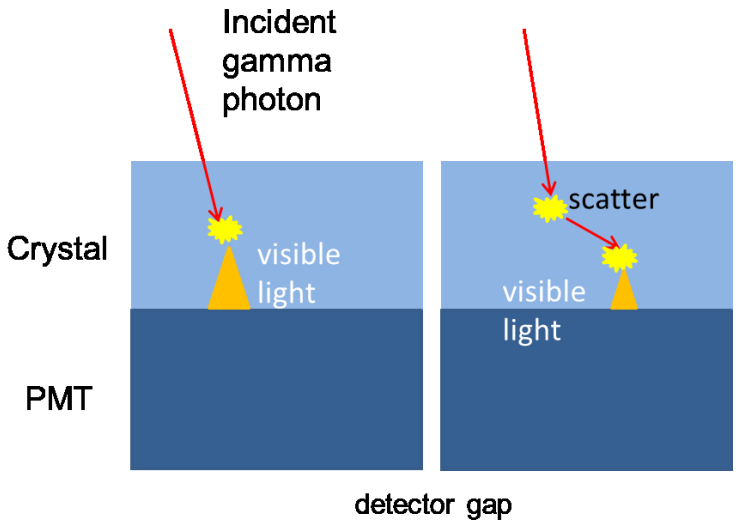

Figure 1-7 Gamma photon detection in the detector of PET scanner

PATIENT MOTION

There are two types of patient motion: the voluntary motion and involuntary motion. Voluntary motion is the motion initiated or can be easily controlled by the patient's brain. For example, the patient may cough or suddenly jerk during the scan. This kind of motion can be removed through patient training and simple motion correction to the data [18]. Involuntary motion means the natural biological motion of the patient's organ and body parts. Respiratory motion and cardiac motion are the two major types of involuntary motion. Since PET scan time is essentially longer than the period of both respiratory motion and cardiac motion, PET images are inevitably blurred by the two motion types. Specifically, the influence of respiratory and cardiac motion in cardiac PET, and methods to handle them is discussed later.

4. IMAGE RECONSTRUCTION

FILTERED BACK PROJECTION

Filtered back projection (FBP) is a well-established analytical imaging reconstruction method. It is based on the mathematical relationship between the activity distribution and the projection. The FBP algorithm will be demonstrated for the simplified 2D scenario shown in Figure 1-8. Accordingly, the projection data $p(s,\theta)$ is the integration of the radiotracer distribution $f(x,y)$ along the LOR:

$$p(s,\theta) = \iint_{R\times R} f(x,y)\delta(xcos\theta + ysin\theta - s)dxdy$$

1-7

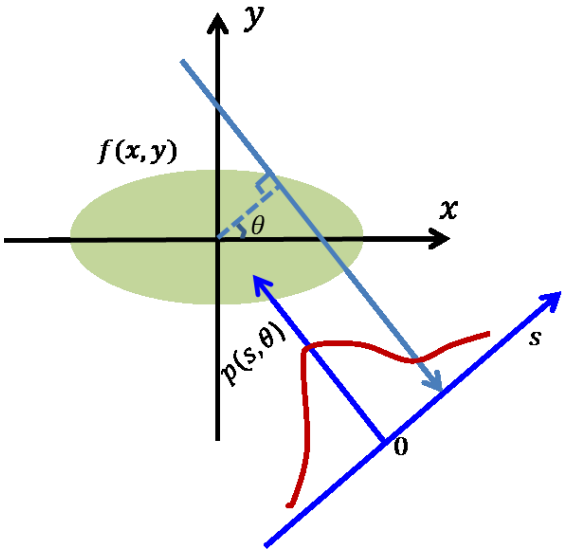

Figure 1-8 Relationship between activity distribution and projection

The transform from the activity map to the projection is called the Radon transform. It is easy to realize that the 1D Fourier of the projection is equivalent to the 2D Fourier transform of the intensity map along the projection direction, as demonstrated by Figure 1-9. This is called the central slice theorem. The following equation is its mathematical format.

$$P(w,\theta) = F(u,v)|_{u=wcos\theta, v=wsin\theta}$$

1-8

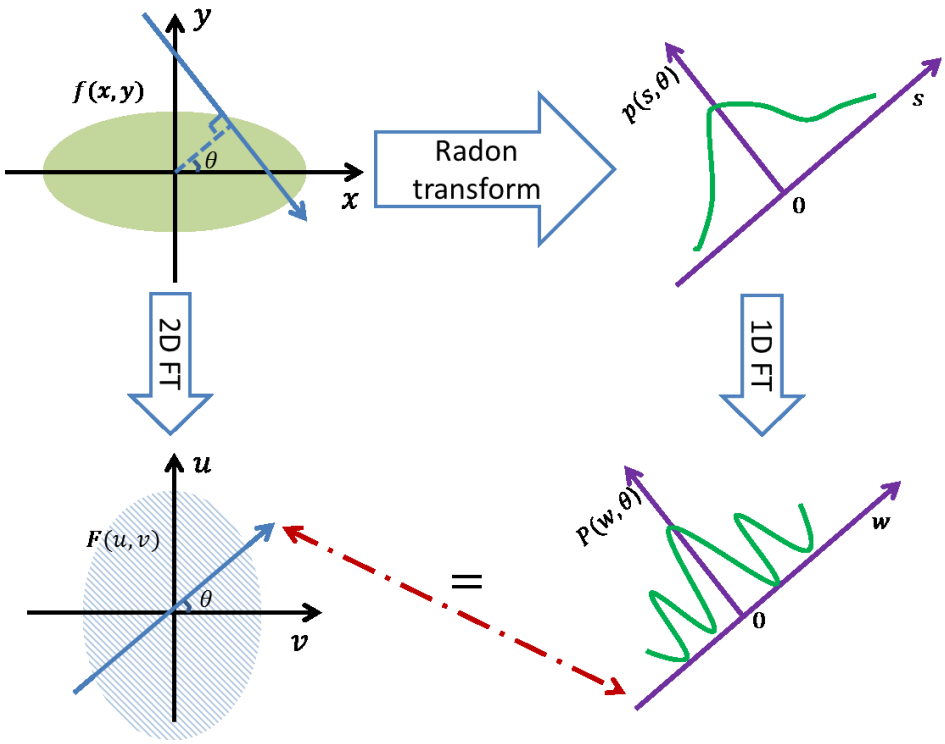

Figure 1-9 Demonstration of central slice theorem in 2D scenario

Activity distribution $f(x,y)$ is equal to the inverse 2D Fourier transform of $F(u,v)$. Using the central slice theorem, it is calculated by the following equation:

$$\int_0^{\pi}\int_{-\infty}^{\infty} P(S,\theta)e^{2\pi iSl}|S|dS|_{l=x\cos\theta+y\sin\theta}d\theta \quad (1\text{-}9)$$

Essentially, the solution is a back projection of the 1D Fourier transform of the projection data filtered by the ramp function $|S|$. To reduce noise and avoid aliasing problem, a low-pass window function is usually applied to the ramp filter.

The discrete form of the imaging process is given by:

$$\boldsymbol{g} = \boldsymbol{Hf} \quad (1\text{-}10)$$

Where g is the projection, f is a vector that represents the image space, and H is the system matrix. The filtered back projection method can be regarded as an inverse of the projection process. Considering noise in the projection data $\boldsymbol{g} = \boldsymbol{H}_{Radon}\boldsymbol{f}_{\boldsymbol{true}} + \boldsymbol{n}$, the solution by FBP method becomes:

$$\hat{\boldsymbol{f}} = \boldsymbol{B}_{FBP}\boldsymbol{g} = \boldsymbol{B}_{FBP}(\boldsymbol{H}_{Radon}\boldsymbol{f}_{\boldsymbol{true}} + \boldsymbol{n}) = \boldsymbol{f}_{\boldsymbol{true}} + \boldsymbol{B}_{\boldsymbol{FBP}}\boldsymbol{n}$$

1-11

The noise is amplified by the ramp filter in the $\boldsymbol{B}_{\boldsymbol{FBP}}$, resulting in bad image quality. Besides image noise, the FBP method does not allows for accurate correction of image degrading factors such as scatter. Therefore, it has limited use in clinical PET scan. Other analytical image reconstruction methods such as the iterative algebraic reconstruction techniques (ART) [19, 20] also suffer from the same problem as FBP and therefore not widely used.

STATISTICAL ITERATIVE METHODS

Unlike analytical reconstruction methods, statistical iterative algorithms incorporate modeling of the statistical distribution of photon counts and other factors possibly involved in the data acquisition into the reconstruction process. This allows better noise handling ability and more accurate modeling of system geometry and image degrading factors such as scatters. Comparing with analytical algorithms, statistical methods tend to achieve higher image quality in terms of noise level and resolution. Another advantage of statistical iterative method is that it can easily handle list-mode data without the need of conversion to sinogram. This not only avoids reducing resolution, but also allows for event-by-event motion compensation and full usage of time-of-flight information. The most widely used image reconstruction methods based on statistical model are the maximum likelihood expectation maximization (ML-EM) [21, 22], and its accelerated version the ordered subset expectation maximization (OS-ES) [23]. Both ML-EM and OS-EM have been adapted to list-mode data and have demonstrated improvement in image quality and reconstruction speed [24, 25].

Since radioactive decay is a Poisson process, the projection data can be modeled by a Poisson distribution with mean value determined by intensity distribution and system matrix. The probability of getting the projection data $\boldsymbol{p}$is described by the following equation, assuming no interference between any detector bins.

$$Prob[\boldsymbol{p}|\boldsymbol{x};\boldsymbol{K}] = \prod_i \left(\left(\sum_j K_{ij} x_j \right)^{p_i} (p_i!)^{-1} \exp\left(-\sum_j K_{ij} x_j \right) \right)$$

1-12

In the above equation, x_j is the activity intensity at pixel or voxel j, p_i is the photon counts at detector bin i, and K_{ij} is the system parameter that determines the contribution of voxel j to detector i, or in other words, the probability of photon originating from voxel j being detected by detector i. The activity distribution estimate $\boldsymbol{x}$ that maximizes the probability function or functions derived from it, is regarded as the solution of image reconstruction by all the algorithms built on this model.

ML-EM

This method seeks to find the activity distribution $\boldsymbol{x}$ by finding the estimate that maximizes the conditional expectation of the log of **Error! Reference source not found.** which is described by the following e quation. This is called expectation maximization (EM) algorithm.

$$E\{\log Prob[q|p,\hat{x};K\} = \sum_i \sum_j -K_{ij}\hat{x}_j + \frac{K_{ij}\hat{x}_j}{\sum_k K_{ik}\hat{x}_k} p_i \log\left(K_{ij}\hat{x}_j\right) + R$$

1-13

Hence the update formula for $(l+1)$th iteration is given by:

$$\hat{x}_j^{l+1} = \frac{\hat{x}_j^l}{\sum_i K_{ij}} \sum_i K_{ij} \frac{p_i}{\sum_{j'} K_{ij'}\hat{x}_{j'}^l}$$

1-14

This equation indicates the update consists of two steps. The projection step is represented by $\sum_{j'} K_{ij'}\hat{x}_{j'}^l$ which means the expectation of the projection based on the current estimate $\hat{\boldsymbol{x}}$. The back-projection step is realized by the $\sum_i K_{ij} \frac{p_i}{\sum_{j'} K_{ij'}\hat{x}_{j'}^l}$ term, which transforms the difference between expected projection $\sum_{j'} K_{ij'}\hat{x}_{j'}^l$ and the actual projection p_i to the image domain. The term $\sum_i K_{ij}$ is called sensitivity, as it represents the chance of a decay at voxel j is detected by any possible detector bins. Since the update is multiplicative, it is easy to impose non-negative constraint on the voxel intensities required by the PET imaging situation.

OS-EM

To reduce the computational cost of updating the intensity estimate of all the voxels using all the projection data during each iteration as experienced by the ML-EM algorithm, the OS-EM algorithm updates the image estimates using one subset of the projection data at a time. The projection bins are grouped into M ordered subsets S_m $(m = 0,1,\dots,M-1)$ to make sure only one subset contains each certain LOR. The update formula for iteration l is described as below:

For $m = 0,1,\dots,M-1$

$$\hat{x}_j^{lM+m+1} = \frac{\hat{x}_j^{lM+m}}{\sum_{i\in S_m} K_{ij}} \sum_{i\in S_m} K_{ij} \frac{p_i}{\sum_{j'} K_{ij'} \hat{x}_{j'}^{lM+m}}$$

End

1-15

For an OS-EM algorithm with iteration number n and subset number m, the image estimate is updated n*m times in total. The OS-EM algorithm using M subsets is generally M times faster than the ML-EM. Since only a subset of the projection data is used in each update, the number of subsets M needs to be chosen carefully to balance the efficiency and accuracy of the algorithm.

MLAA

Quantitative reconstruction of tracer distribution for PET imaging requires accurate attenuation correction. Attenuation map can be obtained from transmission data such as co-registered CT image or PET data acquired with external rotation sources, or MR images. However, such data may not be available or reliable. Great efforts have been made to estimate the attenuation coefficients from the emission data only. The challenge of attenuation estimation in PET is to solve the severe and persistent "cross-talk" between the estimated activity and attenuation distributions. J. Nuyts provided such an algorithm referred to as maximum-likelihood reconstruction of attenuation and activity (MLAA) [26]. The TOF-MLAA algorithm developed by ReZaei incorporates TOF information into the likelihood function [27]. However, even with TOF information, the activity map and attenuation sinogram can only be determined up to a constant [28]. Both algorithms update the activity and attenuation alternately; in other words, the activity is updated using

the attenuation coefficients updated from the last iteration as constant, and then vice versa. The update formula for activity $\boldsymbol{x}$ and attenuation $\boldsymbol{\mu}$ at $(h+1)$th iteration in TOF-MLAA are given below:

$$a_i^h = e^{-\sum_j l_{ij}\hat{\mu}_j^h}$$

1-16

$$\hat{x}_j^{h+1} = \frac{\hat{x}_j^h}{\sum_{it} a_i^h c_{ijt}} \sum_{it} a_i^h c_{ijt} \times \frac{p_{it}}{\sum_\xi a_i^h c_{ijt} \hat{x}_j^h + s_{it}}$$

1-17

$$\psi_i^h = a_i^h \sum_{jt} c_{ijt} \hat{x}_j^{h+1}$$

1-18

$$\hat{\mu}_j^{h+1} = \hat{\mu}_j^h + \frac{\sum_i l_{ij} \frac{\psi_i^h}{\psi_i^h + s_i} (\psi_i^h + s_i - p_i)}{\sum_i l_{ij} \frac{(\psi_i^h)^2}{\psi_i^h + s_i} \sum_\xi l_{i\xi}}$$

1-19

In which c_{ijt} is the sensitivity of the detector at (i,t) for activity in j ignoring attenuation, l_{ij} is the intersection length of LOR i with voxel j, and s_{it} is the expected contribution of scatter and/or randoms. c_{ij} and s_i are the summation of c_{ijt} and s_{it} over the TOF index t. a_i^h is the non-TOF sinogram based on current estimate of attenuation, while ψ_i^h is the non-TOF sinogram integrated with TOF count.

5. CARDIAC PET IMAGING

As one of the most important organ in human body, the condition of heart significantly influences the health and quality of life. Intensive medical research and clinical practice has been dedicated to the diagnosis and evaluation of cardiac diseases such as cardiovascular abnormalities and conditions that affect muscle, valves or rhythm of the heart. PET imaging techniques dedicated for this purpose provides crucial information necessary to discover and study functional abnormalities of the heart such as cardiac vascular diseases (CAD) [29]. For example, cardiac PET can provide information about perfusion defects [30], ejection fraction [31], plaque [32], and motion abnormalities [33], etc. Although photon emission computed tomography (SPECT) can also provide similar information of the heart at lower price, cardiac PET is more advantageous with higher image resolution and system sensitivity.

According to the biochemical property of the tracer, there are mainly two types of radioactive tracer used in cardiac PET imaging. One group is called perfusion agent, blood flow markers whose uptake in the myocardium directly indicates its blood supply. When a blood vessel of the heart is narrowed or blocked, the reduced blood flow leads to lack of perfusion in the region for which it supplies blood. This will be reflected by a "cold" region in the myocardium perfusion PET images. Commonly used perfusion agent includes Rubidium-82, Nitrogen-13 ammonia and Oxyggen-15 water [34]. Another type of tracer provides information about the metabolism or viability of the myocardium. Glucose participates in the metabolic process of the cells. Therefore, fluoro-2- deoxyglucose (F-18 FDG) can be used to diagnose diseases such as cardiac sarcoidosis [35]. Figure 1-10 shows the anatomy of the human heart and the corresponding cardiac PET image [36] with Nitrogen-13 ammonia in three axis, short axis (SA), vertical long axis (VLA), and horizontal long axis (HLA). A perfusion defect pointed by the arrow can be observed from the image.

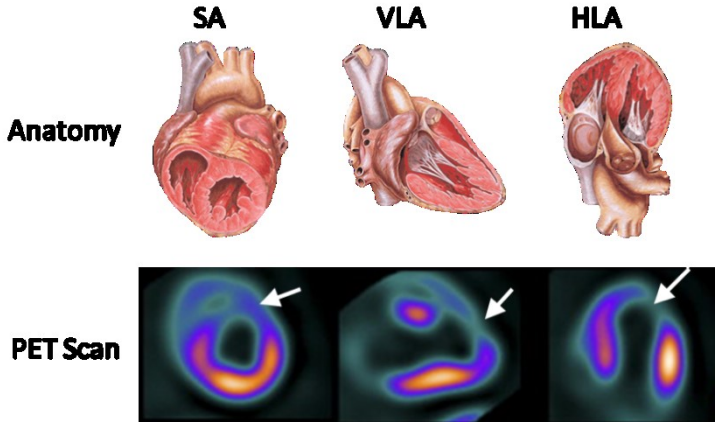

Figure 1-10 Heart Anatomy and Corresponding PET images

Not only the tracer intensity in the myocardium provides useful information, the change of the shape of myocardium revealed in cardiac PET images also helps detecting motion abnormalities. Cardiac-gated PET images capture the moving heart at several cardiac phases as shown in Figure 1-11. In cardiac PET imaging, the widely used number of gates is eight. Experienced physicians are able to spot regional or global motion defects by observing the beating heart in the cardiac gated images.

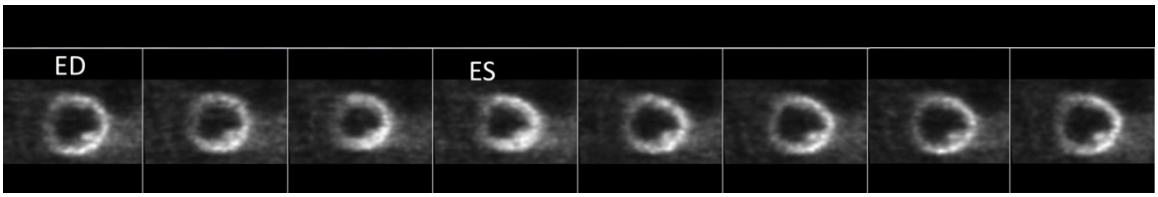

Figure 1-11 8-frame cardiac gated images of an ^{18}FDG study in short-axis view

6. RESPIRATORY MOTION IN CARDIAC PET

The resolution of currently available commercial PET systems has reached 4~5mm [37]. However, several factors during the PET scan significantly degrade the image quality and make it impossible to achieve this nominal spatial resolution. One of these factors is the respiratory motion, which has been reported [38] to be 10-20 mm in head-to-toe direction for heart. A routine PET scan in the clinics can last from 5 to 20 minutes. Although it is possible to reduce respiratory motion effects through approaches such as instructing the patient for shallow breathing, it is impossible to be eliminated [39]. The respiratory motion degrades image quality through two mechanisms. One is the blurring of the tissues and organs since the activity does not stay in the same location. As the heart moves up and down during the respiratory cycle, the image of the heart reconstructed from the acquired PET data is a blurred version of the true intensity map. The other issue is related to the integration of PET and CT in current multimodality imaging trend. The CT scanner provides anatomical information of the patient body, which helps improve spatial co-registration and diagnostic accuracy. Meanwhile, the fast and high-resolution CT scan can provide the attenuation map for use in the attenuation correction of the PET data. The CT scan is usually acquired within a few seconds during which breath holding is possible, while the PET scan can cover quite a few breathing cycles. As a result, the attenuation coefficient image from CT scan is unlikely to match the activity map in PET scan. The attenuation map mismatch can result in artifacts especially in the boundaries of organs such as lung and liver [40]. Both mechanisms can lead to inaccurate quantitation and diagnostic error of lesion localization [41].

RESPIRATORY GATING

RM leads to a reported range of 10-20 mm motion of the heart in the cranial-caudal direction [38], significantly degrading the image quality of cardiac PET data. Due to the relatively long duration of a PET scan which is on the order of 10 minutes compared to a typical RM cycle of about 5 second, it is difficult to

completely eliminate the effects of RM [39], which degrades PET image quality through two mechanisms. One is resolution loss due to motion blur. The other is generation of image artifacts by introducing mis-match of the activity distribution and attenuation map for attenuation correction (AC) especially when a "snap shot" CT scan is used in CT-based AC methods [42]. The image degrading effects lead to lower lesion detectability due to loss of image resolution and contrast, inaccurate quantitation, and image artifacts that affect clinical diagnosis [41].

To reduce the effects of RM in PET imaging, respiratory gating [43-45] and RM correction techniques [46, 47] have been developed and applied to patient studies. In respiratory gating, PET data are divided into different time frames or gates. Each respiratory gate (RG) covers a specific phase of the respiratory cycle with negligible RM. To reduce activity-attenuation mismatch and image artifact, the 'snap-shot' CT scan will need to be transformed and accurately registered [48] to the activity distribution at each RG for accurate attenuation correction.

The RM signals used for respiratory gating can be obtained through two groups of methods. The first group of methods employs external RM monitoring devices. An example is a respiratory bellows that straps around the patient's chest and detects the pressure on the bellows to track the RM [43, 49]. Another method is to use a video camera to measure the displacement of the patient's chest and convert the information to RM[44]. Other approaches include using a temperature sensor to measure changes of temperature in the air flow during breathing [50], piezoelectric crystals to sense pressure changes [51], or the MRI navigator techniques that track motion of the diaphragm [52]. All these methods rely on additional equipment to obtain a surrogate for respiratory motion, and require extra time and effort during setup and measurements. The accuracy and reliability of the measured signal depends on the monitoring equipment and users' experience and skills. In addition, a disadvantage of these methods is that the measured signal is often not directly related to the affected organ of interest, e.g., the heart. For example, poor correlation has been observed between measurements of the external RM devices and the motion of the heart due to hysteretic behavior between inspiration and expiration [53].

The second group of methods overcomes the above disadvantages of the first group. Known as data-driven RM signal extraction methods, they extract the RM signal directly from the acquired PET data. A respiratory motion signal can be obtained by processing the count variations from the manually chosen

regions of interest (ROIs) covering moving organ boundaries on reconstructed dynamic frames[54], or from regions subject to RM identified by Fourier analysis of a cine PET sinogram[55]. Another approach relies on frequency analysis of the center-of-mass (COM) movement of a ROI containing the moving organ which can be the lung tumor in oncologic PET images[56], or the heart in cardiac PET images[45]. The advantages of the data-driven methods are that the extracted RM signal is a direct indication of the motion of the target organ, and the RM signal is obtained with no extra cost, time or effort. However, the effectiveness and accuracy of the data-driven methods rely on the quality of the acquired data, and appropriate data and image processing techniques, and the RM signal extraction method used. Moreover, some of these approaches require sinogram rebinning or image reconstruction for consecutive time intervals each at 100~500ms, which is very time-consuming and computationally expensive.

RESPIRATORY MOTION COMPENSATION

Respiratory motion is relatively homogeneous for the heart region and therefore easy to correct. There have been lots of studies on respiratory motion correction to the PET data. One of the methods is MR-based respiratory motion correction. With hybrid PET/MR scanners available, respiratory motion can be obtained from MR signals and applied to respiratory gated PET data for improved image quality [57]. Respiratory motion can also be obtained from gated PET images. Rigid and non-rigid motion models have been proposed to describe respiratory motion and correct respiratory-gated data [58] through image registration. Besides motion correction on reconstructed images, the respiratory motion derived from MR or PET images can also be incorporated into image reconstruction process for motion compensation [59, 60].

7. CARDIAC MOTION IN CARDIAC PET

CARDIAC GATING

For the purpose of reducing motion blurring and visualizing the cardiac motion, cardiac gating divides PET data into several (typically 8) time frames based on information of the cardiac motion during the scan. The widely used electrocardiogram (ECG or EKG) signal provides temporal information of each cardiac beat of the patient vie recording the electrical impulses generated by the polarization and depolarization of cardiac tissue. Currently most list-mode PET scanners incorporate ECG monitors, and the ECG trigger is recorded

within the list-mode data. Data-driven cardiac gating that relies on cardiac signal derived from the data is also proposed but with much fewer application due to low success rate [45].

CARDIAC MOTION ESTIMATION

Cardiac motion estimation for PET images is essentially an image registration task, which seeks to establish spatial correspondence between two or more images. The registration transformation $\boldsymbol{T}$ that maps a position $\boldsymbol{x}$ in image A to a point $\boldsymbol{x'}$ in image B, i.e.,

$$\boldsymbol{T}: \boldsymbol{x} \mapsto \boldsymbol{x'} .$$

1-20

The cardiac motion vector field (MVF) $\boldsymbol{M}$ is an alternative representation of this transformation:

$$\boldsymbol{M}(\boldsymbol{x}) = \boldsymbol{x'} - \boldsymbol{x} ,$$

1-21

where $\boldsymbol{x}$ and $\boldsymbol{x'}$ are usually the 3D coordinates of each voxel.

Although many methods have been developed for image registration purpose, no all of them are applicable in cardiac motion estimation scenario. There are mainly two groups of image registration methods. The first group uses corresponding point/line/surface landmarks to find transformation between images. This group of method is not very suitable for cardiac motion estimation purpose. Some use markers attached to the skin[61] or teeth[62], or inserted into the bone[63] that are visible under corresponding imaging modalities, and then use point-based registration to find transformation map. These methods provide straightforward solution for rigid transformation, and can also be used to define simple non-rigid transformation[64]. However, they are not practical in cardiac motion estimation. On one hand, it is incapable of capturing the complex 3D motion of the heart with limited numbers of markers; on the other hand, the invasive planting of the seeds into the human heart is very likely to cause damage to the cardiac function and disturb cardiac motion. Some rely on automatic or interactive image segmentation to extract features such as boundaries or surfaces of organs and then find the transformation that matches the features. One example is the head-and-hat algorithm which was originally used to align images of the head between different modalities of different resolutions[65]. Another example is the Iterative Closet Point (ICP) algorithm[66] that iteratively identifies the closest point in the target image surface for the points in source image surface. Local

geometry such as crest lines can also be used as feature alternative to pre-segmented surfaces[67], but require high-resolution images and are sensitive to noise. These methods are applicable to cardiac motion estimation specifically, but given the low-resolution and noisy cardiac PET images, their application is limited.

The second group computes image transformation directly from the voxel intensities and is shown to outperform feature-based methods [63]. For intra-modality image registration, the solution is the image transformation that minimize the mean sum of squares of difference (SSD) [68], or the correlation coefficient(CC) between the image intensities [69]:

$$SSD = \frac{1}{N}\sum|(A(\boldsymbol{x}) - \boldsymbol{T}(B(\boldsymbol{x}))|^2,$$

1-22

$$CC = \frac{\sum(A(x)-\bar{A})(T(B(x))-\bar{B})}{\{\sum(A(x)-\bar{A})^2 \sum(T(B(x))-\bar{B})^2\}^{1/2}}.$$

1-23

For multi-modality registration purpose, mutual information in ()can be used as the registration metric[70], which may also be applicable to intra-modality scenario[71].

$$I(A,B) = H(A) + H(B) - H(A,B).$$

1-24

$H(A)$is the Shannon-Weiner entropy of image A, and $H(A,B)$ is the joint entropy of image A and B.

Besides the metric of image similarity, most of the algorithms enforce smoothness of the resulting transformation map by adding a penalty term calculated based on spatial differentiation of the transformation field, or by using B-spline function to represent the transformation function[68, 71-73]. Methods with B-spline modeling of transformation function are referred to as B-spline registration.

All registration algorithms in this group rely on a process of optimization to compute the transformation that aligns the two images in the best way evaluated by certain metric. A major limitation of these methods is that the optimization process is likely to arrive at local optimizer instead of global optimizer. Multi-resolution methods are often used[74] to address this problem, but cannot solve it completely.

In medical imaging field, most of the methods mentioned about are mainly used to align images of organs or body regions that do not move as periodically and intensively as heart. In those cases, B-spline is sufficient to model the non-rigid displacement between two images. None of the methods is dedicated to cardiac motion estimation in PET imaging, and does not take the complexity of the cardiac motion into consideration. They are purely image-based methods.

The optical-flow approach belongs to the second group of methods, and our method is developed based on this approach.

CURRENT OPTICAL-FLOW BASED MOTION ESTIMATION METHOD

First proposed by Horn and Schunck [75], the optical flow determination method lays the foundation for many cardiac motion estimation methods designed for CT and ECT images. Optical flow, defined in Horn and Schunck's paper as "the distribution of apparent velocities of movement of brightness patterns in an image", is an approximation to the real image motion. MVF calculated using the optical-flow based approach does not contain motion parallel to edges of intensity patterns, that is, movement in the direction of the iso-brightness contours. The MVF is calculated from 2D images by iteratively optimizing brightness constraint and smoothness constraint. Song and Leahy [76] introduced the incompressibility constraint and divergence-free constraint into the cost function for 3D implementation of the optical flow method. Pointing out that it is difficult to find proper weight of the two constraints in Song and Leahy's method, Klein and Huesman [77] proposed to estimate the MVF by minimizing the intensity mismatching error between deformed volume and the reference volume, and the strain energy of the cardiac muscle as a linearly elastic uniform isotropic material. They later extended this method into 4D by adding a new term to the cost function to guarantee the consistence of the motion during the cardiac cycle [78]. Applying the proposed 4D cardiac motion estimation method in paired gated PET/ MRI image datasets from normal human subjects, Klein [79] found it difficult to extract motion tangential to the myocardial boundaries in the PET images and even in high-resolution cine MR datasets, especially for homogeneous mid-wall sections; while in tagged MR images, the detection of cardiac twist is much more successful because of the useful image features contained. The study suggests the possibility of extracting accurate cardiac MVF in images of rich features. These features could be unique anatomical structures like the papillary muscles,

and the RV insertion point that has been used to track cardiac torsion [80, 81]; it could also be uptake non-uniformities such as perfusion defects in gated cardiac PET images. Besides developments of algorithms for motion estimation only, there are also researches seeking simultaneous image reconstruction and motion estimation. A penalty function containing the log likelihood of projection data, intensity mismatch and strain energy, can be iteratively minimized to generate estimation of the image and the MVF [82-84].

LIMITATIONS OF THE CONVENTIONAL METHOD

The first limitation of optical-flow based cardiac motion estimation is that the optimization of the cost function requires an initial estimate of cardiac MVF, and the result is highly dependent on the initial. The zero-valued MVF is usually used as the initial, which is likely to lead the optimization to a local minimum.

Moreover, the aperture problem is intrinsic to the optical flow algorithm. Only motion that is perpendicular to the edges can be detected, and motion parallel to the edges is not detectable since it does not cause change in intensity yet increases strain energy. Unfortunately, cardiac motion contains important components that are parallel to the edge of the myocardium --- the heart twists during the cardiac cycle to squeeze blood out of the ventricles.

Although many researches that apply optical flow based motion estimation algorithms in cardiac images of various imaging modalities have been carried out previously, most of them only provide qualitative evaluation of the motion estimation results based on visual observation, since ground truth is not available for clinical cardiac datasets. In addition, analysis of the estimated cardiac MVF in previous studies rarely take the complexity of cardiac motion into consideration. The anatomy of the heart, characteristics of cardiac motion, and mechanics of cardiac muscle fibers are rarely taken into consideration. Cardiac motion consists of three components: the radial motion, the circumferential motion, and the longitudinal motion. The performance of the motion estimation approach is rarely systematically analyzed in terms of all three cardiac motion components.

8. AIM AND SIGNIFICANCE OF THIS THESIS

This thesis will cover two research topics: data-driven respiratory gating for list-mode cardiac PET data, and feature-based cardiac motion estimation for gated-cardiac PET images. Study on the first topic employs

clinical patient data, and will be presented in Chapter 2. The second topic will be studied mainly with simulation data, and the results will be shown in Chapter 3. Both topics are significant for cardiac PET imaging in both research and clinical area.

The goal of the first study is to improve the performance and robustness of data-driven RM extraction, estimation and gating techniques. The traditional COM based data-driven respiratory gating techniques are not sufficiently robust to handle patient data with high noise level and low target organ-to-background uptake ratio. From the projection data, they often take the counts within the entire field of view without discriminating between the stationary and the moving target organ. As a result, the RM signal derived from the COM of the moving target organ is affected by counts from the stationary region, which leads to reduced accuracy. The data-driven techniques will simplify the RM gating process for use in routine clinical cardiac PET studies without the extract cost, time and effort involve in using an external RM monitoring device. We proposed three approaches including heart-dedicated volume-of-interest (VOI) selection, the use of time-of-flight information[85], and background correction. Six data-driven methods for list-mode cardiac PET data that mix-match the three approaches are developed. Finally, we evaluated the effectiveness and robustness of six approaches using clinical cardiac PET data.

Data-driven respiratory gating has become an active research topic driven by the high requirement of cardiac image quality as well as by the improvement in cardiac PET imaging techniques such as the introduction of TOF and the increase of system resolution. Its application is not limited to cardiac PET imaging. Respiratory motion leads to image blurring, motion artifacts, and activity-attenuation mismatch, all of which degrades the image quality for the whole thorax region. Lung nodules and lesions in the liver can be easily missed or misplaced in ungated images. External devices are not always available for clinical use. Even when they are available, it takes proper training and experience for technicians to master the skills to use them correctly. The inconvenience, extra cost in money and human labor, as well as limited availability of external devices makes data-driven methods more appealing in practical use.

The proposed data-driven respiratory gating method extracts respiratory motion signal directly from the list-mode data without the need of sinogram re-binning. It can be used as a prototype and incorporated into the software of clinical PET scanner for convenient data processing right after acquisition.

The second study is the major part of this thesis. Cardiac PET imaging is currently not the go-to imaging method due to its relatively low system resolution and long acquisition time. However, it is an important imaging technique for collecting cardiac functional information and has extensive application in myocardium viability studies. Although cardiac-gated CT and tagged MR can provide images of higher resolution and track cardiac motion, they either imposes extra radiation dose to the patient, or requires sophisticated pulse-sequence designing and has limited availability in clinical application. The problem we are trying to solve is to extract cardiac motion information directly from gated cardiac PET images. With this technique, we will be able to obtain not only functional information such as perfusion and viability, but also evaluation of cardiac motion condition within a cardiac PET scan.

The goal of our study on cardiac motion estimation is to overcome or reduce the limitations of optical-flow based motion estimation method– the initial dependency and the aperture problem. Many studies have been carried out on cardiac motion estimation but none of them has systematically analyzed cardiac motion components or quantitative evaluated the motion estimation results. With simulated cardiac PET data using realistic digital phantom and advanced analytical as well as statistical simulation tools, we will evaluate the cardiac motion estimation results both quantitatively and qualitatively. The improvement in cardiac PET imaging technique has been providing images of higher and higher quality in terms of resolution. Although the simulation data is still not available in clinical use, we are confident that the resolution of the next-generation PET scanner will keep improving. This in time will make our method more practical in clinical use.

The MVF estimated using the cardiac motion estimation algorithm provides important information for diagnosis of global and regional cardiac motion abnormalities. Especially, with cardiac motion component analysis of the MVF, we will be able to tell which component is not functioning well. Moreover, the MVF can be used for motion compensation of cardiac gated images to improve image quality and reduce motion artifacts. Small regional perfusion defects or viability lesions that may be blurred out by cardiac motion can be recovered with accurate cardiac motion compensation. The motion components parallel to edges are difficult to estimate with conventional methods. The method proposed in this study will try to recover these components. As a result, cardiac motion compensation will be able to reveal small defects that are difficult to identify using MVF estimated by conventional methods.

CHAPTER 2. ADVANCED DATA-DRIVEN RESPIRATORY GATING FOR LIST-MODE CARDIAC PET DATA

Accurate respiratory gating is a prerequisite of generating cardiac PET images of improved image quality by dual respiratory and cardiac motion compensation. The goal of this study is to improve the performance and robustness of data-driven RM signal extraction, estimation and gating techniques. The traditional COM based data-driven respiratory gating techniques are not sufficiently robust to handle patient data with high noise level and low target organ-to-background uptake ratio. Moreover, not all counts within the field of view come from the moving target organ. By identifying separate background and target regions, the RM signal derived from the COM of the moving target organ is less affected by the stationary background, which can lead to improved accuracy.

We propose three approaches including heart-specific volume-of-interest (VOI) selection, the use of time-of-flight information[85], and background correction. The performance and robustness of six data-driven methods that mix-match these three approaches are evaluated using clinical cardiac PET data.

METHODS AND MATERIALS

DATA-DRIVEN RESPIRATORY MOTION SIGNAL EXTRACTION METHODS

SYSTEM GEOMETRY AND NOTATIONS

A schematic diagram of the data acquisition configuration of a typical time-of-flight (TOF) PET scanner is shown in **Error! Reference source not found.**. The coordinates of the object space is r epresented by the *x*-, *y*-, and *z*-axes, where the *z*-axis lies along the axial direction of the PET scanner. The inner radius of the detector ring of the PET scanner is given by R. A pair of two 511 keV annihilation photons detected within a coincidence timing window and an energy window by the detector bins b_1 and b_2 at the detector ring numbers z_1 and z_2, respectively, is registered as a coincidence event. The line connecting b_1 and b_2 is defined as a line-of-response (LOR). The information about the recorded coincidence event, including the detector bins, detector ring numbers, energy of the detected photons, and the TOF bin t are recorded in the list-mode format. The azimuth and polar angles, θ and ϕ, are the angles between the LOR and the transaxial plane, and between the line perpendicular to the projection of LOR on

the transaxial plane and the $\boldsymbol{x}$-axis, respectively. A new coordinate system based on each coincident event is defined by three unit basis vectors $\boldsymbol{u}$, $\boldsymbol{v}$, and $\boldsymbol{w}$, where $\boldsymbol{v}$ is oriented along the direction of the LOR, $\boldsymbol{u}$ is the vector orthogonal to the LOR and lies on the transaxial plane, and $\boldsymbol{w}$ is orthogonal to both $\boldsymbol{u}$ and $\boldsymbol{v}$. In the object space coordinates, these three unit basis vectors are given by

$$\begin{cases} \boldsymbol{u} = (\boldsymbol{cos\phi}, \boldsymbol{sin\phi}, \boldsymbol{0}) \\ \boldsymbol{v} = (\boldsymbol{-sin\phi cos\theta}, \boldsymbol{cos\phi cos\theta}, \boldsymbol{sin\theta}). \\ \boldsymbol{w} = (\boldsymbol{sin\phi sin\theta}, \boldsymbol{-cos\phi sin\theta}, \boldsymbol{cos\theta}) \end{cases}$$

2-1

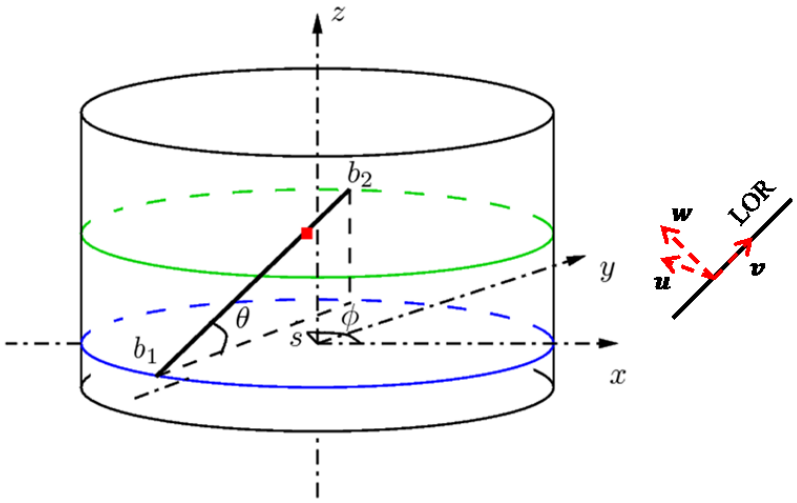

Figure 2-1 Schematic diagram of the data acquisition configuration of a typical PET scanner. The annihilation location is indicated by the red dot.

VOLUME-OF-INTEREST (VOI) SELECTION

Respiratory motion (RM) causes movement of the heart resulting in blurring in the heart in the cardiac PET images. Tracking the movement of the heart in 4D cardiac PET images allows estimation of RM at the location of the heart and can be used in RM compensation for improved image quality of cardiac PET images. In this work, the heart was identified from a preliminary image reconstruction using the ungated list-mode data and its center was determined to be at (c_x, c_y, c_z) in the object space of the summed 3D static image. The width of the heart in the transaxial plane and its length in the axial direction was determined as r_t and r_z, respectively. Radii that are slightly larger than r_t and r_z were chosen to be the radii of the 3D volume-of-interest (VOI) that encompasses the entire heart. The extracted VOI and its

projections was used to determine the 2D region-of-interest (ROI) containing the heart, or C-ROI, and a background ROI, or B-ROI, in a uniform background region next to the C-ROI. The location of the center of the heart in the $(\boldsymbol{u}, \boldsymbol{v}, \boldsymbol{w})$ coordinates is given by

$$\begin{cases} c_u = c_x cos\phi + c_y sin\phi \\ c_v = -sin\phi cos\theta c_x + cos\phi cos\theta c_y + sin\theta c_z \\ c_w = sin\phi sin\theta c_x - cos\phi sin\theta c_y + cos\theta c_z \end{cases}. \quad \text{2-2}$$

A transaxial or cross-section cut (x, y) plane of the 3D C-VOI in the object space is shown in **Error! Reference source not found.**. It is represented by the blue circle centered at (c_x, c_y) with radius r_t. In the image analysis, the circular shape was approximated by a square with a side length of $2r_t$. Two B-ROIs were chosen adjacent to the square C-ROI along the LOR projection. The areas of the cardiac ROI and background ROI are the same.

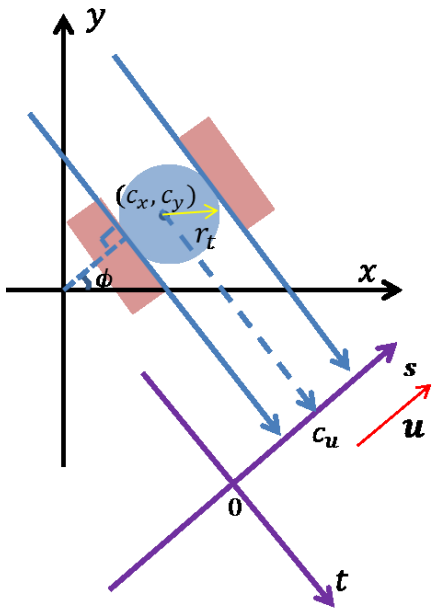

Figure 2-2 The definition of cardiac ROI, C-ROI, and background ROI, B-ROI, in a transaxial plane. The blue region represents the C-ROI and the red region the B-ROI.

In the coronal, sagittal or cross-sectional cut planes (x, z) or (y, z) that is parallel to the z-axis, the selection of C-ROI and B-ROI has to take tilted events into consideration. The shapes of the sectional cut through C-VOI and B-VOI are shown in Fig. 3.For coincidence events where the two annihilation photons

are detected by the same detector ring as shown in Fig. 3 (a), the projection of C-VOI and B-VOI satisfies$|z - c_z| < r_z$, in which z is the detector ring number. For events where the photons are detected by different detector rings, the projections of the C-VOI and B-VOI depend on the tilted angle θ. Hence the range of the detector ring number of one photon z_1 becomes

$$|z_1 - c_z'| < \frac{r_z}{cos\theta},$$

2-3

where

$$c_z' = c_z + \left(R - \left(-c_x\, sin\phi + c_y\, cos\phi\right)\right) tan\theta.$$

2-4

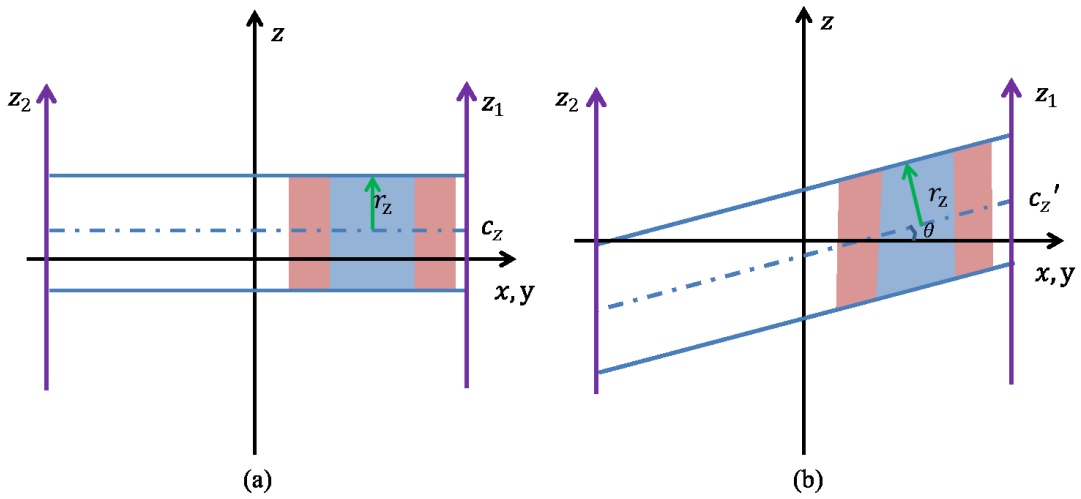

Figure 2-3. The projections of the C-VOI and B-VOI on the coronal or sagittal plane with the pair of annihilation photons detected by detector bins of the (a) same detector ring, and (b) different detector rings. The blue and red area represents the projection of the C-VOI and B-VOI on the plane defined by z axis and any straight line on x-y plane respectively.

CENTROID LOCATION CALCULATION WITHOUT AND WITH TOF

Without TOF information, the 3D C-VOI and B-VOI containing the heart and background regions in image and data analyses are referred to by the C-ROI and B-ROI defined in the projections. Photons detected by detector bin s that satisfies $|s - s_{00}| < r_t$ are not guaranteed to come from the C-VOI in**Error! Reference source not found.**. Therefore, the estimated C-VOI used in calculating the centroid l

ocation of the heart without TOF information as show in Figure 2-4 is larger than those shown in **Error! Reference source not found.**.

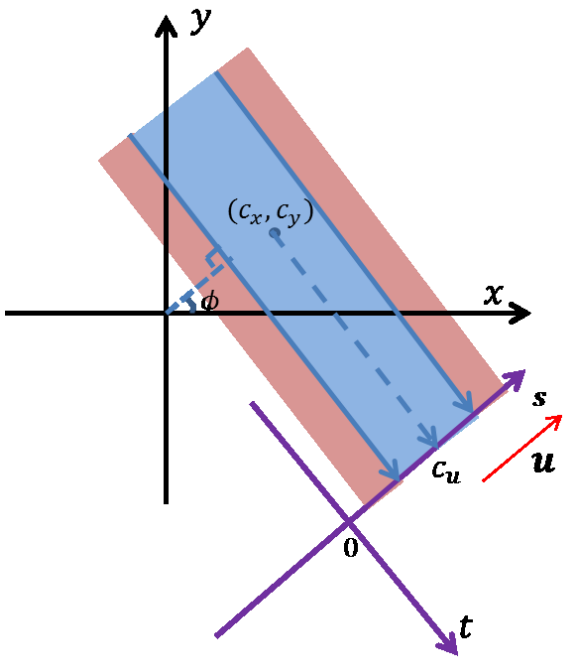

Figure 2-4. The estimated C-VOI and B-VOI used in the centroid of the heart calculation without TOF. The blue region represents the C-VOI while the red region represents the B-VOI.

Hence without TOF information, the location of the centroid of the heart is calculated from

$$z_{centroid} = \frac{\sum_{i \in ROI} z_i \cdot c_i}{\sum_{i \in ROI} c_i},$$

2-5

where $z_i = \frac{z_1 + z_2}{2}$ and c_i is the count of voxel i in the VOI. With TOF, the annihilation location can be identified more accurately to exclude photons that do not come from the heart VOI. The most likely annihilation (MLA) point of a detected coincidence event, *(x*, y*, z*)*, is defined at the maximum of the TOF profile along the LOR [86]. The coordinate of the MLA point is given by [86]

$$\begin{cases} x^* = s\cos\phi - \frac{l\sin\phi}{\sqrt{1+\delta^2}} \\ y^* = s\sin\phi + \frac{l\cos\phi}{\sqrt{1+\delta^2}} \\ z^* = z + \frac{l\,\delta}{\sqrt{1+\delta^2}} \end{cases},$$

2-6

where

$$\begin{cases} \boldsymbol{\delta = tan\theta} \\ \boldsymbol{z = \frac{z_1+z_2}{2}} \end{cases}.$$

2-7

In (6), s is the projection of the LOR on $\boldsymbol{u}$ axis; l is the TOF parameter that corresponds to the TOF profile $h(l-r)$ centered at position $r = l$ along the LOR direction. In other words, l is the difference between the arrival times of the two annihilation photons, $\Delta\tau$, at the corresponding detectors and is given by $l = c\Delta\tau/2$, where c is the speed of light. Its projection on the $\boldsymbol{v}$-axis is given by

$$\boldsymbol{t = z\,sin\theta - l}.$$

2-8

The uncertainty of the MLA is taken into consideration by assigning location of each annihilation event a weight calculated based on the TOF profile. The weight is calculated by

$$\boldsymbol{w = f(t - l_{00}) = m(l) \otimes h(l)}.$$

2-9

where $\otimes$ is the convolution operation and the mask, $m(l)$, and the TOF profile, $h(l)$, are given by

$$\begin{cases} m(l) = \begin{cases} 1, & for\ |l| \le r_t \\ 0, & otherwise \end{cases} \\ h(l) = \frac{1}{\sqrt{2\pi}\sigma} e^{-\frac{l^2}{2\sigma^2}} \end{cases},$$

2-10

where $\sigma = 7.5\ cm$ is determined by the temporal TOF resolution of the PET scanner and is a fixed parameter. The TOF profile $h(l)$ represents the uncertainty of the annihilation location along the LOR.

Thus, the centroid location on the axial direction is calculated using

$$\boldsymbol{z_{centroid-tof} = \frac{\sum_{i \in VOI} z_i \cdot w_i}{\sum_{i \in VOI} c_i \cdot w_i}},$$

2-11

where w_i is the weight used in the MLA calculation, z_i is the z coordinate of the MLA point for each of the TOF coincidence event *i* originated in the C-VOI.

RANDOM CORRECTION AND SENSITIVITY NORMALIZATION

The random coincidence was corrected using the standard subtraction of delayed coincidences method[87] by subtracting the events in a delayed time window from the prompt event as shown by the following equation.

$$z_{centroid-tof} = \frac{\sum_{i\in VOI,prompt} z_i \cdot c_i \cdot w_i - \sum_{i\in VOI,delay} z_i \cdot c_i \cdot w_i}{\sum_{i\in VOI,prompt} c_i \cdot w_i - \sum_{i\in VOI,delay} c_i \cdot w_i}. \quad \text{2-12}$$

In addition, since different detector bins have different sensitivity, the non-uniformity of the PET detectors was corrected by multiplying the acquired data with uniformity correction map that consists of correction factors, s_i, for each detector bin *i*. With the additional non-uniformity correction Eq. (12) becomes

$$z_{centroid-tof} = \frac{\sum_{i\in VOI,prompt} z_i \cdot c_i \cdot w_i \cdot s_i - \sum_{i\in VOI,delay} z_i \cdot c_i \cdot w_i \cdot s_i}{\sum_{i\in VOI,prompt} c_i \cdot w_i \cdot s_i - \sum_{i\in VOI,delay} c_i \cdot w_i \cdot s_i}. \quad \text{2-13}$$

BACKGROUND CORRECTION

NECESSITY OF BACKGROUND CORRECTION

The 2D C-ROI selected from the sinogram in section 2 contains not only the myocardium, but also some background region such as the blood pool, and portions of the lung and liver. Assuming the background is stationary, the estimated motion magnitude of the heart due to RM based on the centroid location, by summing all the detected counts that are included in C-ROI, is an underestimation of the true motion magnitude.

Figure 2-5 provides a schematic demonstration of centroid location calculation, in which the region inside the red square represents the C-ROI of heart used in centroid location calculation in the RM estimation. The two circles with their centroid locations c_1 and c_2 represent the locations of the heart at two respiratory phases, and the rest of the C-ROI region within the red square is the stationary background. Let

the detected counts that originate from the heart and are detected in the heart region be a and in the background region be b, and the centroid location of the background be c_b. Then, the estimated centroid locations of the entire C-ROI at the two respiratory phases are $\frac{ac_1+bc_b}{a+b}$ and $\frac{ac_2+bc_b}{a+b}$, and the respiratory motion amplitude will be

$$\boldsymbol{l = \frac{ac_1+bc_b}{a+b} - \frac{ac_2+bc_b}{a+b} = \frac{a}{a+b}(c_1 - c_2)},$$

2-14

which indicates that the estimated RM amplitude l is smaller than the true RM amplitude($c_1 - c_2$).

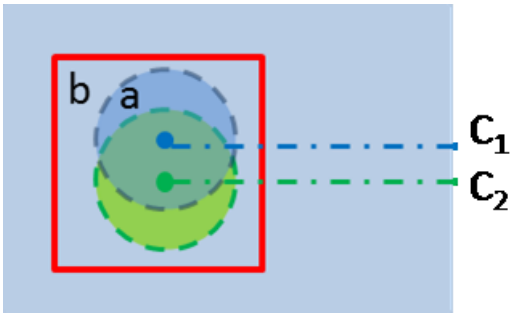

Figure 2-5. Schematic diagram of the RM motion estimation based on calculations of centroid locations of the C-ROI. "a" and "b" represents counts from the myocardium and from the background.

To correct this underestimation, we proposed a background subtraction approach. The basic idea is to identify the contribution from the background counts and subtract it from the centroid calculation equation. Since it is impossible to distinguish between the contributions of detected counts from the background and from the heart in the C-ROI, we can only seek an estimated background counts that is closest to the truth. The detected counts in B-ROI are used as an estimation of the true background counts. With background correction, the estimated centroid locations of the heart at the two respiratory phases become $\frac{ac_1+bc_b-b'c'_b}{a+b-b'}$ and $\frac{ac_2+bc_b-b'c'_b}{a+b-b'}$, where b' and c'_b are the estimated background counts and the centroid location of the background region, respectively. The closer the background estimation $b'c'_b$ is to the true background contribution bc_b, the closer the estimated RM amplitude, l, will be to the true RM amplitude, $(c_1 - c_2)$.

DIRECT AND SMOOTHED BACKGROUND CORRECTION

We proposed and evaluated a direct and a smoothed background correction method for more accurate estimation of the RM magnitude from the C-ROI data. In the direct background correction method, the detected counts from the B-ROI were subtracted from the counts in the C-ROI as shown by the following equation.

$$z_{centroid} = \frac{\sum_{i \in ROI} z_i c_i - \sum_{j \in Background} z_j c_j}{\sum_{i \in ROI} c_i - \sum_{j \in Background} c_j}. \quad \text{2-15}$$

After background subtraction, the centroid location sequence after subtracting the background become noisier. In the smoothed background correction method, the counts from B-ROI were smoothed with a low-pass filter before subtraction from the C-ROI to reduce the noise. The estimated centroid location of the C-ROI become

$$z_{centroid} = \frac{\sum_{i \in ROI} z_i c_i - F(\sum_{j \in Background} z_j c_j)}{\sum_{i \in ROI} c_i - F(\sum_{j \in Background} c_j)}, \quad \text{2-16}$$

where $F()$represents the smoothing function of the low-pass filter.

By combining TOF and background corrections, we have a total of six RM motion estimation methods to track the centroid locations of the C-ROI during the scan. Table I shows the six methods with different combination of TOF and background correction methods.

Table 2-1 Six RM motion estimation methods based on different combination of TOF and background correction approaches

	without TOF	**with TOF**
no background correction (N-BC)	Method 1	Method 4
direct background correction (D-BC)	Method 2	Method 5
smoothed background correction (S-BC)	Method 3	Method 6

With each method, the motion of the heart along the z-axis was tracked by estimating the C-ROI centroid location from the list-mode data at every 200ms of the list-mode data. The 200ms sampling rate was chosen

to provide sufficiently high Nyquist frequency to show the respiratory frequency of human, which ranges from 2 to 6 second, in the respiratory signal extraction and estimation described below.

POST-PROCESSING OF CENTROID MOTION SIGNAL

An example of the estimated C-ROI centroid location sequence from a sample list-mode data obtained from the previous section was shown in Figure 2-6 (a). Its Fourier Transform is shown in Figure 2-6 (b) which reveals a strong peak corresponding to a RM cycle of 4.15 sec. A smooth version of the RM curve shown in Figure 2-6 (c) was obtained by extracting the RM motion peak within the two red vertical bars in Figure 2-6 (b), thereby removing the low frequency variation and high frequency noise in C-ROI centroid location sequence shown in Figure 2-6 (a). Finally, an inverse Fourier transform was applied to the extracted frequency spectrum to obtained a smoothed RM signal shown in Figure 2-6 (c).

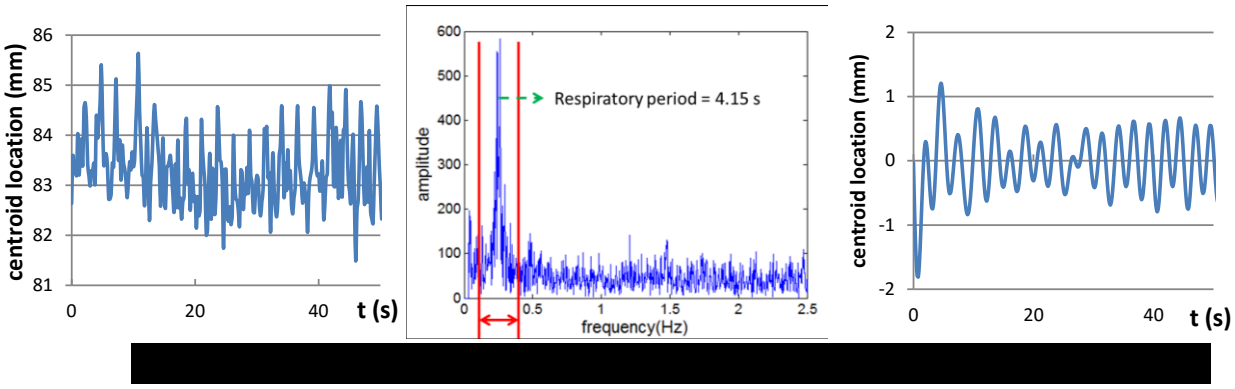

Figure 2-6. RM signal extraction and processing. (a) An example of estimated C-ROI centroid location sequence from the list-mode data and sampled at 200 msec. (b) Frequency spectrum of the centroid location sequence in (a) obtained from its Fourier transform revealing a RM peak corresponding to a period of 4.15 sec. (c) A smoothed RM signal curve obtained from the inverse Fourier transform of the extracting the RM motion peak within the two red vertical bars in (b).

EVALUATION OF EXTRACTED RESPIRATORY MOTION SIGNAL

To quantitatively evaluate the performance of the proposed RM signal extraction methods, we applied two quality assessment methods.

1. SNR of respiratory motion spectrum

The signal-to-noise ratio (SNR) of the centroid location sequence calculated from the list-mode simulation was defined by

$$SNR = \frac{S}{N}, \quad 2\text{-}17$$

where S and N are measured from the frequency spectrum of the signal as shown in Figure 2-7. The S is the amplitude of the RM peak, while N is the average amplitude of the high-frequency noise. A high SNR value indicates more successful detection of RM from the C-ROI centroid location sequence. It can be used as an index of confidence of the respiratory gating signal.

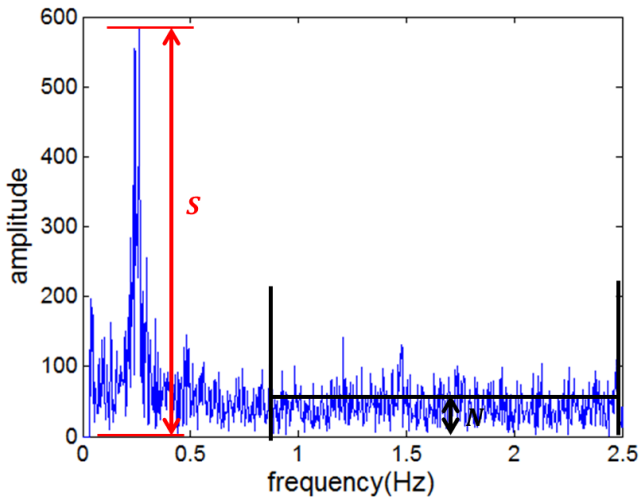

Figure 2-7. The definitions of signal, N, and noise, N, in the SNR measurements.

2. RM amplitude measurement from respiratory gating signal

The RM amplitude was estimated from the RM signal curve obtained from the proposed extraction and post-processing method shown in Figure 2-6. As shown in Figure 2-8(a), the RM amplitude is defined as the range of centroid locations that contains 95% of the total counts. The estimated movement of the myocardium from the respiratory gated images was determined by drawing a profile across the heart along the axial direction and measuring the distance between the myocardium location between different frame as shown in Figure 2-8(b). Since the true RM of the patient is not available, the estimated motion from the reconstructed images is used as the true RM magnitude in the quantitative evaluation.

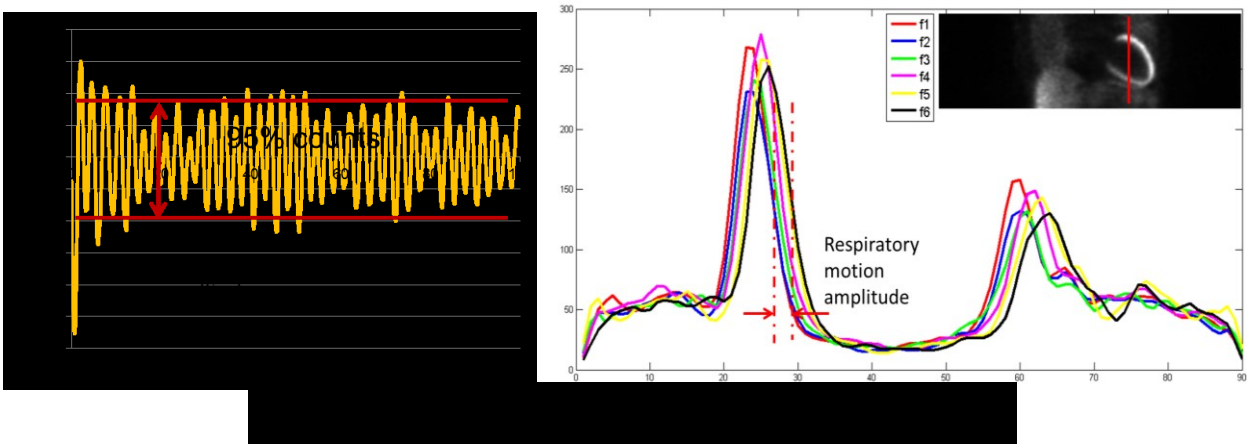

Figure 2-8 (a) respiratory motion amplitude estimation from respiratory motion signal. (b) Verticle profiles through the center of the projection images of the heart at six respiratory gated frames. The RM magnitude is determined from the edges of the myocardium in the gated images with the largest difference.

MATERIALS

Twelve clinical cardiac PET datasets were used in evaluating the proposed RM signal extraction and estimation method. The patient datasets were anonymized before used in the study. The patients were injected with a clinical dose of ^{18}FDG, $^{13}NH_3$ or ^{82}RbCl, and were scanned for 5 to 15 minutes with a Philips Ingenuity TOF PET/CT scanner. Data sets #1 to #3 are ^{18}FDG studies; data sets #4 to #6 are $^{13}NH_3$ studies; data sets #7 to #12 are ^{82}RbCl studies. The acquired PET data with TOF information was stored in list-mode format. The proposed RM extraction and estimation methods were applied to the list-mode data of each patient and the ungated and gated list-mode data were reconstructed using the image reconstruction toolbox provided by Philips.

RESULTS

1. Extraction of RM signal from C-ROI centroid location sequence

Examples of the Fourier transforms or frequency spectra of the extracted C-ROI centroid location sequences from the list-mode data of Patient #1 in Section C and from using the six RM signal extraction methods in Table I are shown in Figure 2-9. Both the RM and CM peaks are visible in all the frequency spectra. Two distinct peaks are identified as the RM peak at 0.35 Hz (or cycles/sec) and as the CM peak at 0.78 Hz. Their magnitudes and the noise of the frequency spectra are lowest with no TOF and background

correction. The S-BC method provides reduced noise in the frequency spectra as compared to that of the D-BC method. With additional TOF information, the frequency spectra show higher RM and CM peak magnitudes and lower noise than those without TOF information. Similar results for the RM peak are found in Patient #3, and Patients #6 to #12. For Patient #6 to #11, the CM peak is not detectable.

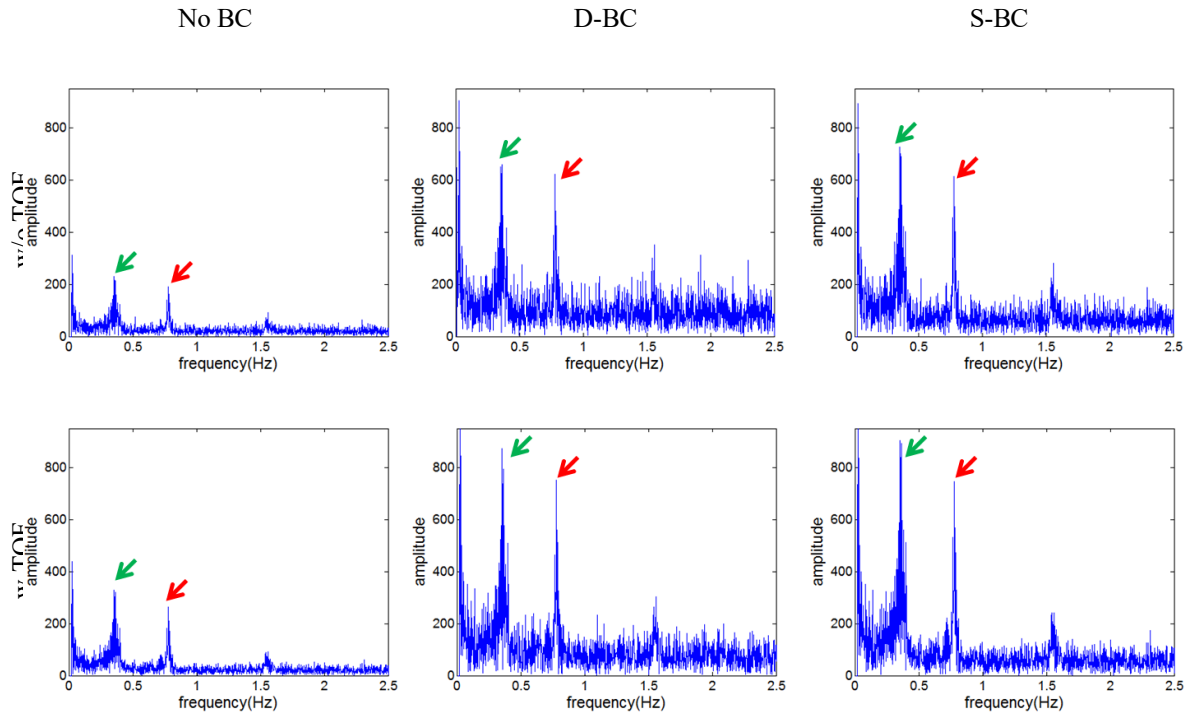

Figure 2-9. The frequency spectra or the Fourier transform of the C-ROI centroid location sequences obtained from list-mode data of Patient #1 using the six RM signal extraction and estimation methods in Table I. From the left to right column, the results are obtained with no background correction and with the D-BC and S-BC methods. The upper and lower rows show results without and with TOF correction. The green arrows point to the extracted RM peaks, while the red arrows point to the CM peaks.

Similar results for Patient #2 are shown in Figure 2-10. For this patient, the RM peak is visible with no background correction and with and without TOF information. When the D-BC method is applied, the noise in the frequency spectrum signal is increased dramatically and obscures the RM signal. The S-BC method lowers the noise in the frequency spectrum to provide a higher RM signal.

No BC D-BC S-BC

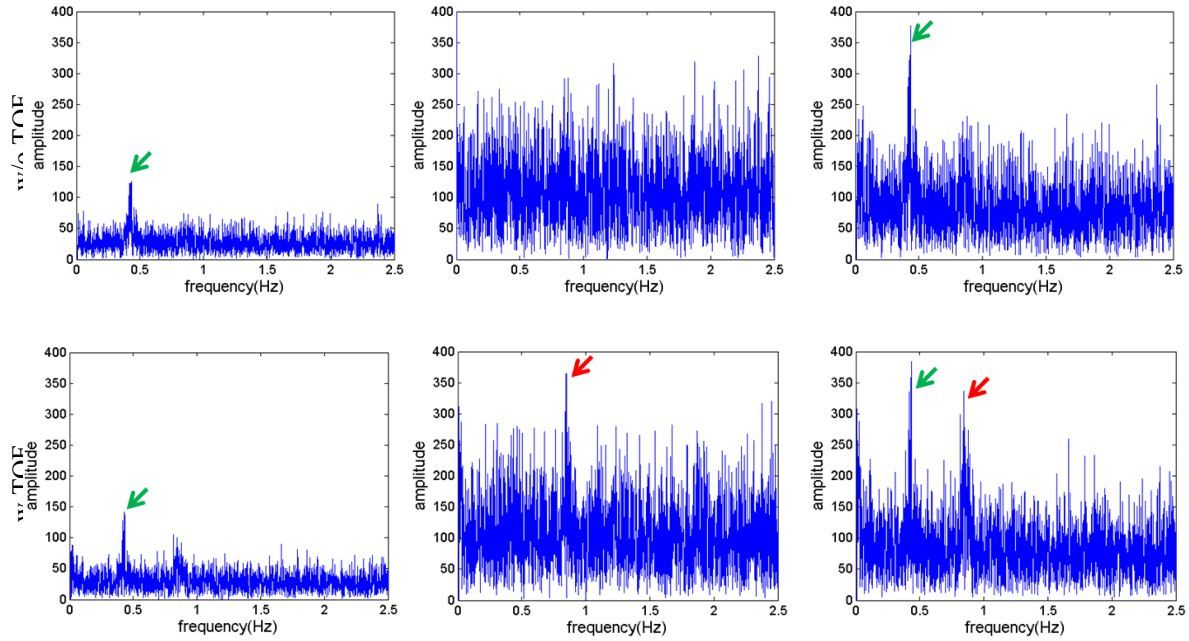

Figure 2-10. Similar frequency spectra as those in Figure 2-9 but obtained from Patient #2. They show the D-BC method gives overly high noise magnitude that obscures the RM signal. The S-BC suppresses the noise magnitude and reveals RM signal with higher magnitude. The green arrows point to the extracted RM peaks, while the red arrows point to the CM peaks.

Similar results from Patient #5 are shown in Figure 2-11. They demonstrate the effect of the background and TOF correction methods in extracting the RM signals. The frequency spectra in the upper row shows that without TOF information, the RM peak is not visible without background correction and is visible with the D-BC and S-BC methods. The frequency spectra in the bottom row show that with TOF information, the RM peak is visible with and without background correction, indicating that TOF information is helpful in extracting the RM signal. Both D-BC and S-BC methods improve the visibility of the RM and CM peaks, while the S-BC method provides lower noise magnitude. Similar results are found in Patient #4.

No BC D-BC S-BC

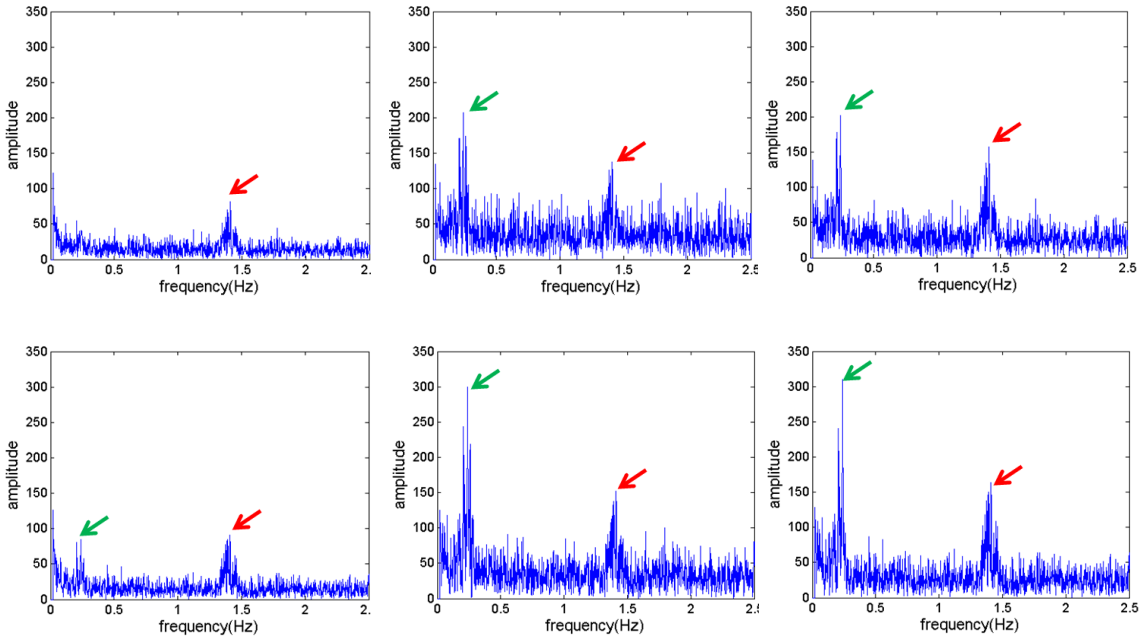

Figure 2-11. Similar frequency spectra as those in Figure 2-9 but obtained from Patient #5 . Results in the bottom row show the TOF correction method provide better visualization of the RM and CM peaks. Also, the RM peak is more visible when the D-BC and S-BC methods are applied as compared to that with no background correction. The green arrows point to the extracted RM peaks, while the red arrows point to the CM peaks.

2. SNR of RM signal

To provide quantitative assessment of the RM signal extraction methods, we computed the signal-to-noise ratio (SNR), defined in 2-17 and Figure 2-8, of the RM signal in the frequency spectra obtained from the 12 patient studies using the different background and TOF correction methods shown in **Error! R eference source not found.**. The results are plotted in Figure 2-12. In cases where the RM signals were obscured by the noise in the frequency spectra shown in the previous section, no SNR measurement was available.

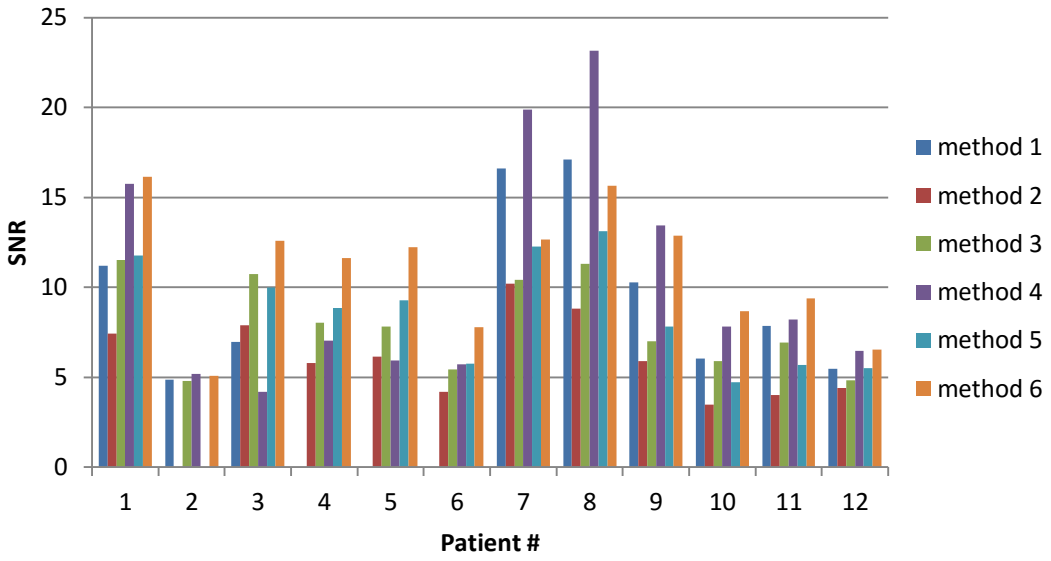

Figure 2-12 SNR of respiratory motion signal for 12 patients with six different methods

In all 12 patients, the introduction of TOF information improves the SNR compared with non TOF information methods, with or without D-BC and S-BC methods. In most cases, the removal of background counts achieved by TOF information provides higher RM signal strength than the concurrent increase in noise in the frequency spectra, resulting in improvement of SNR value. In cases such as Patient #4 to #6, the SNR obtained with Method 4 in **Error! Reference source not found.** is able to extract the RM peak t hat is not available by Method 1. The exception is the case of no background correction for Patient #3. For this patient, the reconstructed image obtained from the ungated data shows higher myocardium-to-background contrast and lower activity in background region as compared to that of the other patients. As a result, the contributions of background counts to the C-ROI are quite small. Meanwhile, the inclusion of TOF information provides improved RM signal strength by reducing the contribution of background counts into the C-ROI. However, in the case, the increased RM signal strength is overpowered by an increase of signal noise, leading to reduced SNR.

The D-BC and S-BC methods have different effect on the frequency spectra. For Patient #1 to #2 and Patient #7 to #12, the SNR is reduced with the D-BC method. For example, in Patient #2, the RM peak is overwhelmed by noise with the D-BC method and becomes invisible. On the other hand, the S-BC method brings up the SNR by reducing the signal noise, resulting in improved SNR than the D-BC method. For Patient #3 to #6, both D-BC and S-BC approaches perform better than without background correction.

Furthermore, the S-BC approach yields higher SNR than the D-BC approach. The main differences between the two groups can be attributed to two factors. First, background subtraction results in increase in noise in the frequency spectra and may lead to loss in the visibility of the RM peak. Second, the background counts often include contributions from the liver part of which may move in and out of the C-ROI during the RM cycle and can affect the background contribution and SNR when it has high tracer uptake. Although background-subtracting increase the RM signal amplitude, it can also lead to increased noise and reduced SNR.

3. RM amplitude estimation

Another quantitative assessment criterion of the six correction methods in Table 2-1 Six RM motion estimation methods based on different combination of TOF and background correction approaches is the estimated RM amplitude calculated from the RM signal extracted from the frequency spectra shown in Figure 2-6. The movement of the myocardial wall measured from the respiratory-gated images of the heart shown in Figure 2-8 was used as the reference for comparison. The results obtained from the 12 patient studies are shown in Figure 2-13. For all the patients, except those with no visible RM signal peak, both D-BC and S-BC methods significantly increase the estimated RM amplitude and bring it closer to the reference RM amplitude estimated from the RM gated images.

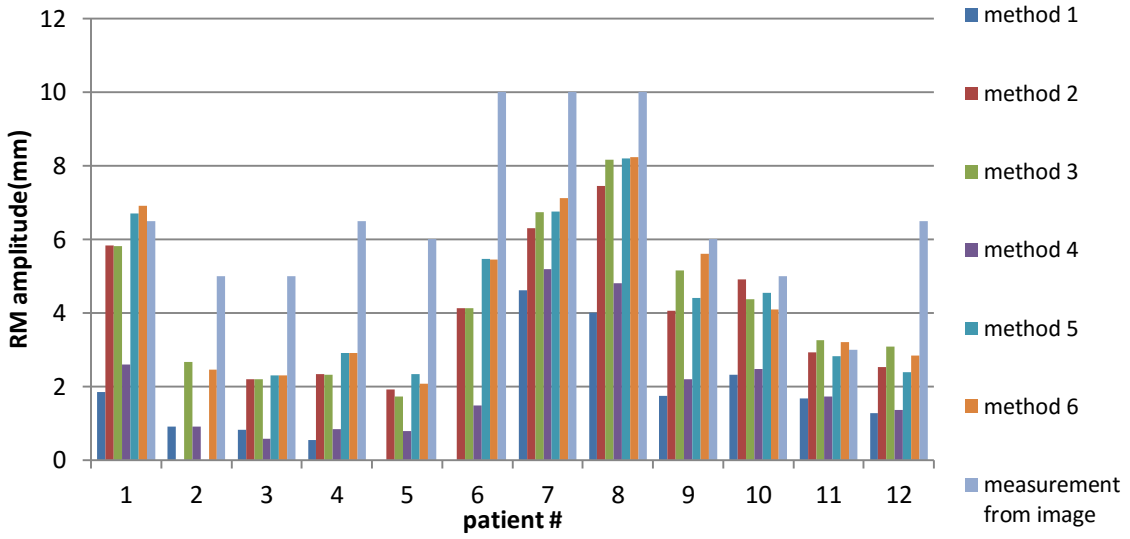

Figure 2-13. RM amplitude of the RM signal extracted from the frequency spectra of the 12 patient using the six background subtraction and TOF correction methods in Table I. The corresponding movement of the myocardial wall measured from the respiratory gated images of the heart is also shown as references.

Increasing the amplitude and accuracy of the RM signal has other useful applications. The higher amplitude allows more accurate determination and it helps distinguish between different respiratory frames, since respiratory gating is essentially amplitude-based. This information is also important if the researcher is interested in respiratory motion correction. It provides first-impression about how much influence of the patient's respiratory motion is on the data. When the respiratory motion of the patient is too small, it may not be necessary to preform respiratory motion correction or respiratory gating.

A noteworthy phenomenon found in Figure 2-9, Figure 2-10 and Figure 2-11 shows an additional benefit of the proposed data-driven RM extraction and estimation method beyond respiratory gating purpose. For some patients, the data-driven method is able to reveal the cardiac motion (CM) peak signal in the frequency spectra of the centroid location sequences of the C-ROI. Using the same data analysis methods for the RM signal extraction, we calculated the SNR of the CM signal from the frequency spectra. Results from patients with visible CM peak signal are shown in Figure 2-14. They show TOF correction provides increased SNR of the CM signal for most patients. In particular, for Patient #6, the frequency spectra with TOF correction brings out CM signal that is unavailable without TOF information even without background correction. Besides factors such as heart to background signal contrast and noise level, there is another factor that can influence the detectability of CM signal extraction. Different from RM signal extraction, the CM signal extraction is not mainly in inferior-superior direction. As a result, the CM signal extracted from the respiratory gated C-ROI sequence only reveal the component of the CM along the inferior-superior direction. However, the extracted CM signal can by useful for cardiac gating purposes in cases when ECG signal is not available.

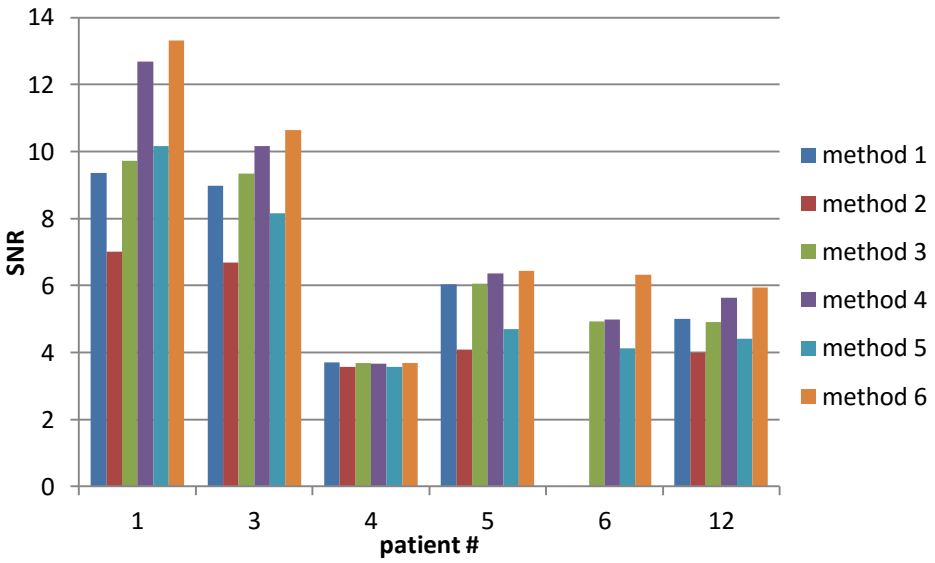

Figure 2-14. SNR of CM signal obtained from applying the six different background subtraction and TOF correction methods in Table I to the twelve patient studies.

DISCUSSION

In our proposed approaches, the extracted RM signal from the cardiac ROI (C-ROI) contains contributions from the heart, liver, and other organs in the chest region. In cardiac PET using ^{18}F-FDG or ^{13}N-NH_3, the activity uptakes in the heart and liver and their contributions to the counts in the C-ROI tend to be higher than that from the other organs. While the motions of the heart and liver contribute to the RM signal extraction, the stationary background reduces the RM magnitude estimation. We sought to improve the accuracy of the RM signal by reducing the contribution from the stationary background, by subtracting the background counts directly or after proper smoothing through background correction, or by reducing counts from the background using the TOF information. For the centroid-tracking based respiratory signal extraction methods, the main factors that affect the RM peak of the extracted motion signal are the respiratory motion amplitude of the heart, the ratio of the uptakes between the heart and the background, and the noise level of the list-mode data. The larger distance the heart moves in axial direction during respiratory cycle, the higher the RM peak in frequency spectrum of the respiratory motion signal. Meanwhile, higher heart activity compared to that of the stationary background and higher count level in the PET data which gives lower noise in the extracted RM signal, also lead to more distinguishable RM peak.

The TOF information is related to the location of annihilation points. By identifying and excluding counts originated from the stationary background, we were able to reduce their effect and improved RM signal estimation in all patient studies with or without background correction.

The performance of the three proposed background correction approaches is different among the 12 patient studies. There are two main factors that influence the contributions from the background counts. First, subtracting noisy background counts from the C-ROI results in higher noise of the extracted centroid location sequence. Smoothing the estimated background counts before subtraction in the S-BC method provides reduced noise and increased SNR of the RM signal as compared to the D-BC method. Second, the background region often contains the liver whose movement contributes to the RM signal. Its subtraction results in reduction of the RM signal strength. Since the liver is close to the heart, it is difficult to completely exclude the liver in the background count extraction. The background correction methods are more likely to improve RM signal extraction in patients with low liver uptake. Since the uptakes in the heart and liver are patient and tracer dependent, analysis of the patient data is necessary before choosing which best background subtraction method to use. In our study, we evaluated only one background count estimation and extraction method. For patients with high liver uptake, an improved background estimation method that excludes contribution from the liver is topic for future study.

An additional CM signal was found in the frequency spectra for some patients. This additional capability was reported previously in analysis of PET data [7]. The proposed RM signal extraction methods can also be used for CM signal extraction, which can serve as an alternative to ECG based cardiac gating.

The number of patients involved in this study was small and may not include all the possible data variations in a large patient population for cardiac PET studies. However, our study can guide further development of data-driven RM and CM signal extraction and estimation methods for use in RM and CM gating and in RM and CM correction for improved PET image quality and quantitative accuracy.

CONCLUSION

Using combinations of TOF information and two background correction approaches, we evaluated six data-driven methods for the extraction and estimation of RM signals from list-mode cardiac PET data. A

cardiac VOI (C-VOI) was selected from the preliminary reconstructed images and its corresponding C-ROI in the sinogram was identified. In TOF-PET studies, the TOF information was used to identify the location of annihilation events originated from within the C-VOI. The C-VOI centroid was calculated in 200ms intervals by down weighting the contributions from outside the C-VOI. Random coincidence and detector sensitivity were corrected by delay-event subtraction and normalization using experimentally measured detector sensitivity coefficients, respectively. Detected counts from the stationary background within the C-ROI lowered the amplitude of the RM peak signals and made the signal extraction difficult. Reduction of the contributions of stationary background from the C-ROI enhanced the RM peak signal amplitude but could often lead to increased noise in the frequency spectra. The six RM signal extraction and estimation methods listed in Table I represented different trade-offs between RM signal enhancement and noise reduction. These methods were evaluated using data from 12 clinical cardiac PET studies.

Among the six RM signal extraction methods, the background subtraction correction methods with or without smoothing increased the amplitude of the processed RM signal, compared with no background correction. However, the effects of background subtraction on the frequency spectra of the centroid location sequence were data-dependent. For patient data with high statistical noise fluctuations and high liver uptake, the background signal could be noisy and contain RM information. Its subtraction could lead to increased noise and reduced RM signal amplitude, resulting in decreased SNR of the RM peak signal in the frequency spectra. In some extreme cases of high data noise, the frequency spectra obtained with background subtraction did not reveal any visible RM signal peak. In cases where the patients had low liver uptake and high detected counts or low data noise, background subtraction provided enhanced RM peak signal that allowed more reliable RM signal extraction. With smoothing of background counts before subtraction, the SNR of the RM peak signal could be further improved by reducing the noise amplification in data subtraction. Meanwhile, the TOF information demonstrates significant advantage in RM signal extraction. Method 4 and Method 6 in Table 2-1, both utilizing the TOF information, successfully extracted the RM signal for all twelve patient data sets.

Since the characteristics of different patient datasets can be quite different, the selection of the optimal RM signal extraction method is important to provide the best SNR of the RM signals.

CHAPTER 3. FEATURE-BASED CARDIAC MOTION ESTIMATION

PRELIMINARY STUDY

The main purpose of the preliminary study is to test the idea of incorporating feature in to cardiac motion estimation. In this study, we proposed a feature-guided motion estimation approach to improve the accuracy in cardiac motion estimation for cardiac PET images. The basic idea is to create an initial MVF estimate closer to the true cardiac motion than the traditional zero-valued MVF. Using realistic digital phantom and analytical simulation tool, we extracted the anatomical features from simulated cardiac PET images and used the motion of the features to guide the cardiac motion process. The motion estimation results were evaluated quantitatively.

METHODS

FEATURE EXTRACTION

There are two major anatomical features in human heart—the papillary muscles and the interventricular sulcus. With advanced medical imaging techniques, these small structures of the heart become increasingly visible, which brings prospect of feature based motion estimation. Located in the ventricles of the heart, the papillary muscles control the motion of tricuspid and bicuspid valves through a bundle of connecting muscles. The "footprint" of the papillary muscle is where the root of the papillary muscle connects the endocardium. The interventricular sulcus is the connection between the left ventricle and the right ventricle. Figure 3-1 shows both features of the human heart using the 4D XCAT phantom. These features contain useful information about the motion of the myocardium, especially motion that is difficult to detect using traditional method.

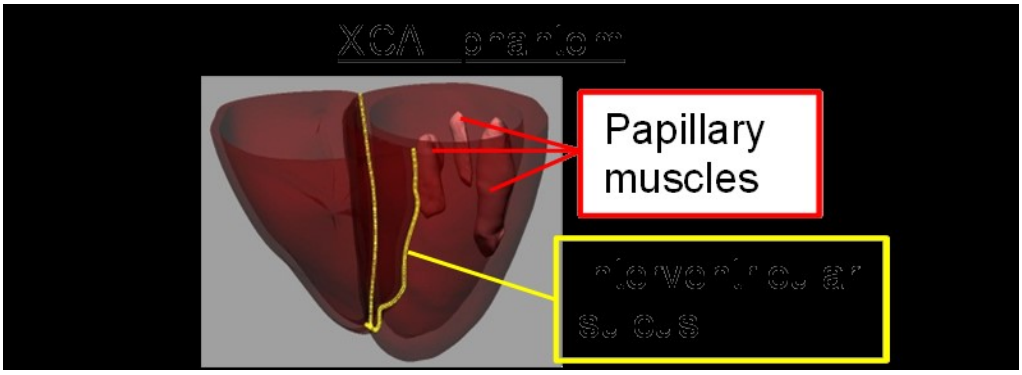

Figure 3-1 Anatomical features of human heart demonstrated using the 4D XCAT phantom. The internventricular sulcus is highlighted by the yellow curve. The papillary muscles are the small pieces of muscles that locate inside the left ventricle.

To extract the "footprint", first the seeded 3D region growing method[88] was used to segment out the blood pool inside the left ventricle in short-axis cardiac images based on the intensity difference between the blood pool and the myocardium. In each short-axis slice, we find the shape of the blood pool is concave due to the intruding papillary muscle. Hence we extracted the papillary muscle by subtracting the convex hull[89] of the blood pool with the blood pool itself, and then found the root of the papillary muscle. The centroid of the "footprint" of the papillary muscle is calculated from the extracted area, and its motion is tracked during the cardiac cycle by repeating the extraction in every time frame. The extraction process is demonstrated in Figure 3-2(a), and the extracted centroid is shown in Figure 3-2 (b).

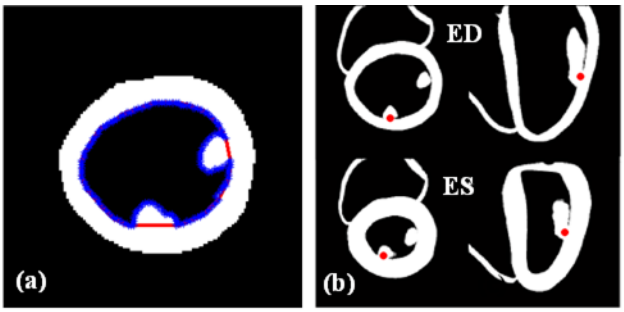

Figure 3-2 (a) Extraction of the "footprint" of the papillary muscle in short axis view of the phantom image. Blue curve: outline of the blood pool. Red line: convex hull of the blood pool. (b) The centroid shown in the short-axis and long-axis view of the XCAT phantom images of end-diastolic phase and end-systolic phase.

For the interventricular sulcus, first, we used the 3D region growing method to segment out the whole myocardium from the background. Noticing that the thickness of the right ventricle is distinctively smaller than that of the left ventricle, we applied 3D erosion to the extracted myocardium followed by 3D dilation to

remove the right ventricle and keep only the left ventricle. After successfully separating the right ventricle and the left ventricle, we identified the pixels that connect these two parts on each short-axis slice as the sulcus points. Figure 3-3(a) shows the extraction process on one slice of the phantom image. After extracted the interventricular sulcus points on each slice, the entire sulcus curve as in Figure 3-3(b) can be obtained by connecting these points and smoothing the curve.

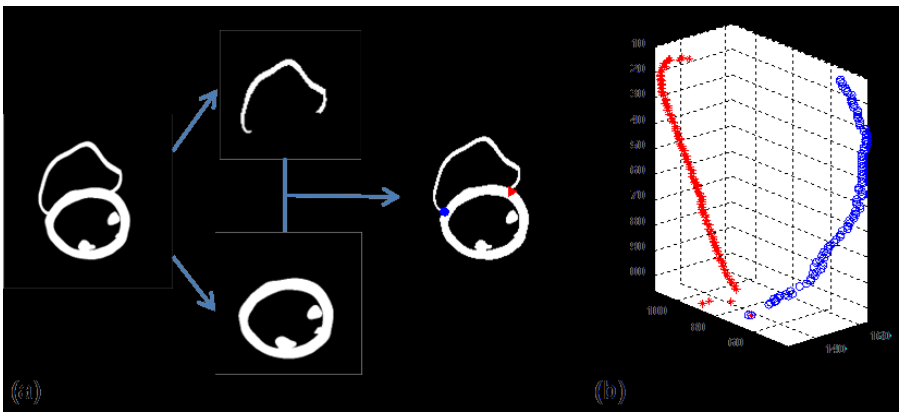

Figure 3-3 (a) Extraction of the IS from frame 1 of the phantom image. The blue dot indicates the anteior IS while the red triangle indicate posterior IS. (b) The extracted IS from frame 1 of the phantom image. Blue circles indicates the anterior IS while the red stars indicate the posterior IS.

FEATURE GUIDED MOTION VECTOR FIELD INITIALIZATION

Information contained in the extracted motion of the above-mentioned features is regional, but the motion of the feature is extended to the whole myocardium based on knowledge about human cardiac motion. The optical flow based motion estimation algorithm generally requires an initial MVF to start the optimization process. Zero-valued MVF is usually used as the initial, but without the prior knowledge of the cardiac motion, it tends to converge to a local minimum, which is not the true MVF. A cardiac MVF initialized using the motion information contained in the features reduced the null space and could be closer to the true MVF.

Based on the anatomy of human heart, cardiac motion is divided into three components as shown in Figure 3-4 (a). Clinical studies have found relationships between each motion component and the location in myocardium. In other words, the motion of a certain voxel of the myocardium is related to its location in the whole heart. Based on clinical studies of normal patients, we have two sets of assumptions about the

three cardiac motion components. Along the longitudinal direction: 1) the radial motion is approximately proportional to the radius of the left ventricle on short-axis plane; 2) the circumferential motion is linearly related to the distance to the apex, and there is a non-twisting plane at the 2/3 of long axis length from the apex [90, 91]; 3) the longitudinal motion is also linearly related to the distance to the apex, and the apex shows nearly zero longitudinal motion [90-92]. Along the transmural direction on each short-axis slice, radial and circumferential linearly decrease by half from endocardium to epicardium, while the longitudinal motion is uniform [90]. The linear relationships in these assumptions are approximations based on previous clinical study results. The magnitude of three motion components on each short-axis slice in the 4D XCAT phantom is plotted in Figure 3-4(b), which is consistent with clinical data and proves our assumptions are reasonable.

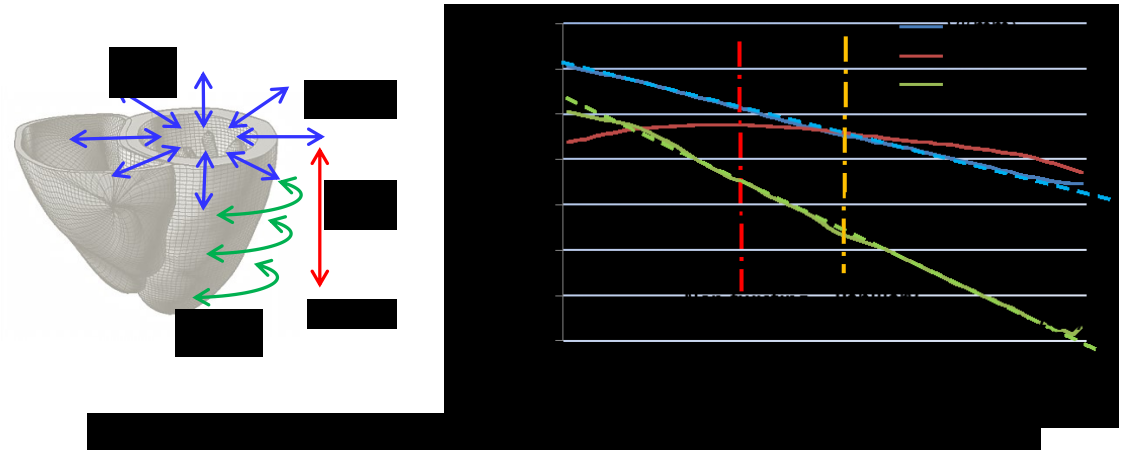

Figure 3-4 (a) Three cardiac motion components shown using the 4D XCAT phantom. (b)The magnitude of three motion components along the longitudinal direction. Data collected from the 4D XCAT phantom.

1. PAPILLARY MUSCLE GUIDED MVF INITIALIZATION

An initial estimation of the cardiac MVF was created using the extracted papillary muscle in two steps. First, the values of three motion components at the endocardium on each short-axis cross-section were extrapolated from the motion of the centroid using

$$\widehat{V_l}(s) = k_l \cdot s + b_l,$$

3-1

$$\widehat{V_r}(s) = r(s) * p_r,$$

3-2

$$\widehat{V_c}(s) = \widehat{V_c}(s_p), \forall s,$$

3-3

in which $\widehat{V_l}(s)$, $\widehat{V_r}(s)$, $\widehat{V_c}(s)$ represents the longitudinal, radial, and circumferential motion at the endocardium of short-axis slice s respectively, s_p is the short-axis slice number of the papillary muscle centroid. In 3-1, the slope and intersect are determined from the longitudinal motion of the centroid using

$$k_l = V_l(s_p)/(s_p - s_a),$$

3-4

and

$$b_l = -k_l \cdot s_a,$$

3-5

in which s_p and s_a are the short-axis slice number of the papillary muscle and the apex respectively. In (2), $r(s)$ is the radius of the endocardium at short-axis slice s, and the scalar is calculated using the radial motion and the radius of the footprint centroid by

$$p_r = \widehat{V_r}(s_p)/r(s_p).$$

3-6

In 3-3, with no information about the circumferential motion of the heart except at the papillary muscle footprint, the circumferential motion of every slice is initialized using the same value as the circumferential motion of the papillary muscle footprint.

With the motion at the endocardium determined, the second step is to initialize the MVF on each short-axis slice from the endocardium to the epicardium. Radial motion and the circumferential motion can be calculated using

$$\widehat{Vr}(R) = \frac{R + R_a - 2R_b}{R_a - R_b}\frac{1}{2}\widehat{Vr}(R_a)$$

3-7

$$\widehat{Vc}(R) = \frac{R + R_a - 2R_b}{R_a - R_b}\frac{1}{2}\widehat{Vc}(R_a)$$

3-8

As demonstrated by Figure 3-5, R is the radius of the transmural ring, R_a and R_b are the radius of the endocardium and epicardium respectively. The longitudinal motion is initialized uniformly on each slice. The three motion components of the whole left ventricle extrapolated in the above two steps are then transformed into the laboratory coordinate system for use in motion estimation process. Thus, the MVF of the whole myocardium has been initialized using the information from the papillary muscle.

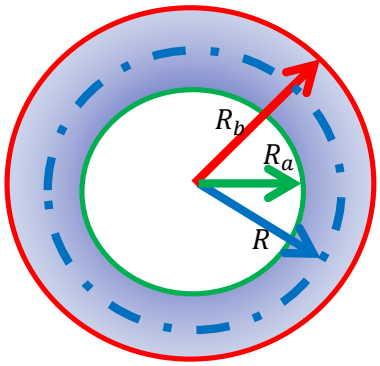

Figure 3-5 Initialization of the cardiac MVF on short-axis cross section.

2. INTERVENTRICULAR SULCUS GUIDED MVF INITIALIZATION

Using the extracted motion of the interventricular sulcus, we created an initial MVF for the left ventricle based on the same sets of assumptions. After extracting the sulcus, the motion of the sulcus between two time frames was calculated and decomposed into three components. Based on the change of the longitudinal length of the sulcus, the longitudinal motion on each short-axis slice of the left ventricle is initialized linearly. The circumferential motion at the epicardium of each slice is determined by linear regression analysis of the circumferential motion of the sulcus. The radial motion on the epicardium of each slice is initialized by smoothing the radial motion curve of the sulcus. The extracted motion components and fitted curve of the interventricular sulcus in frame 1 is shown in Figure 3-6.Then the radial motion and circumferential motion are initialized transmurally using

$$\widehat{Vr}(R) = \frac{R+R_a-2R_b}{R_a-R_b}\widehat{Vr}(R_b),$$

3-9

and

$$\widehat{Vc}(R) = \frac{R+R_a-2R_b}{R_a-R_b}\widehat{Vc}(R_b).$$

3-10

By transforming the three initialized motion components into the laboratory coordinate, an interventricular sulcus guided initial MVF was created for the left ventricle and named as S-initial.

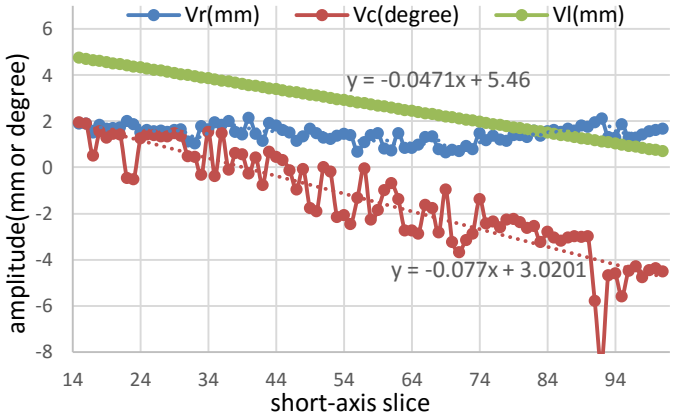

Figure 3-6 Three motion components of the anterior interventricular sulcus extracted from the phantom image frame 1. Fitted (broken lines) curves were used build the S-initial estimation of the cardiac motion.

OPTICAL FLOW BASED MOTION ESTIMATION ALGORITHM

The estimation of the 4-D MVF is through a previously proposed [76] and implemented [93] optical flow based motion estimation algorithm in which the cost function consists of an intensity mismatching term $E_I(\boldsymbol{m})$and a weighted elastic energy term $\alpha E_S(\boldsymbol{m})$. These two terms are defined in the following equations.

$$\boldsymbol{E_I(m)} \triangleq \sum_r \left[\boldsymbol{f_1(r)} - \boldsymbol{f_2}\left(\boldsymbol{r} + \boldsymbol{m(r)}\right)\right]^2,$$

3-11

$$E_S(\boldsymbol{m}) \triangleq \frac{1}{2}\sum_r(\lambda(u_x + v_y + w_z)^2) + \sum_r\left(\mu\left(u_x^2 + v_y^2 + w_z^2\right)\right) + \frac{1}{2}\sum_r(\mu\left[\left(u_y + v_x\right)^2 + (u_z + w_x)^2 + \left(v_z + w_y\right)^2\right]),$$

3-12

where $\boldsymbol{m}$ is MVF estimate, u, v and w are the components of $\boldsymbol{m}$ in the x, y and z directions, $\boldsymbol{r}$ is the 3D spatial coordinate of a voxel, f_1 and f_2 the reconstructed image at two adjacent time frames. The first term

$E_I(\boldsymbol{m})$ is approximated by its first order Taylor series. The weight α was set to 0.005 and the Lame constants were chosen according to Mair [82]. The cost function is optimized using an iterative conjugate gradient algorithm, and the MVF is obtained as the minimizer after 30 iterations with guaranteed convergence.

For comparison and evaluation, four initial MVF estimates were used in phantom study: (1) the 0-initial which is a zero valued MVF, which contains no motion information; (2) the P-initial which is the initial MVF extrapolated from the extracted motion of a papillary muscle; (3) the S-initial which is the initial MVF extrapolated from the extracted motion of the interventricular sulcus; (4) the T-initial which is the true MVF of the heart model of the XCAT phantom. Among these four initials, the 0-initial is the typical initial used in motion estimation; the P-initial and the S-initial are MVF initialized using our proposed feature based method; and the T-initial is included here for comparison, but it is not available in realistic situations.

MATERIALS AND EXPERIMENT DESIGN

INTRODUCTION TO SIMULATION TOOLS

This study mainly relied on simulated cardiac PET data to implement and evaluate the proposed methods. The 4D XCAT phantom provides anatomy and motion of human body. In preliminary study, we used analytical simulation tool STIR to generate projection data and reconstruct cardiac images.

The 4D NURBS-based Cardiac-Torso (XCAT) phantom [94] developed in our group is a digital anthropomorphic phantom widely used in nuclear medical imaging study. It provides highly realistic anatomy of human body derived from CT images and modeled with non-uniform rational b-splines (NURBS) surfaces. Moreover, it also provides realistic 4-D respiratory and cardiac motion which was determined from set of 4-D tagged MR cardiac images, and the respiratory motion came from a 4-D high resolution respiratory-gated CT dataset respectively. In this study, the XCAT phantom was used to generate activity map and attenuation map for simulation of cardiac PET scan.

In this study, a newly updated 4-D XCAT phantom featuring a 4-D beating heart model with known cardiac MVF was employed to simulate myocardial perfusion (MP) PET images for implementation and evaluation of the proposed motion estimation method. As a realistic anthropomorphic phantom widely used in medical imaging, the 4-D XCAT phantom provides both activity and attenuation maps of the human

body and allows for simulation of medical image data with known medical imaging processes. The update of the phantom includes the addition of two papillary muscles that are attached to the endocardium of the left ventricle of the heart model. The locations and shapes of the papillary muscles were determined from a 4-D cardiac-gated CT image dataset with 10 time frames over one cardiac cycle. The 4-D MVF of the original XCAT phantom was determined from a set of 4-D tagged MR cardiac images. The 4-D XCAT phantom also provides realistic MVF, which serves as a reference to evaluate the performance of the proposed cardiac motion estimation method.

Figure 3-7 (a) shows the heart model in the 4-D XCAT phantom, and the MVF of four sample slices of the left ventricle is plotted in (b).

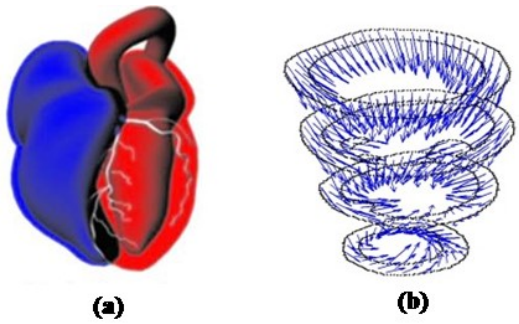

Figure 3-7(a) Surface renderings of the cardiac model of the XCAT. (b) True MVF of the XCAT phantom at four sample slices of the left ventricle are plotted as blue arrows.

STIR (Software for Tomographic Image Reconstruction) is an open source software mainly for 3D PET image reconstruction [95]. It provides several image reconstruction methods such as FBP and OSEM-One Step Late algorithm, as well as functions such as scatter correction and motion correction. In this study, we used its forward projection function to generate analytical projection data for the heart region, in order to speed up our simulation.

HIGH-RESOLUTION ANALYTICAL SIMULATION

The 4-D XCAT phantom data set consists of a series of 3-D images representing 8 time frames which uniformly distribute over a one-second cardiac cycle starting from the end-diastolic (ED) phase. Each of the 3-D phantom images was digitized into a 128×128×128 matrix with a voxel size of $(0.078\ \text{cm})^3$. The end-systolic (ES) phase was set at 0.4 second while the mid-diastolic (MD) phase was at 0.7 second from

the R-wave. Activity concentration was set to the myocardium only to simulate the activity distribution of an ideal perfusion tracer in human body. The known MVF of the beating heart of the 4-D XCAT phantom was used as the ground truth. Noise-free cardiac-gated MP PET projection datasets were generated from 3-D XCAT phantom at each time frame using the STIR simulation software [95] modeling the imaging characteristics of a modified GE Discovery RX PET scanner with improved resolution. Parameters of the customized 3-D PET scanner are provided in Table 3-1. Image degrading factors such as detector response, position range, nonlinearity, and scatter were not included in the simulation of projection, so the system resolution is equal to the bin size. The purpose of simulating this non-existing PET imaging system is to generate high quality images for preliminary implementation and evaluation of the proposed method, since extraction of the features demands high resolution. Poisson noise was added to the projection data after normalizing the total counts in the sinogram of the center slice to 6000, which is 8 times of typical clinical counts of a 40-minute PET scan. The projection data were processed using the OS-EM image reconstruction method provided by the STIR software to obtain reconstructed images. Butterworth filter with a cutoff frequency of 0.1 cycle/voxel and order 6 was applied to the noisy reconstructed images to mimic standard clinical process. One sinogram of the center slice of the XCAT heart phantom at ED before adding noise was shown in Figure 3-8 (a), while (b) and (c) show one middle slice of the reconstructed image before and after filtering.

Table 3-1 Parameters of the customized scanner

Number of rings	65
Number of detectors per ring	1600
Inner ring diameter (cm)	88.62
Average depth of interaction (cm)	0.94
Distance between rings (cm)	0.156
Default bin size (cm)	0.078

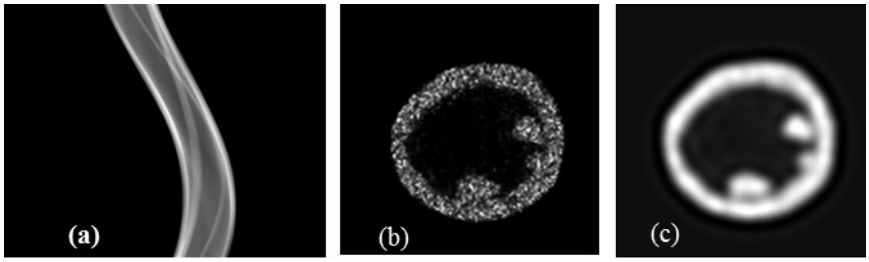

Figure 3-8 (a) The simulated noise-free sinogram of the center slice of the heart model of the XCAT phantom. (b) Reconstructed PET image of the noisy projection data. (c) Reconstructed PET image after application of the Butterworth filter.

Using the proposed method, features were extracted from each time frame of phantom image and simulated PET image. Then all cardiac images were down-sampled by 2, and initial cardiac MVFs between each two time frames of down-sampled image were created using the motion information contained in the features. The initial MVFs were combined with the optical-flow based motion estimation method to estimate the cardiac MVF in the down-sampled images.

RESULTS

The motion of the myocardium between neighboring frames of the 8 frames in total has different magnitudes. The heart starts to contract from the first frame and reaches end-systolic phase shortly after frame 3, and then start to relax since frame 4 until the last frame. The average magnitude of the cardiac MVF in 8 frames of phantom images are provided in Figure 3-9, in which we can find that frame 1, 2, 5, and 6 have relatively larger cardiac motion than the other four frames. Among the 8-frame cardiac images, frame 1 has the largest contracting motion during the systolic phase while frame 5 has the largest relaxing motion during the diastolic phase.

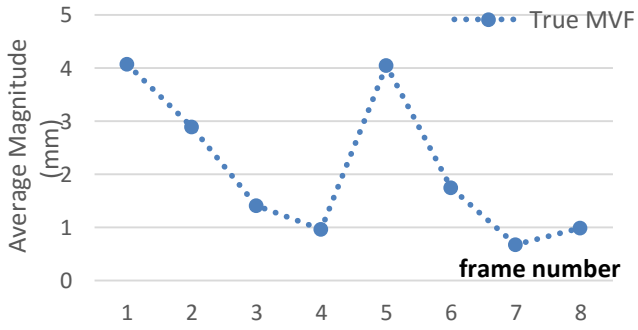

Figure 3-9 Average magnitude of the true MVF in eight frames of phantom images.

For IS, using the proposed feature extraction method, we were able to identify the sulcus location and calculate the three motion components of the sulcus curve from the phantom images and simulated high-resolution PET images. However, for the papillary muscle, although we were able to obtain the centroid location of the footprint in each cardiac frame, we found that the motion of the centroid was inconsistent with the cardiac MVF. The inconsistency will be studied in next section. At this stage, as the main purpose is to preliminarily test the idea of feature-based cardiac motion estimation, we decided to use the true motion of the calculated centroid point in the first frame for MVF initialization.

The motion estimation results using the 0-initial, P-initial, S-initial and T-initial in frame 1 and frame 5 of phantom image and simulated PET images are shown in Figure 3-10and Figure 3-11 with the true MVF as reference. In Figure 3-10, the heart is contracting. In the highlighted basal region in, the true motion vectors represented by the blue arrows show both radial motion and longitudinal motion, both of which contribute to the contraction of the myocardium. The MVF estimated using the 0-initial in Figure 3-10 (c) are mainly pointing toward the center of the heart, showing the radial motion and negligible longitudinal motion. As a result, the longitudinal motion is significantly underestimated with the 0-initial. The motion vectors estimated using other three initial MVF are closer to the true MVF, showing more accurate estimation of the longitudinal motion. Results from simulation data are similar to those from the phantom images. In Figure 3-11, the heart is relaxing. The highlighted short-axis region is experiencing outward radial motion and counter-clockwise circumferential motion. The motion estimated with 0-initial shows mainly radial motion, while results of the other three initials show both motion components. The results of S-initial provide more accurate approximation of circumferential motion, which is difficult to detect using the conventional method due to aperture problem. Results of the P-initial shows overestimated Vc because the circumferential motion of every short-axis is initialized with the same value as the papillary muscle centroid. T-initial achieves most accurate results in both phantom images and simulated cardiac PET images. This indicates accurate initial estimate is crucial to obtain accurate estimation of the true MVF, even for the circumferential motion.

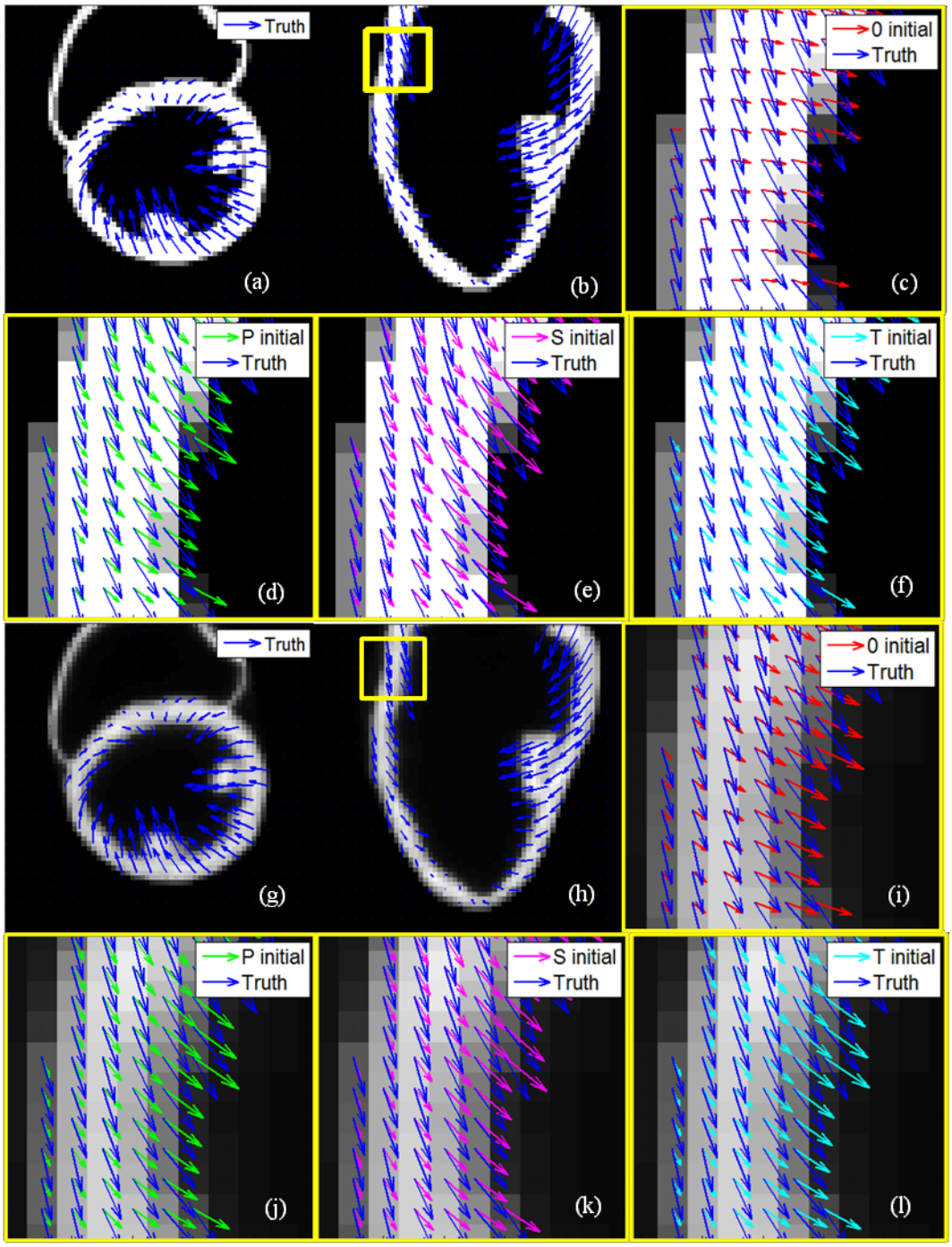

Figure 3-10 The "true" and estimated cardiac MVF obtained with four initial MVF from the phantom image at frame 1. The true MVF of the myocardium is shown in (a) short-axis and (b) vertical long-axis views. Regions surrounded by the yellow squares in (b) are zoomed in to provide a closer look at the details. MVFs estimated using the 0-initial, the P-initial, the S-initial and the T-initial in the squared region are displayed in (c), (d), (e) and (f), respectively, and the true MVF of this region is shown as reference. Similar results for simulated PET images are shown in (g)-(i).

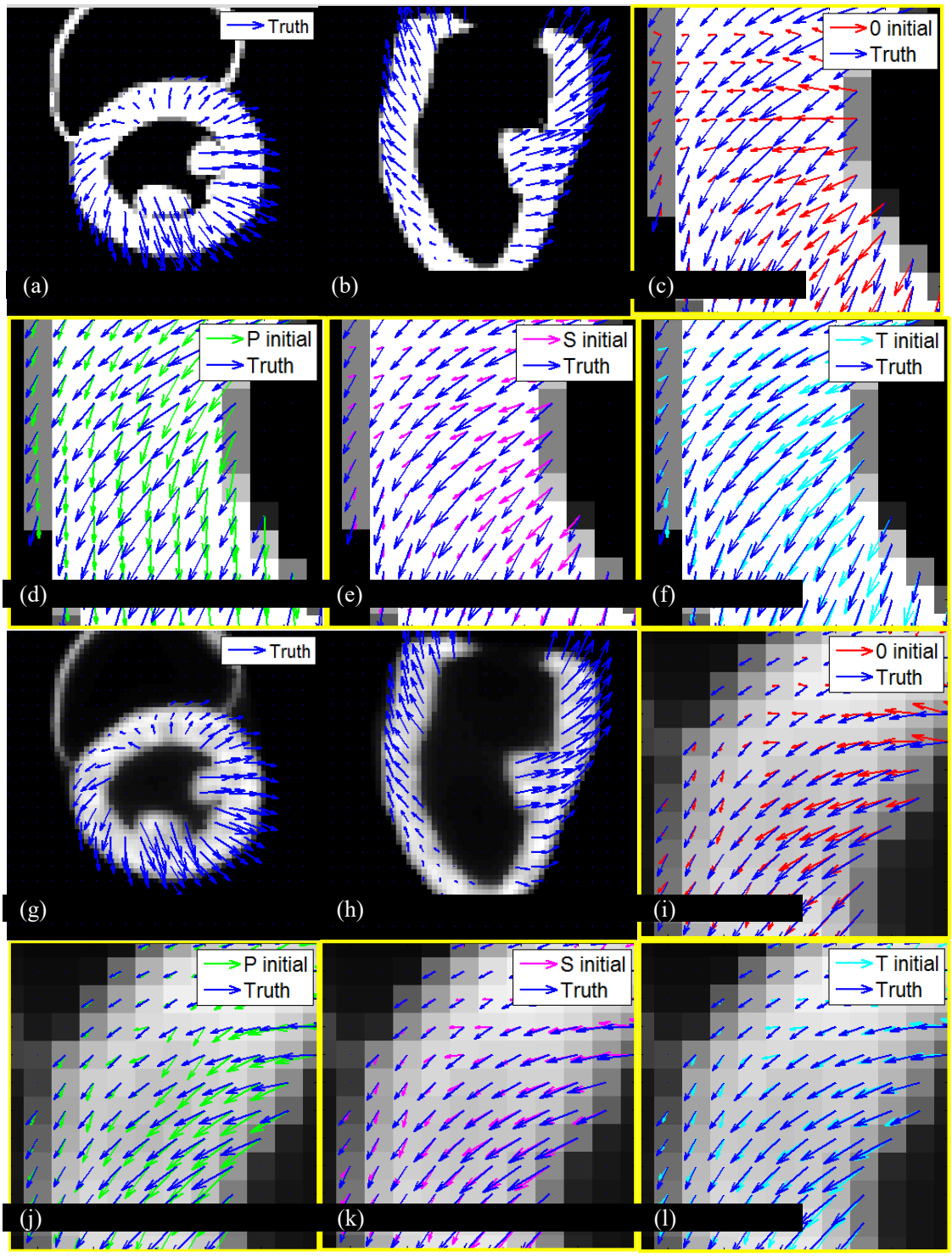

Figure 3-11 The "true" and estimated cardiac MVF obtained with four initial MVF from the phantom image at frame 5. The true MVF of the myocardium is shown in (a) short-axis and (b) vertical long-axis views. Regions surrounded by the yellow squares in (b) are zoomed in to provide a closer look at the details. MVFs estimated using the 0-initial, the P-initial, the S-initial and the T-initial in the squared region are displayed in (c), (d), (e) and (f), respectively, and the true MVF of this region is shown as reference. Similar results for simulated PET images are shown in (g)-(i).

The estimated 4-D cardiac MVFs for each time frame were compared with the true cardiac MVF of 4-D XCAT phantom to determine their quantitative accuracy. We calculated the absolute error in three motion components at each voxel and showed the motion estimation error in the form of a polar map. Figure 3-12is the polar map for the error in three motion components of simulated PET image at frame 1. Errors in three motion components show similar distribution in the myocardium. The basal region tends to have larger motion estimation error than the apical region. This is consistent with the fact that the cardiac motion at the basal region is larger than other region. For the longitudinal motion, its larger error at the basal region is also cause by the fact that its direction gets tangential to the edge of the myocardium at the basal region. The longitudinal motion has larger error than the other two components, and the improvement in the motion estimation accuracy mainly lies in this component. Since the longitudinal motion is the largest motion component in magnitude and the most underestimated, initializing this component properly could significantly improve the motion estimation accuracy. The error in radial motion is small even with the 0-initial, because its direction is perpendicular to the edge of the heart. Error in the circumferential motion is large at the apex, because when the short-axis radius gets very small, the estimation of circumferential motion will get very difficult. Both P-initial and S-initial achieve more accurate estimation of radial and longitudinal motion than the 0-intial. However, due to inaccurate initialization of circumferential motion, the P-initial yields larger error for circumferential motion at the basal region.

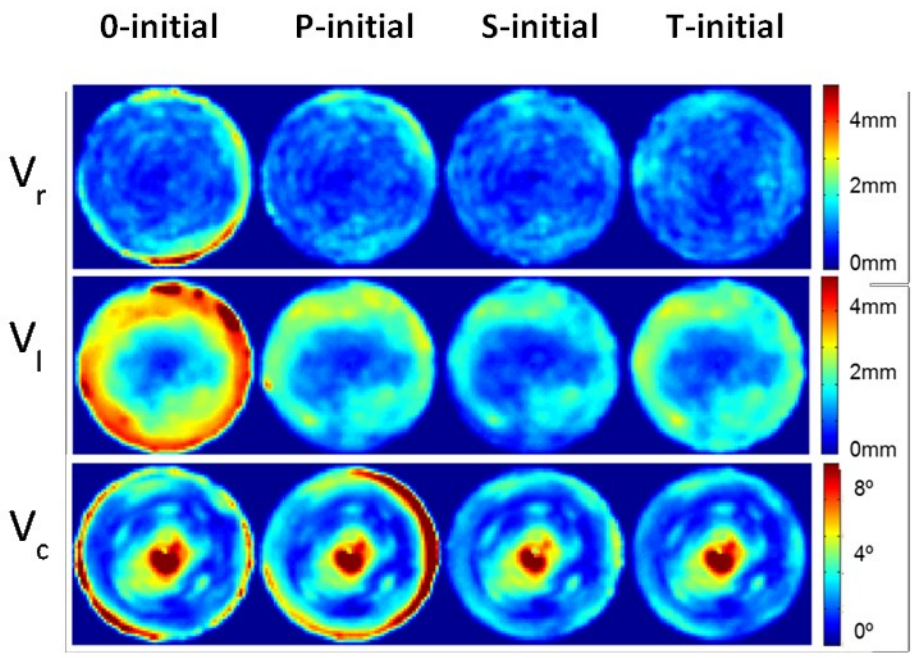

Figure 3-12 Polar map of motion estimation error in simulated PET images of Frame 1. The first row shows the error of radial motion in the myocardium, the second row shows the error in circumferential motion, and the third row shows the error in longitudinal motion. The four rows represent the results of 0-initial, P-initial, S-initial and T-initial respectively. The error of radial and longitudinal motion is in unit of millimeter, while the error of circumferential motion is in unit of degree.

For global quantitative evaluation of the cardiac motion estimation accuracy of the whole myocardium, we used the error of estimated MVF measured by in terms of the root mean-square-error (RMSE) over the entire myocardium of the left ventricle by

$$\boldsymbol{RMSE} = \sqrt{\frac{1}{N}\sum_{i=1}^{N}\|\boldsymbol{MVF}_{est}(\boldsymbol{u},\boldsymbol{v},\boldsymbol{w};\boldsymbol{i}) - \boldsymbol{MVF}_{tr}(\boldsymbol{u},\boldsymbol{v},\boldsymbol{w};\boldsymbol{i})\|_2^2}, \quad \text{3-13}$$

where N is the total number of voxels over the entire myocardium; $\boldsymbol{MVF}_{est}(u,v,w;i)$ and $\boldsymbol{MVF}_{tr}(u,v,w;i)$ are the estimated MVF and the true MVF of voxel i, respectively; u,v,w represent motion in the x,y,z directions; and $\|\boldsymbol{V}\|_2$ is the l_2 norm of vector $\boldsymbol{V}$.

The motion estimation error using four initial MVFs in 8 time frames of simulated PET images is provided in Figure 3-13. In frame 1, 2, and 5, the P-initial achieves lower global error than the 0-initial. S-initial achieves even better performance than the P-initial and comparable motion estimation accuracy as

the T-initial in both phantom images and simulated PET images. This is reasonable since the interventricular sulcus can provide more information of the cardiac motion than the papillary muscle, leading to more accurately initialized cardiac MVF. The motion estimation error of S-initial is even slightly lower than that of the T-initial in frame 1 and 5 of simulated PET images, but not so in phantom images. This may be caused by the noise, since there is only one noise realization in the simulated PET study. Another explanation is that in phantom images the intensity is uniform in the myocardium, which provides little help for the optical flow algorithm to find the motion that causes intensity change, while in simulated PET images, blurring by system resolution and smoothing introduces intensity changes near the boundaries of the myocardium. Even among the four large-motion frames, it is noticed that in frame 1, 2 and 5, the feature-guided initials provide better performance than in frame 6, which has smaller motion than others do. For frames with very small motion (frame 3, 4, 7, 8), the four initial estimations provide similar results in terms of accuracy. Meanwhile, the RMSE for these four frames are comparable with the average amplitude of the true MVF, indicating that motion estimation for small-motion frames is inaccurate. Since the voxel size is $(1.56\text{mm})^3$, the accuracy of motion estimation is approaching the limitation of the image resolution.

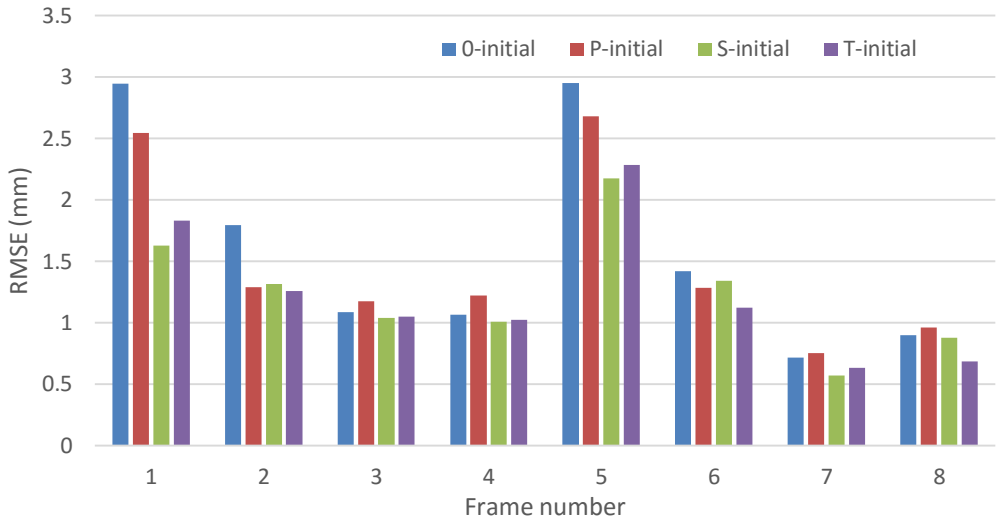

Figure 3-13 RMSE of the estimated MVFs of four initials in simulated low-noise PET images of 8 time frames with frame 1 as ED. In frames of significant cardiac motion, feature-guided initial MVFs can improve the accuracy of motion estimation.

To have a comprehensive understanding of the motion estimation error, we compared the three motion components of the estimated MVF with the true MVF and calculated the error of each component

individually. The motion estimation errors in three components using the four initial MVFs in frame 1 of simulated PET images are shown in Figure 3-14. Among three components, the radial motion is the easiest to estimate, since it is perpendicular to edges of myocardium. The circumferential motion is the most difficult due to the aperture problem. The bar for the error in the circumferential motion may look higher than the other two components in the figure. This is because the circumferential motion is measured in degree, while radial and longitudinal motion are measured in millimeter. In fact the circumferential motion contributes the least to the total motion estimation error. Moreover, the errors in both radial and longitudinal motion are smaller than the magnitude of the true motion components, while the error in circumferential motion is higher than the magnitude of the true circumferential motion. This indicates that radial and longitudinal motion can be estimated much more accurately than the circumferential motion. Longitudinal motion is improved the most because its magnitude is the largest. All three components were more accurately estimated using the S-initial MVF than using the 0-initial. The improvement in the accuracy by the P-initial and S-initial lies mainly in longitudinal motion component in terms of magnitude. Since the P-initial was created using the circumferential motion of one point, it achieves less accurate estimation of the circumferential motion globally than all the other methods.

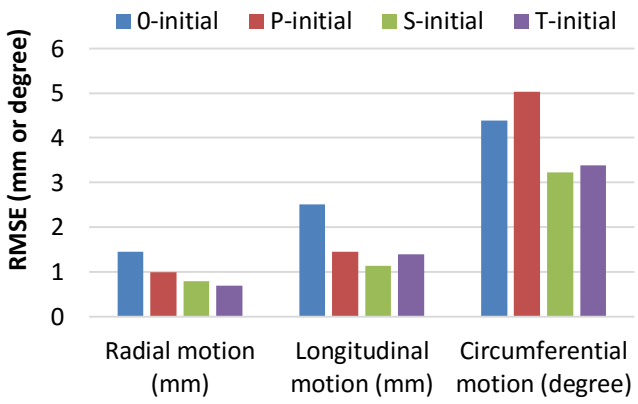

Figure 3-14 The RMSE of three motion components of the MVFs estimated from simulated noisy PET image of frame 1 (ED) using 4 different initial estimates. The RMSE of the radial and longitudinal motion components are in the unit of millimeter, while that of circumferential motion is in degree.

DISCUSSION

In this preliminary study, based on the information provided by the motion of the footprint of a papillary muscle and the interventricular sulcus, a feature guided cardiac MVF approach was developed and tested on the 4-D XCAT phantom heart model with known MVF and simulated MP PET image data generated from the phantom with realistic simulation tools. Four initial estimates including the zero-valued initial, two feature-guided initials, and the true MVF were used in combination with an existing MVF estimation algorithm to estimate the MVF of cardiac images. We have found the feature-guided initials provide significant improvement in the accuracy of MVF estimation over zero initialization. In frames of significant cardiac motions, the P-initial improves motion estimation accuracy than the 0-initial. The S-initial achieves even better performance than the P-initial and comparable with the T-initial. Since the S-initial is created with information about the circumferential motion along the long-axis the heart, while the P-initial is based on motion of a single point at the endocardium, the former achieves more accurate estimation of the circumferential motion for the whole myocardium. We conclude the motion information provided by the anatomical features allows improved MVF estimation of the left ventricular motion from simulated MP PET images. In this study, the proposed method was tested on simulated MP PET images that were generated from the 4-D XCAT phantom, but this method is equally applicable to other imaging modalities such as CT, as long as the papillary muscle can be robustly and accurately extracted from the images. Although the imaging system we simulated in this study is still under development, the success of application our method on simulated data and the clinical patient data indicates it is feasible and promising.

While we have shown improvement in motion estimation accuracy obtained by the utilization of the features, we also realize that this improvement is highly dependent on accurate extraction of the anatomical feature. Noise, resolution, and any other factors that can reduce the image quality will make it more difficult to extract the features accurately. In low-resolution images, the apparent attachment between the papillary muscles and the endocardium may increase, especially during the systolic phase. The connection between the left ventricle and the right ventricle will also become less resolvable. The proposed method requires the image resolution to be high enough to expose the target feature. In simulation data for which the method shows improvement in motion estimation accuracy, the projection data from the high-resolution phantom image was generated with customized high-resolution detector. Currently, the state-of-art PET scanner has spatial resolution of about 4mm, so it is not guaranteed the feature extraction will work on clinical data. With development of

new hardware and improvement in image reconstruction techniques, the resolution the PET imaging system has seen improvement in recent years, providing good prospect for our methods. We should expect more valuable application of our methods with improved PET imaging techniques.

Besides system resolution, the noise level also has significant influence on the performance of our methods. Noise in the image makes it more difficult to extract the features and reduces the reliability of feature tracking results. Extra smoothing filter is necessary to reduce the image noise, but at the expense of reducing resolution. This phenomenon will increase the difficulty of feature extraction. Since the motion estimation result can be significantly influenced by the initial estimation, a P-initial or S-initial based on inaccurate tracking of the papillary muscle or sulcus may lead to increased error in the MVF estimation. Similarly, using an inaccurate motion of the feature as prior information will lead to mistakes in motion estimation results. Images with higher noise level also see more error in the motion estimation results, since noise changes the intensity, which the algorithm is trying to register.

The proposed method does not completely solve the aperture problem of the optical flow based motion estimation algorithm; instead, it suggests the possibility of utilizing anatomical feature and cardiac motion model to guide the motion estimation process for more accurate results. In this study, the proposed method was tested on simulated MP PET images that were generated from the 4-D XCAT phantom, but this method is equally applicable to other imaging modalities such as CT, as long as the papillary muscle can be robustly and accurately extracted from the images.

This study can be extended mainly from two aspects. First, more robust feature extraction methods are required to obtain accurate feature information, especially for noisy cardiac PET data. Second, cardiac motion estimation algorithm may be improved by using the motion of the feature as a prior information.

MOTION ESTIMATION FOR PATIENT DATA

A clinical $^{13}NH_3$ 4D GMP PET study of an abnormal patient was also employed to implement the feature-guided motion estimation method. The patient was injected with standard clinical dose of $^{13}NH_3$ and scanned in GE DVCT PET/CT scanner for 10 minutes. The list-mode data was gated into 8 cardiac gates based on ECG signal and was reconstructed and post-processed onsite. Figure 3-15 shows reconstructed short-axis images at ED and ES. Limited by the resolution of the PET scanner and quality of the image, we

were unable to extract the papillary muscles. Instead, the IS was extracted manually from images at ED and ES, as shown in Figure 3-16. Three motion components were calculated and plot in Figure 3-17. The "twisting" motion of the heart was observed in the middle plot of Figure 3-17, in which the slices above #75 and below #75 rotates in the opposite direction, proving our hypothesis about cardiac motion. Sulcus-based initial MVF was created using the averaged motion of the anterior and posterior sulcus to estimate the cardiac motion from ED to ES.

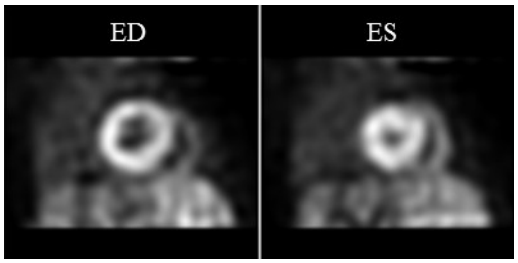

Figure 3-15 Sample PET images from a $^{13}NH_3$ 4D GMP PET study of an abnormal patient at ED (left) and ES (right).

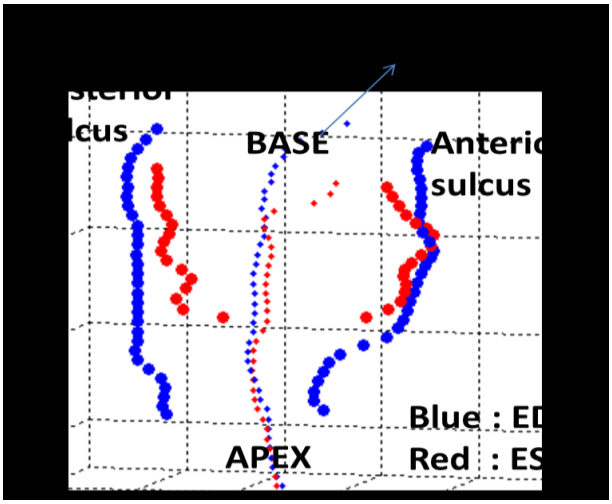

Figure 3-16 Extracted IS from the patient data.

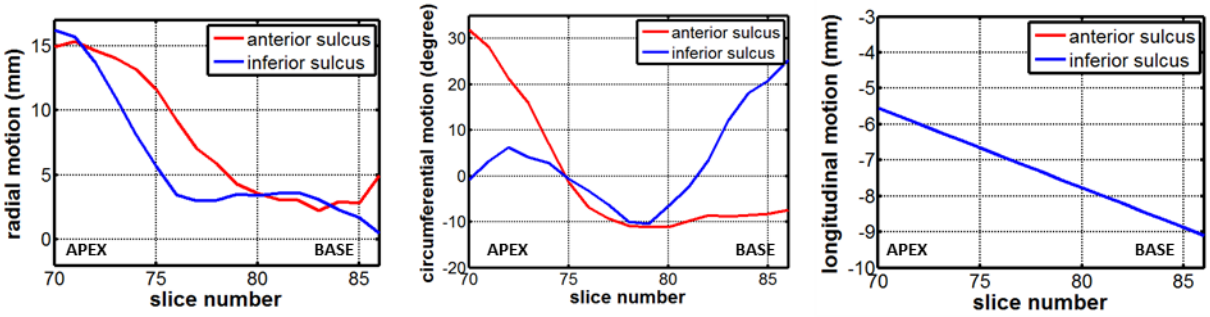

Figure 3-17 Radial (left), Circumferential (middle) and longitudinal (right) motion of the extracted sulcus.

MVF estimated using the sulcus-guided initial and zero valued initial for the patient images was shown in Figure 3-18, in which (a) shows a sample slice at basal region, (b) shows a sample slice at mid-cavity, and (c) a vertical long axis slice. Bull's eye plots of the three motion components from the estimated MVF using S-initial were shown in Figure 3-18. Since motion in the apex is small and can cause large error in circumferential motion, it was omitted in the bull's eye plots. It is noticed that the basal region and mid-cavity region have contradictory circumferential motion. True MVF of the myocardium is not available for this clinical case; therefore, we were not able to evaluate the accuracy of the motion estimation result. However, this case shows the potential of the proposed motion estimation method in clinical study. The motion estimation result is highly dependent on the accuracy of feature extraction, which is determined by both image quality and feature tracking method. With the improvement in PET imaging techniques, the application of the proposed method may become easier and more reliable.

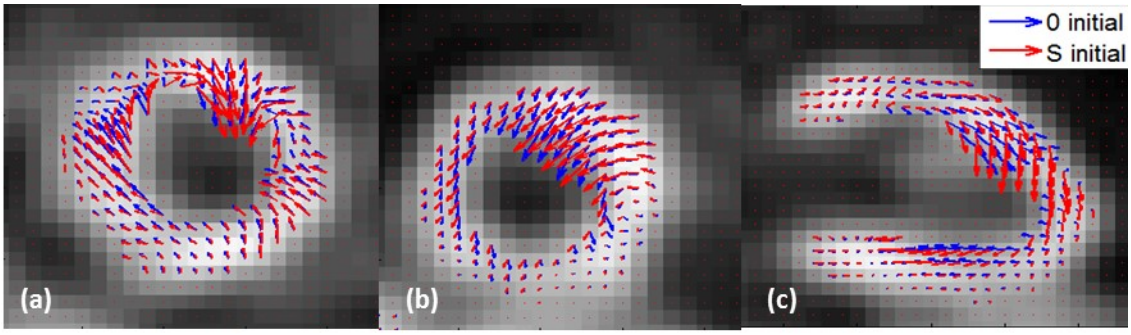

Figure 3-18. MVF estimated from patient data in basal short-axis (a), mid-cavity short-axis (b) and vertical long axis (c) slice.

FURTHER IMPROVEMENT

IMPROVEMNT OF METHODS

A NEW B-SPLINE BASED FEATURE EXTRACTION METHOD

The challenge of extracting IS from cardiac PET images is the blurring of the image due to the low system resolution and image noise. The sulcus extraction method used in preliminary study relies on high-resolution low-noise images. It uses image erosion and image dilation to separate left ventricle and right ventricle. Image erosion and dilation essentially damages the image resolution, and the shape of the separated two parts is no longer the same as the original shape of the left and right ventricle. Furthermore,

although in the simulation data, the right ventricle is assumed to have the same intensity as the left ventricle in the phantom image, its intensity will be reduced in low-resolution images due to partial volume effect. As a result, region growing is not able to accurately segment out both left and right ventricle simultaneously. The extraction of right ventricle will be much more challenging in real clinical cases, the tracer uptake of the right ventricle may not be as high as the left ventricle, which is determined by both the tracer type and the patient.

Instead of identifying the IS directly from the blurred intersection of the LV and RV from the PET images, we developed an extraction method for the IS by the intersection of the estimated boundaries of the LV and LV using B-spline fitting. This method avoids extracting the myocardium and separating the left and right ventricle. The first step of the IS extraction method was to identify and separate the boundary of the LV and the RV from the short-axis slice images of the 3D cardiac PET image at each cardiac-gated frame. An estimate of the inner boundary of the RV was obtained by segmenting the blood pool (BP) within the RV using the 3D region growing method. The shape of the extracted BP was concave at the septal wall side and convex at the lateral side. By subtracting the BP from its convex hull, the septal side of the BP boundary was identified as a segment of the useful outer LV boundary within the RV. We then identified the central segment of the LV boundary outside and on the anterior and posterior sides of the RV from the LV segmented from the original image using 3D region growing. Meanwhile, the segment of the BP boundary on the lateral side of the RV minus the area adjacent to the IS intersection points was identified by subtracting the central segment of the LV boundary from the whole boundary of the BP in the RV. With reduced image resolution, the sulcus point where the left and right ventricle boundary meet is blurred out and becomes less sharp and therefore unreliable. In this situation, the unreliable points near the sulcus point were removed. This process is shown in Figure 3-19.

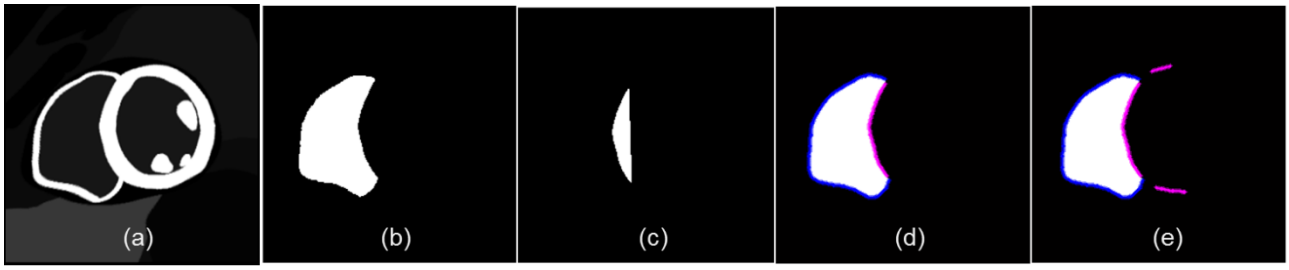

Figure 3-19 Extraction of left and right ventricle boundary. (a) A short-axis slice of the XCAT phantom with activity in myocardium and liver. (b) Blood pool inside the right ventricle segmented using 3D region growing method. (c) Residual shape after subtracting the blood pool from its convex hull, from which the septal boundary is identified. (d) Separated septal boundary and lateral boundary shown in pink and blue respectively. (e) Septal boundary with added points from left ventricle boundary and lateral boundary shown in pink and blue respectively.

The three extracted outer LV segments were fitted with a B-spline curve that passed through the IS intersection points of the short-axis image slice, while the lateral boundary of BP was extrapolated using B-spline curve fitting. The two crossings of the extended BP boundary with the fitted outer LV boundary were determined as the anterior and posterior IS intersection points. The procedures were repeated for all short-axis image slices of the 3D cardiac PET image at each cardiac-gated frame to obtained the anterior and posterior segments of the IS over the entire heart. The process is shown in Figure 3-20.

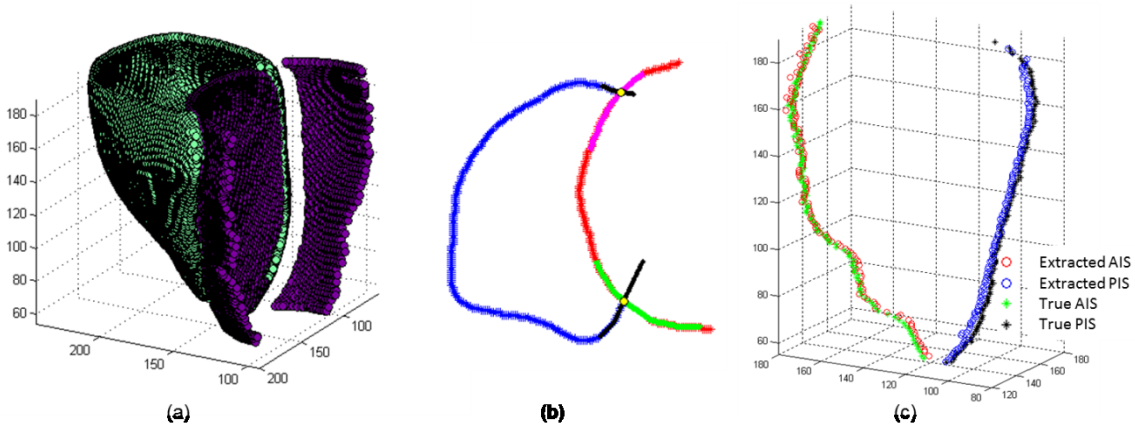

Figure 3-20 (a) 3D display of the extracted two curves from each short-axis slice. Septal boundary and lateral boundary are shown in purple and green respectively. (b) B-spline curve fitting of septal boundary and extrapolation of lateral boundary on one short-axis slice. The intersection is marked by the yellow points. (c) 3D display of extracted IS for all slices, true location of the sulcus is shown for comparison.

MOTION ESTIMATION WITH FEATURE INFORMATION AS CONSTRAINT

The extracted motion of the feature only gives the optical flow algorithm a starting point when used as an initial; in other words, it does not control which direction the optimization of the cost function will go. In order to make full use of the feature information during the motion estimation process instead of only using it as initial, we propose to include the feature into the cost function of the optical flow algorithm. The idea

is to use the motion of the features to guide the motion estimation process. A feature-based constraint is added to the cost function:

$$E_f(\boldsymbol{m}) = g(\boldsymbol{r}; \boldsymbol{r_f}, \sigma)\left\|\boldsymbol{m}(\boldsymbol{r}) - \boldsymbol{m_f}(\boldsymbol{r})\right\|^2.$$

3-14

Hence the cost function becomes

$$E(\boldsymbol{m}) = E_I(\boldsymbol{m}) + \alpha E_S(\boldsymbol{m}) + \beta E_F(\boldsymbol{m}),$$

3-15

where γ is the weight, $g(\boldsymbol{r}; \boldsymbol{r_f}, \sigma)$ is the weight for voxel $\boldsymbol{r}$, and $\left\|\boldsymbol{m}(\boldsymbol{r}) - \boldsymbol{m_f}(\boldsymbol{r})\right\|^2$ is a measurement of the difference between estimated MVF and the prior MVF for the voxel based on extracted MVF of the feature. Here we use l_2 norm as $\|\quad\|^2$ function, which essentially assumes Gaussian noise in the MVF. The weighting factors will be determined empirically. The purpose is to use the motion of the feature to regulate the path of the optimization of the cost function. To simplify calculation and optimization of the cost function, we use all the points of the feature to determine the value $g(\boldsymbol{r}; \boldsymbol{r_f}, \sigma)$ and $\boldsymbol{m_f}(\boldsymbol{r})$ before motion estimation. For the $g(\boldsymbol{r}; \boldsymbol{r_f}, \sigma)$, a mask of the same size as the cardiac image is created by setting value 1 to the sulcus points and value 0 to everywhere else, and then blurred a with a Gaussian filter with standard deviation σ. $\boldsymbol{m_f}(\boldsymbol{r})$ is created using the same method as creating the initial MVF for the myocardium. Thus, each voxel $\boldsymbol{r}$ has a fixed weight factor determined by its distance from the feature, as well as a pre-determined prior MVF based on the extracted motion of the feature.

Similar idea has been proposed by several studies for brain imaging. [96] and [97]use local, nonparametric deformation models with landmark constraints, which need to be first interpolated everywhere to serve as *a pirori* deformation field. The landmarks are determined from an automatic process and are not regarded as definitive. [98] proposed to incorporate the landmark information with a spring term:

$$E_s = \sum_{i=1}^{S} \alpha_i \|\boldsymbol{g}(x_i) - z_i\|^2$$

3-16

Where S is the number of springs, $\alpha_i$are weighting factors, $\boldsymbol{g}()$ is the deformation function, and x_i and z_i are the landmark positions in the reference and test images. Different from the first two studies, [98] imposed the landmark information only at landmark points where it is really known. The landmarks are assumed to come from professional human intervention and therefore are accepted as trustworthy and definitive. These methods are developed for image registration tasks in brain MRI imaging, and have not been applied to cardiac motion estimation area. Moreover, the landmarks used are anatomical structures of human brain such as the sulcal bottom lines or sulci, which are not available for heart which has much fewer distinctive features.

Our method is based on the same ideology that the motion of features or landmarks provides useful *priori* knowledge of the motion of the whole. Different from previous studies mentioned above, this method assign weight to each voxel based on its distance to the feature and the weight is adjustable by changing σ. A large σ means points farther to the feature are also under the influence of the motion of the feature. This allows flexible control of how much the motion of the feature can influence the motion estimation process spatially. More importantly, the cardiac motion model was used in creating the prior MVF, which has never been proposed before. In addition, the weight for the feature-based constraint β is also adjustable. The more reliable the estimation motion of the feature is, the higher the weight should be. Theoretically, assuming the feature based motion estimation of the whole myocardium $\boldsymbol{m_f(r)}$ is the true cardiac motion, the σ value that determines voxel-wise weight and the coefficient β, which is the total weight of feature constraint term, should both be infinitely large, so that the final motion estimation result will be exactly the truth. In this experiment, both values are chosen empirically. We used $\sigma = 15\ pixel$ and $\beta = 8$. Notice that both values are quite large, in order to give large weight to the feature-guided constraint term.

The method was implemented on both phantom images and hybrid cardiac PET data to test its performance in different system resolution and noise level. This will be the first motion estimation method that incorporates anatomical features. Although this method uses anatomical features of the heart and is dedicated to cardiac motion estimation, it may be applicable to estimation motion of other moving organs.

MATERIAL AND EXPERIMENT DESIGN

HYBRID (MONTE-CARLO AND ANALYTICAL) SIMULATION DATA

In preliminary study, we tested the feature-based cardiac motion estimation method with a single set of analytical simulation to prove its feasibility. The next step of our research is to apply the improved methods to more realistically simulated cardiac PET data of different resolution and noise level in order to fully understand its performance in different situations. Besides XCAT and STIR introduced in preliminary study, Monte-Carlo simulation tools SIMSET and GATE were employed in generation of new simulation data.

INTRODUCTION TO MONTE-CARLO SIMULATION TOOLS

The validated integration of the SimSET and GATE in PET simulation with 4D XCAT phantom proves capable of speedup the generation of noise-free data [99].

The SimSET (short for Simulation System for Emission Tomography) package [100] is a Monte-Carlo simulation tool that models the physical processes in emission imaging. The package consists of several modules, each handle a specific physical factor. The core module is the Photon History Generator (PHG) that simulates the radioactive decay and the resulting photon paths through the phantom one by one. The random coincidences generation module simulates random coincidences. It also provides simulation of collimator and detector, but in this study, we only use it to simulate physical processes that happen within the phantom.

GATE is acronym of Geant4 Application for Tomographic Emission [101]. Developed based on Monte-Carlo techniques, it provides modeling of time-dependent processes such as radioactive decay as well as complex system geometry in nuclear medicine. Although it is relatively slow in simulating photon interactions and transmissions in voxelized phantom, its strength in conveniently implementing complex system configurations and simulating collimator/detector responses makes it a useful tool. In this study, we only used it to simulate the physical processes in the PET scanner.

GENERATION OF HYBRID SIMULATION DATA

Although it is desirable to use completely Monte-Carlo simulated data, we found it infeasible and impractical to do so. There are two reasons. First, the high-resolution PET imaging system required for our method is still not available. The resolution of a PET imaging system is limited by the many factors such as

the physical property of the crystals. To achieve the required resolution, we have to cut the crystals in the detector into super small pieces. Moreover, the stopping power of the crystal material has to be much higher than current available materials such as CZT to reduce the depth-of-interaction effects. The Monte-Carlo simulation code we used in this study can only simulate a system that is physically feasible. Second, even if such a system exists and can be modeled by the Monte-Carlo simulation code, it will be extremely time-consuming to run the whole simulation. The highest resolution we tried to achieve in the simulation data is 1mm, much higher than the 6mm resolution of current available system. Six times increase in resolution means that to achieve simulation data of the same noise level will require 6^3 times of the total count, not to mention that it already took 3 months to obtain noise-free data for the 6mm resolution system.

Therefore, instead of spending years generating the Monte-Carlo simulation data, we combined analytical and Monte-Carlo simulation methods to obtain high-resolution simulation data with reasonable computation time and realistic modeling of the imaging physics.

PHANTOM IMAGE

To begin with, the 4D XCAT phantom was digitized into 0.5325mm × 0.5325mm × 0.40875mm voxel sized images. This ultra-fine digitization guaranteed that the features such as papillary muscles and IS were detectable with sufficient accuracy. Activity concentration was set according to the FDG tracer uptake measured from the clinical PET scan of a normal patient. Different from the data set used in preliminary study, the end-systolic (ES) phase was set at 0.5 second with 1 second as cardiac period. The corresponding heart curve is shown in Figure 3-21. Four frames of images were generated at equal time interval over the cardiac cycle, with frame 1 corresponding to ED, i.e., the beginning of the cardiac cycle. We learned from preliminary study that if the cardiac cycle is divided into 8 frames, many frames such as frame #3, #4, #6, #7, and #8 do not contain much cardiac motion for detection. This new setting will make sure the movement of heart between each two consecutive frames is large enough to detect.

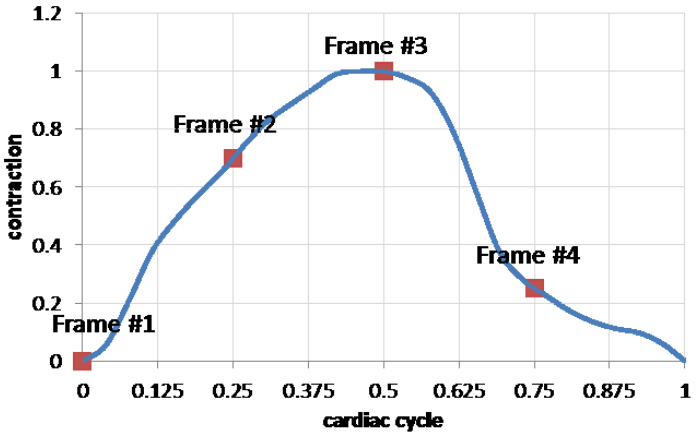

Figure 3-21 Heart curve

GENERATION OF ANALYTICAL SIMULATION PART

The function of analytical simulation part is to generate high-resolution noise-free projection of the primary events. The system we are trying to simulate is not technically available, and cannot be simulated with the current MC simulation tool.

We still use the STIR simulation software to generate noise-free cardiac-gated MP PET projection datasets from the phantom images. The PET scanner simulated here has finer crystal and more rings than the one simulated in preliminary study for higher resolution. The parameters of the customized 3-D PET scanner are provided in Table 3-2. Image degrading factors such as detector response, position range, nonlinearity, and scatter were not included in the simulation of projection, so the system resolution is equal to the bin size.

Table 3-2 Parameters of the customized scanner

Number of rings	188
Number of detectors per ring	2520
Inner ring diameter (cm)	88.62

Average depth of interaction (cm)	0.94
Distance between rings (cm)	0.08175
Default bin size (cm)	0.0599

Under such parameter settings of the simulated scanner, the resulting projection data is a 630×630×188 matrix for each frame of phantom. Attenuation effect was added to the projection data by dividing the projection image with attenuation coefficient sinogram calculated from an attenuation map of the XCAT phantom, which is shown in Figure 3-22.

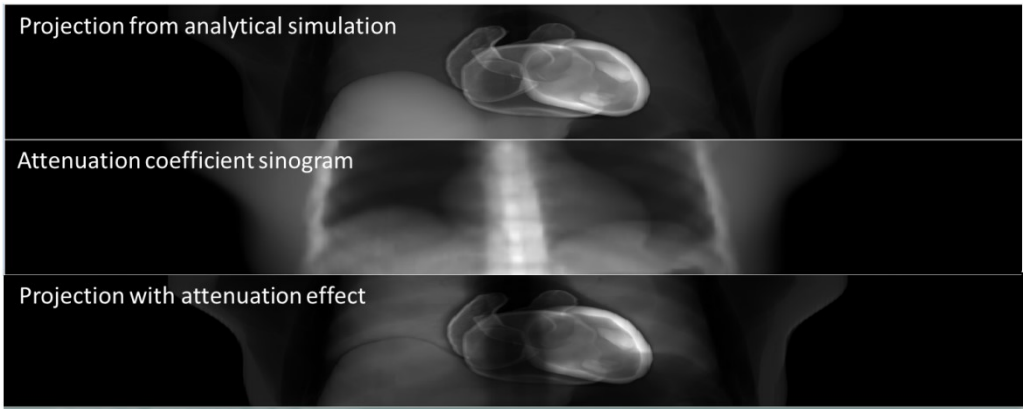

Figure 3-22 Adding attenuation effect to the analytical simulated projection data

GENERATION OF MONTE-CARLO SIMULATION PART

We generated a full-set of noise-free Monte-Carlo simulation data modeling the GE discovery RX scanner by combining GATE and SIMSET software, which was shown to yield faster speed [102102]. The 4D XCAT phantom was digitized into 2.396mm by 2.396mm by 3.27mm voxel sized images for simulation of cardiac PET scan. The GE discovery RX scanner has a system resolution of 6mm and its parameters of are shown in Table 3-3.

Table 3-3 Parameters of the GE discovery RX scanner

Number of rings	24
Number of detectors per ring	620
Inner ring diameter (cm)	88.62

Average depth of interaction (cm)	0.94
Distance between rings (cm)	0.654
Default bin size (cm)	0.2396

Organs including myocardium, blood pool in the heart, spleen, lung, stomach, liver, and the rest of the body were simulated individually. The simulation of separate organs allows creation of any tracer uptake by summing organ projections with different weight, as shown in Figure 3-23. In this study a typical FDG tracer uptake was simulated. The projection data in Figure 3-23 is scaled to isotropic voxel resolution from the original simulation (2.13mm/pixel in horizontal axis and 6.54mm/pixel in vertical axis) for illustration purpose. A combination of 24 equal-time respiratory gates and 48 equal-time cardiac gates with total of 1152 gates were generated. To save simulation time, projections of 1152 dual R&C gates were simulated only for the myocardium and blood pool shown in Figure 3-23. For the rest organs, projections of only 24 respiratory gates were simulated as we assume that the cardiac motion did not affect organs other than the heart. In this case, a total of 2424 (1152*2+24*5) noise free projections were simulated.

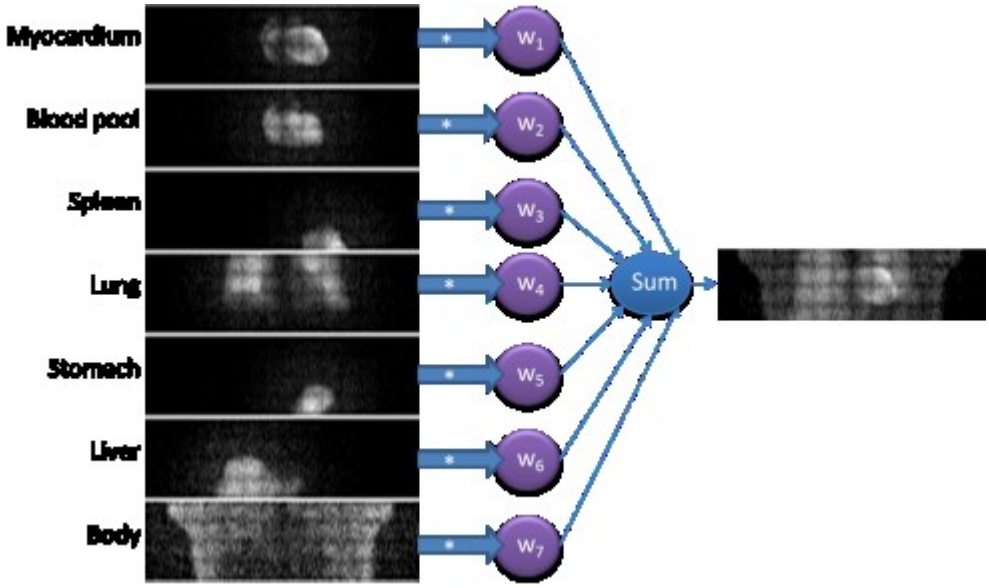

Figure 3-23 Illustration of the simulation for FDG tracer uptake from individual organ uptakes.

Notice that there are dark strips in Figure 3-23. They were caused by non-uniformity in the detectors and detector gaps based on realistic configuration of the GE RX PET scanner. To correct for non-uniformity,

we also generated a noise-free simulation for a uniform cylindrical phantom to obtain a detector coefficient map (

Figure 3-24a).The uniformity map (

Figure 3-24b) was then calculated by dividing the theoretically calculated sinogram of the cylindrical phantom considering only attenuation effect with the Monte-Carlo simulated sinogram of the cylindrical phantom. In the end, Monte-Carlo simulated sinogram from the cardiac PET scan was multiplied by the uniformity map to get uniformity corrected sinogram.

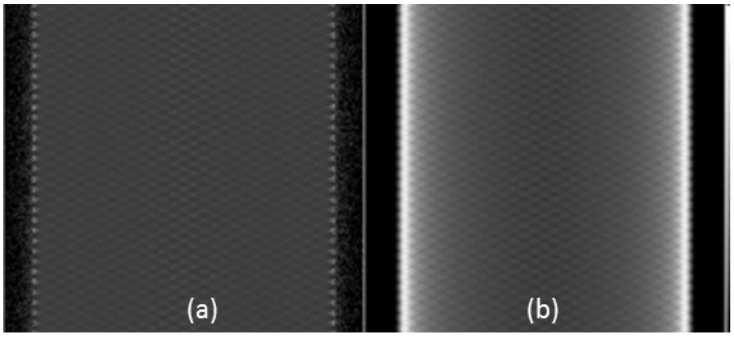

Figure 3-24 Effects of detector non-uniformity and uniformity correction. a) Monte-Carlo simulated sinogram of the digital cylinder phantom, b) uniformity map.

The Monte-Carlo simulation code generates sinogram from primary events and sinogram from scattered events separately. The total number of events and number of scattered events were measured separately from the summed sinogram of all organs and all gates. The scatter-to-all ratio was 34.4334%, which would be used when adding scatter to the analytical simulated sinogram of primary events.

The simulated sinogram of scattered events cannot be used directly in generating hybrid simulation data. There are two problems to solve before simply adding it to the analytically simulated primary events. First, even though the summed sinogram of primary events for all organs and all gates is almost noise-free, the sinogram of the scattered events is not since scatter is only 34.4334% of the total events. Sinogram of scattered events for single cardiac frame is even noisier since each gate only contains a small portion of the total count. We do not want to introduce noise to the projection data through adding scatter. Second, the imaging system used in analytical simulation has much higher resolution than the GE scanner simulated in Monte-Carlo code. Even the dimension of projection data is different.

To solve these two problems, we used three combined approaches. First is to use scattered events from all simulated gates to approximate scattered events in each single cardiac gate. Thus, the summed projection of scattered events will have much lower noise. Second is to use B-spline interpolation to obtain a "noise-free" sinogram of the scattered events from the high-count yet still not noise-free simulated scatter sinogram. Figure 3-25 shows the effect of this approach. Third is to use B-spline interpolation to generate sinogram under high-resolution system setting from "noise-free" sinogram from low-resolution simulation. All three approaches are based on the knowledge that scatter is a slow spatially varying component. The influence of resolution is negligible considering that scatter effects have wide spatial spread. Figure 3-26 shows the comparison between scatter projection before and after all three steps.

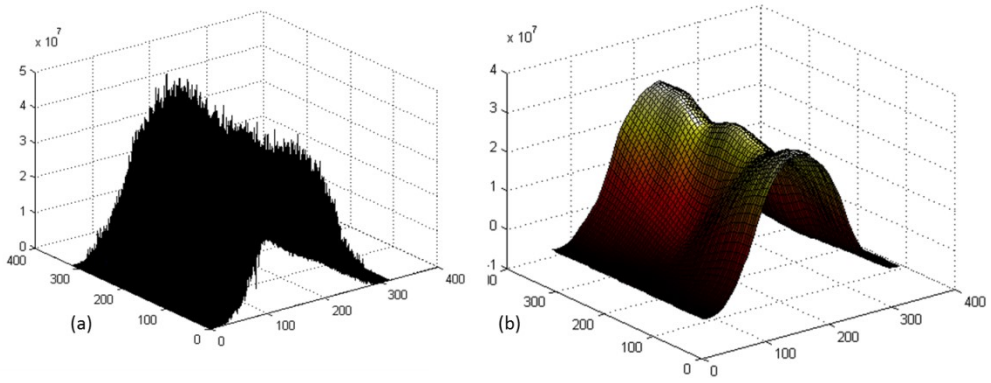

Figure 3-25 Interpolation from noisy scatter to noise-free scatter. (a) One sinogram of summed projection of scattered events from all gates MC simulated gates. (b) noise-free sinogram of scatter after B-spline surface fitting.

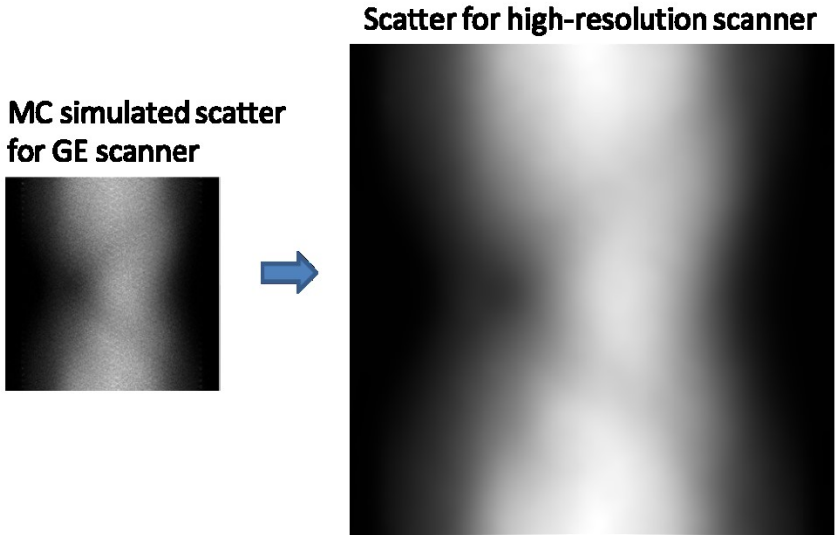

Figure 3-26 Scatter projection from MC simulation and resulting scatter projection for high-resolution scanner

COMBINATION OF ANALYTICAL AND MONTE-CARLO SIMULATION

The projection of scattered events interpolated from MC simulation data was added to the projection of primary events from analytical simulation after being scaled according to the scatter-to-primary ratio measured from MC simulation. Thus, we obtained high-resolution noise-free projection data with attenuation and scatter effect.

There are two factors we want to include in the simulation data: resolution and noise. We tested five resolution levels: 0.6mm, 1.5 mm, 3mm, and 4.5mm. The first one is the highest resolution achieved by the analytical simulation setting. Both 0.6mm and 1.5mm resolution systems are still not available, while 3mm is recently achieved by the most advanced PET system developed by United Imaging. 4.5mm the system resolution of the Philips Vereos Digital PET/CT scanner. To obtain data with the last three resolution levels, corresponding Gaussian filter was applied to the 0.599mm resolution projection data. We simulated four different noise levels: noise-free, 8 times, 2 times and 0.5 times of "clinical counts"; they are named as NF, 8N, 2N and 0.5N, respectively. The photon counts in the central slice of the projection data for a routine clinical cardiac PET scan is 6000, and this is based on a patient data acquired on a GE discovery RX scanner. The slice thickness for the patient data is 3.27mm, which is eight times of the slice thickness for the high-resolution simulation data. The detector bin size of the GE system is 4 times of the simulated high-resolution scanner according to Table 3-2 and Table 3-3. To achieve the same noise level for each pixel in projection data, the "clinical counts" mentioned above for the simulated PET data was in fact 128 times of the real clinical counts. The noise was added to the projection data by first scaling the data to corresponding total count, then adding Poisson noise.

In the end, the projection data was reconstructed using OS-EM algorithm by the STIR software. We used 21 subsets and 3 iterations to obtain the final reconstructed images. The attenuation map was used as another input in addition to the projection data, assuming perfect attenuation correction. Scatter was not corrected in this study to add extra difficulty to the feature extraction task. The reconstructed images are in pixel size 0.6mm by 0.6mm by 0.6mm, and are reoriented into short-axis view for feature extraction and motion estimation. The image matrix size is 256 by 256 by 256. After feature extraction, the images were

collapsed by 2 in three directions and the matrix size became 128 by 128 by 128 for motion estimation. Figure 3-27 shows noise-free reconstructed images in short-axis view for frame #1 with different system resolution. The proposed methods were applied to the reconstructed cardiac images, and the results were shown in the next section.

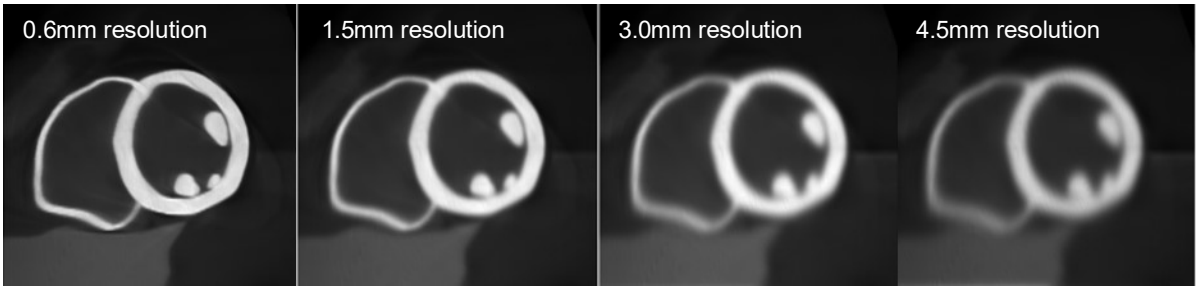

Figure 3-27 Reconstructed images from the noise-free hybrid simulation data of frame #1 for different resolution

RESULTS

INVESTIGATION ON PAPILLARY MUSCLE EXTRACTION

In preliminary study, we have found that the change in the location of the centroid of the papillary muscle footprint is inconsistent with its true motion. Using the new data set, we carefully investigated this phenomenon and demonstrated why the papillary muscle may not be a reliable feature to use in cardiac motion estimation.

The true centroid location of the papillary muscle footprint was determined from the phantom images of four cardiac frames. Since we have reoriented the cardiac images into short-axis view, the *z* axis is the longitudinal direction. The true longitudinal movement of the centroid was calculated from the true MVF of the XCAT phantom. The results are shown in **Error! Not a valid bookmark self-reference.**.

Table 3-4 Footprint centroid extraction results from phantom images of four cardiac frames

	x	y	z	area of footprint (pixels)	true Vl (pixel)
frame 1	70.9076	156.1261	113.1176	119	-6.7
frame 2	85.0635	155.5159	109.1905	126	-3
frame 3	91.354	156.354	109.8137	161	7.7

frame 4	75.8448	155.6207	111.7155	116	2.4

The footprint centroid in frame 1 should move to z=106.4176 according to the true MVF. In addition, from frame 2 to frame 3, the centroid is supposed to move towards lower z value, but does not do so in the extraction result. From the table, it is clear that the inconsistency is inherent for the XCAT phantom. This does not mean that the phantom is wrong. On the contrary, this indicates the phantom models the morphology of human heart realistically. Physiologically, the area where the papillary muscle and the endocardium contact is changing during the cardiac cycle. Note that "contact" is not equivalent to "attach". By "contact", we mean the papillary muscle appears to be touching the endocardium, but the connection is only visual and not physiological. The contacting region is extract from the cardiac images as the footprint. By "attach", we mean the region where papillary muscle and the endocardium are inseparably connected, and its area does not change during the cardiac cycle. The real attachment is contained in the contacting region. The shape and location of the papillary muscle footprint changes as the muscle contracts or relaxes to control the mitral valve. At diastolic phase, the mitral valve opens and the papillary muscle relaxes, the contacting region between papillary muscle and the endocardium is close to the true attaching region. At systolic phase when the papillary muscle contracts, not only its shape gets shorter and thicker, but it also moves towards the apex and presses more into the endocardium. As a result, the contacting region, i.e. the footprint, includes not only the true attaching region but also more apparent connection. This can be observed by the area of footprint in four cardiac frames in The results are shown in **Error! Not a valid bookmark self-reference.**.

. The centroid of the increased contacting area is no longer the true centroid of the papillary muscle root.

We also used the feature extraction method proposed in preliminary study to extract the centroid location from simulated noise-free cardiac PET images of 0.6mm, 1.5mm, 3.0mm system resolution. The x, y, z coordinates of the footprint centroid, as well as the area of the footprint measured in number of pixels, are shown in Table 3-5.

Table 3-5 Footprint centroid extraction results for three system resolutions

	0.6 mm resolution				1.5mm resolution				3.0mm resolution			
	x	y	z	Area	x	y	z	Area	x	y	z	Area
frame 1	69.9	154.7	115.3	142	68.4	154.7	122.3	220	67.8	153.9	128.2	375
frame 2	84.6	155.2	112.1	166	83.4	155.5	119.4	304	83.1	155.0	124.1	467
frame 3	90.5	156.1	115.6	273	90.3	155.9	119.3	410	90.2	156.0	122.0	565
frame 4	75.4	154.8	112.8	140	74.1	155.5	120.3	221	73.1	154.2	126.7	392

As the resolution degrades, the gap between the papillary muscle and the myocardial wall is further blurred, making it more and more difficult to determine the accurate location of the footprint. The extracted centroid location shifts towards the basal direction (larger z value) and the footprint size increases dramatically, especially for the end-systolic phase (frame 3). The poorer the resolution gets, the more prominent this effect is.

In summary, both the physiological property of the papillary muscle and the blurring by system resolution make the papillary muscle unreliable in terms of indicating accurate cardiac motion. For the rest part of the research, we only used the IS as reliable cardiac feature for motion estimation.

RESULTS ON IMPROVED FEATURE EXTRACTION METHOD FOR IS

The improved IS extraction method was implemented and applied to hybrid simulation data, and the results were compared with the IS extraction method proposed in preliminary study. For quantitative evaluation, we defined the error of estimated sulcus location as:

$$\boldsymbol{E} = \frac{\mathbf{1}}{\boldsymbol{N}}\sum_{\boldsymbol{i=1}}^{\boldsymbol{N}}\|\boldsymbol{L_{est}}(\boldsymbol{i}) - \boldsymbol{L_{tr}}(\boldsymbol{i})\|_{\mathbf{2}} \,. \tag{3-17}$$

where i is the short-axis slice number, N is the total number of short-axis slices along the IS, $\boldsymbol{L}_{est}(i)$ and $\boldsymbol{L}_{tr}(i)$ are the estimated 2D location of sulcus point and the true location of sulcus point on short-axis slice i, respectively; $\|\quad\|_2$ is the l_2 norm. The true location of the sulcus points was obtained from the XCAT phantom image by both methods for consistency. In other words, for each IS extraction method, when

calculating the error in the location of the extracted IS from simulated cardiac PET images, the extracted IS location from phantom image obtained with this specific method was used as the truth.

The IS extraction error in noise-free simulation data of different system resolution using the improved method and the previous method is shown in Table 3-6. The errors for AIS and PIS were calculated separately. As expected, the IS extraction error increases as the system resolution degrades with both methods. Under the four simulated system resolution, the improved method generally has higher accuracy than the previous method. Especially, for the 4.5mm resolution cardiac images, the previous method was unable to extract the sulcus location. Another distinctive phenomenon is that the accuracy of PIS is almost always higher than that of AIS under four system resolutions and in four cardiac frames, and the degradation of its accuracy under poor resolution is much less severe than that of the AIS. This is due to the difference in the shape of the two corners of the bloodpool in the right ventricle. The anterior corner is an acute angle, making it easier to be blurred out under poor system resolution. The posterior corner is an obtuse angle, less susceptible to resolution degradation.

Table 3-6 IS extraction error (mm) using the improved method and the previous method under four system resolutions

	interpolation method		previous method	
	0.6mm resolution simulation noise free			
	AIS	PIS	AIS	PIS
Frame 1	1.04	0.85	0.91	0.91
Frame 2	1.06	0.49	1.28	1.59
Frame 3	1.13	0.49	0.86	0.70
Frame 4	1.02	0.49	0.84	0.63
	1.5 mm resolution simulation noise free			
	AIS	PIS	AIS	PIS
Frame 1	1.52	0.83	1.60	1.64
Frame 2	1.78	0.66	1.49	1.02

Frame 3	1.81	0.72	1.54	1.66
Frame 4	1.80	0.69	1.66	1.53
	3 mm resolution simulation noise free			
	AIS	PIS	AIS	PIS
Frame 1	2.39	1.01	4.69	2.55
Frame 2	2.90	0.96	2.45	1.97
Frame 3	3.13	1.12	2.61	3.18
Frame 4	2.54	0.85	3.77	2.65
	4.5 mm resolution simulation noise free			
	AIS	PIS	AIS	PIS
Frame 1	3.53	1.02	fail	fail
Frame 2	4.27	1.39	fail	fail
Frame 3	4.30	1.64	fail	fail
Frame 4	3.70	1.10	fail	fail

It is important to accurately extract the sulcus location in all cardiac frames since the error in IS extraction will be propagated to the calculated sulcus motion. In cardiac motion estimation, the motion of the PIS was used to create S-initial and S-guided constrain, as the PIS extraction was more accurate than AIS.

MOTION ANALYSIS OF PIS

The motion of the sulcus between each two frames was calculated from the estimated location of the sulcus based on the linear assumption of the longitudinal motion, using the method in preliminary study. The two basal end-points of the sulcus in each two frames were matched, and then other points were matched proportionally. Three motion components were calculated based on the point-to-point correspondence and the shape of the heart.

The following figures show the three motion components from frame 1 to frame 2 of the PIS calculated from phantom images. On the curves, each data point represents an extracted sulcus point. The long-axis

slice number from small value to large value represents sulcus point location along cardiac long-axis from apex to base. Notice that the circumferential motion is measured in degree, while the radial and longitudinal motion are measured in pixel. Here we show the radial and longitudinal motion in pixels instead of mile-meter, because feature extraction is carried out in pixelated cardiac images with 0.6mm pixel size.

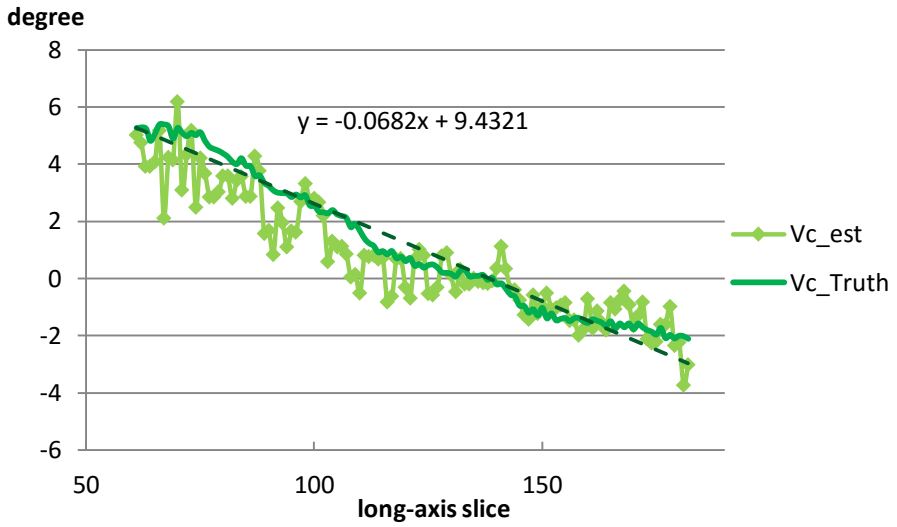

Figure 3-28 Circumferential motion of PIS from frame 1 to frame 2 calculated from phantom images. The true circumferential motion is shown in darker green as reference.

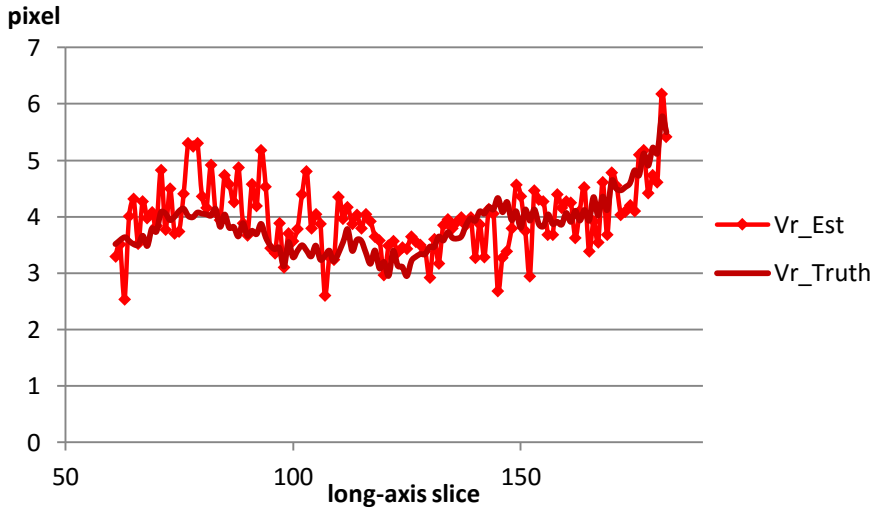

Figure 3-29 Radial motion of PIS from frame 1 to frame 2 calculated from phantom images. The true radial motion is shown in darker red as reference.

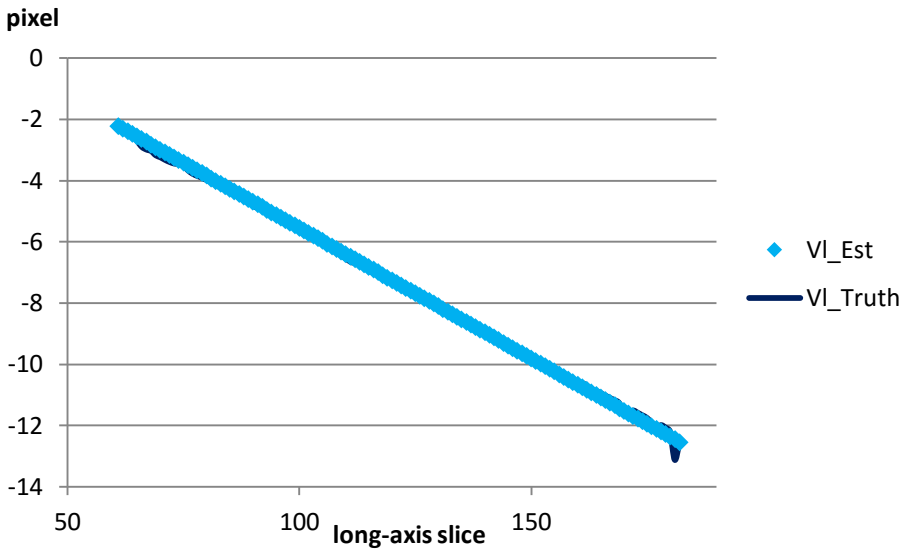

Figure 3-30 Longitudinal motion of PIS from frame 1 to frame 2 calculated from phantom images. The true longitudinalmotion is shown in darker blue as reference.

As Figure 3-28, Figure 3-29and Figure 3-30 show, the three motion components of the PIS calculated from the phantom images are reasonably accurate. Especially, the longitudinal motion from estimation matches very well with the truth. This is essential as the calculation of the other two components relies on finding the corresponding long-axis slice for the sulcus point in the second frame. The phantom images provide sharp boundaries of the myocardium, but even with this unrealistically high image quality, there is still error in radial and circumferential motion. The error in radial motion is within 2 pixels, which is reasonable as feature extraction is pixel-based.

Although the motion of PIS extracted from phantom images is reasonably accurate, it is not the case in simulated cardiac PET images, especially when the system resolution gets worse. The following figures show the radial and circumferential motion of PIS from frame 1 to frame 2 extracted from noise-free simulation images of different system resolution. As the longitudinal motion is always determined based on visual observation of the basal end of the sulcus, it is always the same as the result from phantom images. From Figure 3-31 to Figure 3-34, the radial motion is overestimated for images of all resolution levels, and the overestimation increases from high-resolution to low-resolution except for 4.5mm system resolution. Meanwhile, the radial motion curve becomes less smooth as the resolution degrades. For circumferential motion, there is also a visible trend from high resolution to low resolution. In Figure 3-31, when the system

resolution is very high and same as the pixel size of the phantom image, the circumferential motion is close to the truth. However, as system resolution becomes lower, the slope of the circumferential motion decreases. At 4.5 mm resolution, the linear regression line of circumferential motion is almost flat. In other words, the "twisting" of the heart becomes less and less distinguishable as the resolution degrades. Besides the changes in motion estimation accuracy, the curves for the PIS motion also become shorter at the apical end from results of 0.6mm resolution to that of 4.5mm resolution. It gets more difficult to extract the sulcus points near the apex with lower resolution, because the right ventricle is much smaller at the apical region and hence is more susceptible to the blurring of lower system resolution.

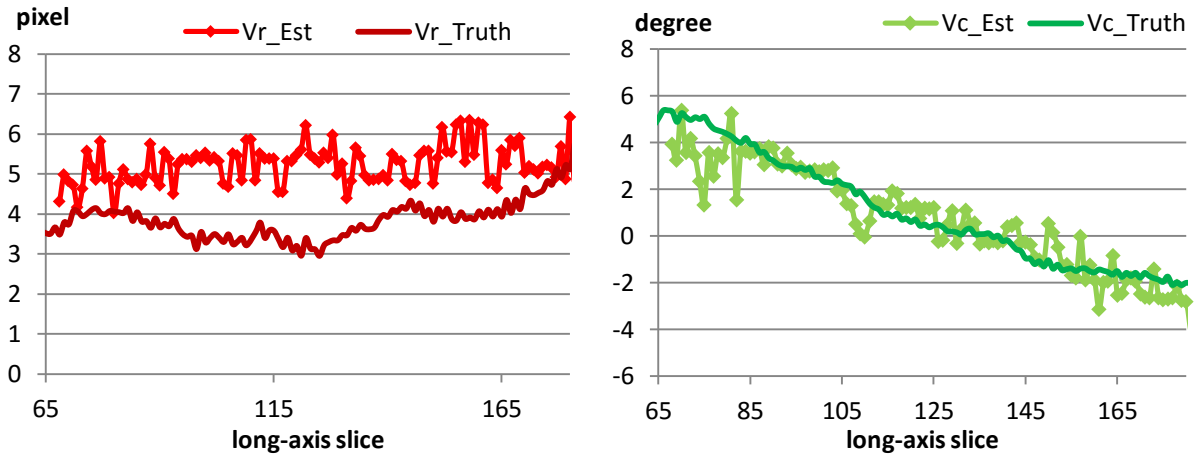

Figure 3-31 Radial (left) and circumferential (right) motion of PIS from frame 1 to 2 extracted from noise-free simulation data of 0.6mm system resolution. The true radial and circumferential motion are shown by darker red and darker green curves respectively.

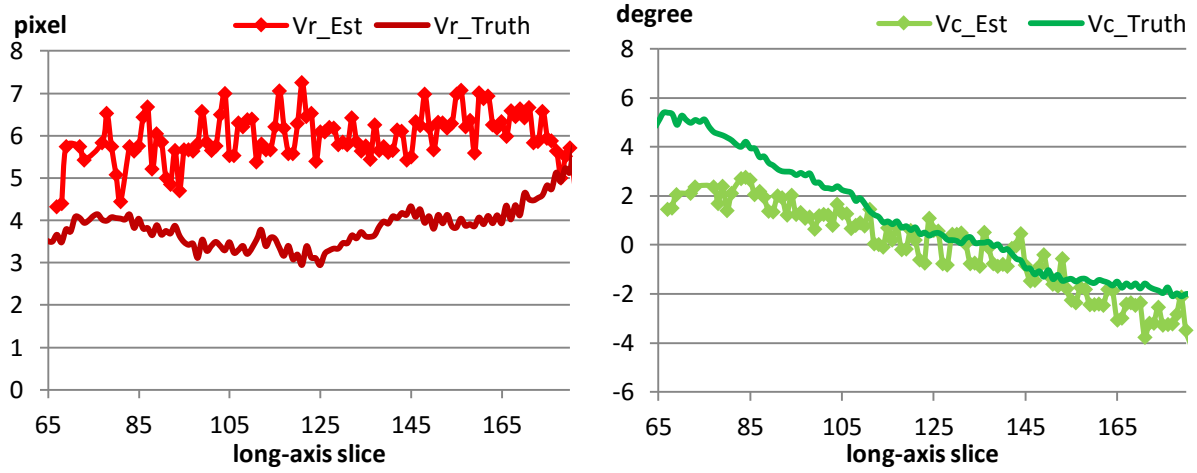

Figure 3-32 Radial (left) and circumferential (right) motion of PIS from frame 1 to 2 extracted from noise-free simulation data of 1.5 mm system resolution. The true radial and circumferential motion are shown by darker red and darker green curves respectively.

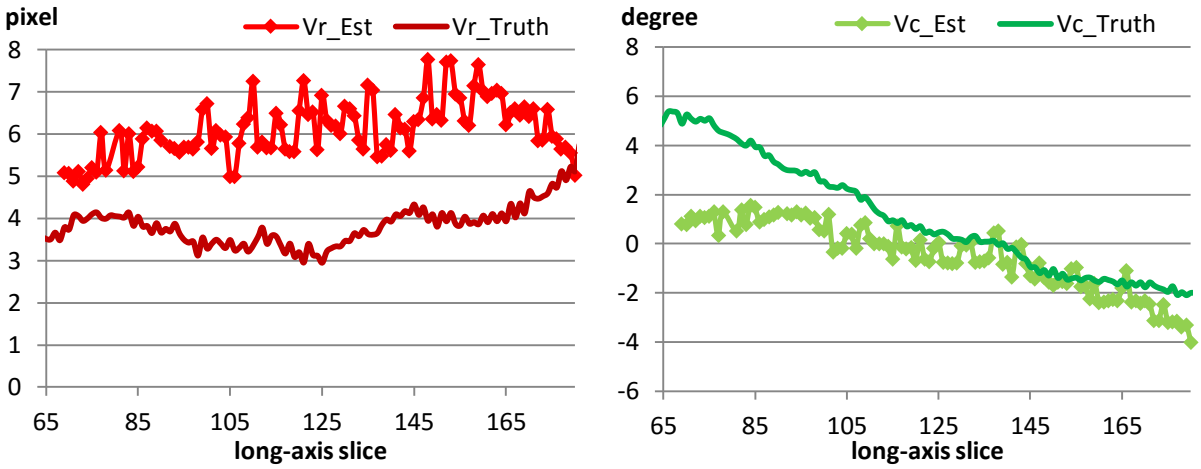

Figure 3-33 Radial (left) and circumferential (right) motion of PIS from frame 1 to 2 extracted from noise-free simulation data of 3.0 mm system resolution. The true radial and circumferential motion are shown by darker red and darker green curves respectively.

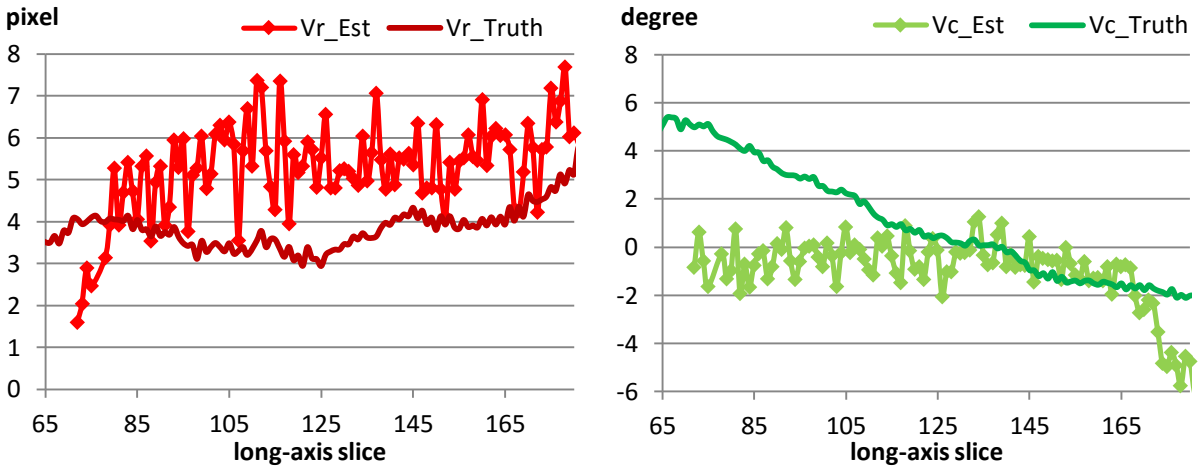

Figure 3-34 Radial (left) and circumferential (right) motion of PIS from frame 1 to 2 extracted from noise-free simulation data of 4.5 mm system resolution. The true radial and circumferential motion are shown by darker red and darker green curves respectively.

Besides image resolution, noise level is also an important factor that influences the extracted motion of the feature. The following figures show the radial and circumferential motion of PIS from frame 1 to frame 2 extracted from simulated cardiac PET images of 0.6mm system resolution at different noise levels. The overestimation of radial motion is observed from results of all four noise levels, but it does not increase

from low noise to high noise except that it is higher at noise-level 8N. However, with increased noise, the radial motion curve becomes less smooth, similar to the observation when the system resolution degrades, especially for 4.5mm system resolution. Accuracy of the circumferential motion decreases with higher noise, and linear regression line becomes more flat when the noise is increased. The similarity in the influence of resolution and noise level is reasonable, as the increasing noise requires smoothing filter during feature extraction, which essentially degrades the image resolution.

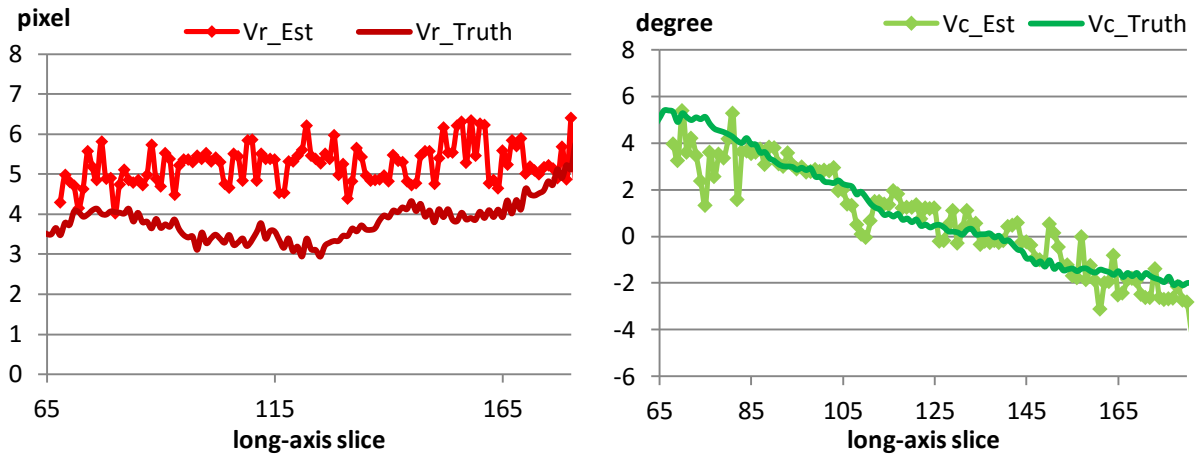

Figure 3-35 Radial (left) and circumferential (right) motion of PIS from frame 1 to 2 extracted from noise-free simulation data of 0.6mm system resolution. The true radial and circumferential motion are shown by darker red and darker green curves respectively. This figure is the same as Figure 3-31, and it is shown again for comparison with results from other noise-levels.

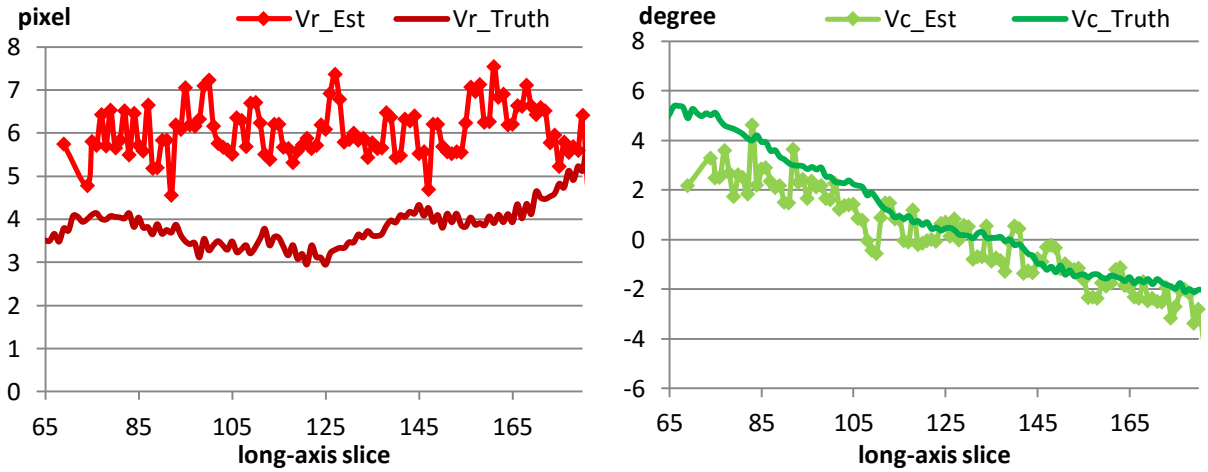

Figure 3-36 Radial (left) and circumferential (right) motion of PIS from frame 1 to 2 extracted from simulation data of 0.6mm system resolution at noise-level 8N .The true radial and circumferential motion are shown by darker red and darker green curves respectively.

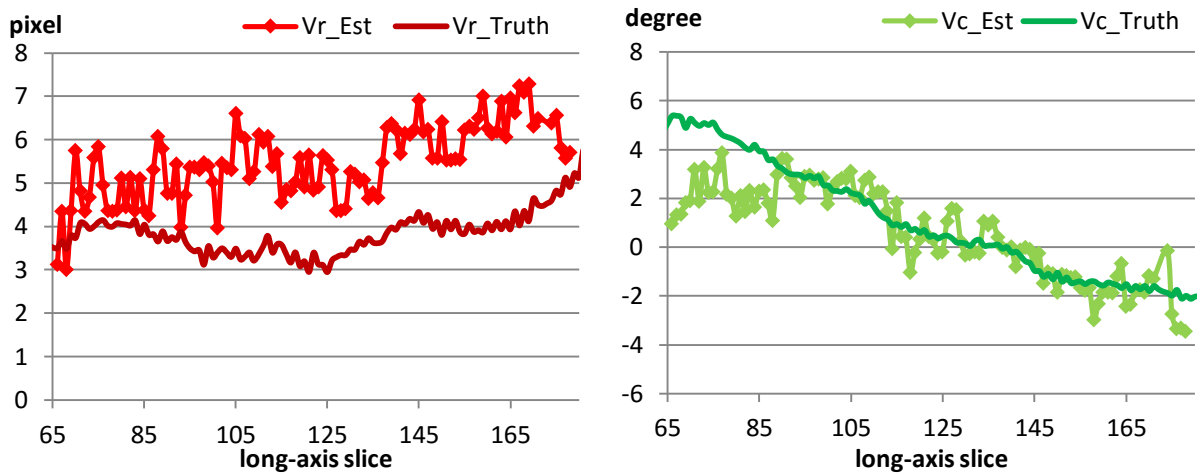

Figure 3-37 Radial (left) and circumferential (right) motion of PIS from frame 1 to 2 extracted from simulation data of 0.6mm system resolution at noise-level 2N.The true radial and circumferential motion are shown by darker red and darker green curves respectively.

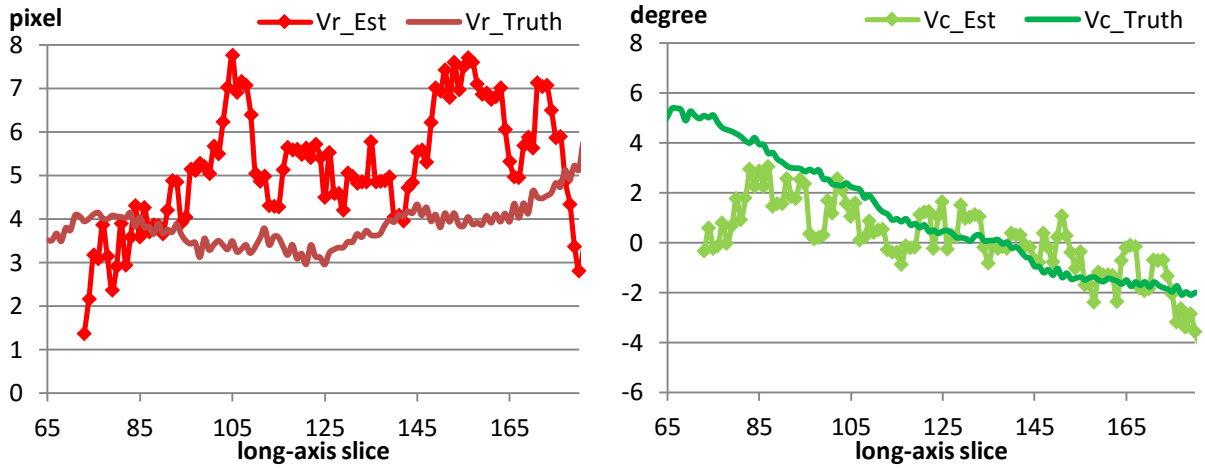

Figure 3-38 Radial (left) and circumferential (right) motion of PIS from frame 1 to 2 extracted from simulation data of 0.6mm system resolution at noise-level 0.5N.The true radial and circumferential motion are shown by darker red and darker green curves respectively.

RESULTS ON FEATURE-BASED CARDIAC MOTION ESTIMATION

Before analyzing the cardiac motion estimation results, we first studied the true cardiac motion provided by the XCAT phantom. The motion of the myocardium between neighboring frames of the four cardiac frames describes the change in the shape of a normal human heart. The heart starts to contract from the first frame and reaches end-systolic phase at frame 3, and then starts to relax back to frame 1. The average magnitude of the cardiac MVF in 4 frames of phantom images is provided in Figure 3-39, in which we can find that

frame 1and 3 have relatively larger cardiac motion than the other two frames. Among the 4-frame cardiac images, frame 1 has the largest contracting motion during the systolic phase while frame 3 has the largest relaxing motion during the diastolic phase.

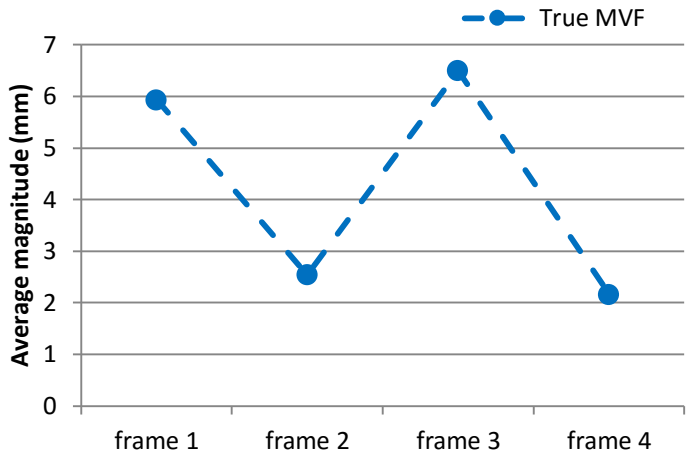

Figure 3-39 Average magnitude of the true MVF in four frames of phantom images.

Cardiac motion between each two neighboring frames was estimated using four methods: (1) 0-initial with conventional optical flow, (2) S-initial with conventional optical flow, (3) T-initial with conventional optical flow, and (4) S-initial with sulcus motion as additional constraint, named as S-constrain + S-initial.

RESULTS FOR PHANTOM IMAGES

The global cardiac motion estimation error defined by RMSE was calculated using 3-13 for the four methods and was shown in Figure 3-40. For phantom images, the S-initial achieves more accurate motion estimation result than 0-initial for all cardiac frames. The T-initial is always the best among the four methods. With the new feature-based optical flow approach, i.e. the S-constraint + S-initial, the motion estimation error is further reduced and is comparable with the result of T-initial. Even in frames with small cardiac motion, the information of IS is able to improve motion estimation accuracy. In frames with large motion, the improvement by S-initial and feature-based method is more distinctive than in frames with small motion.

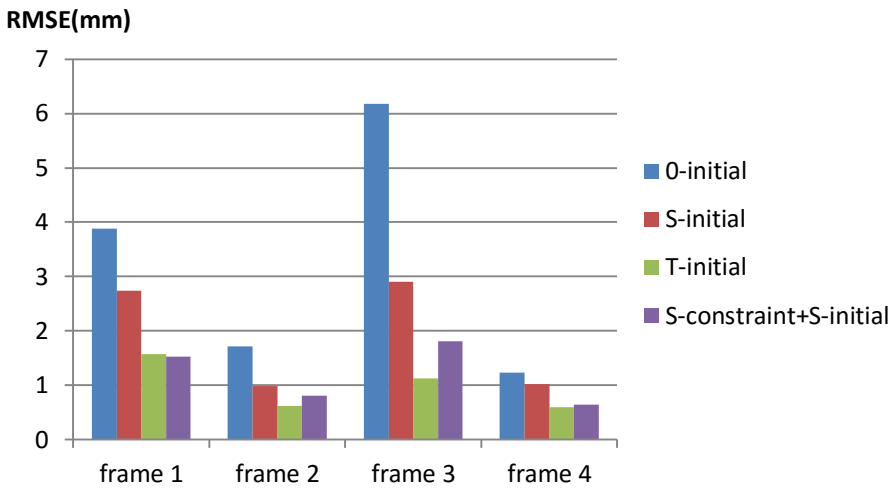

Figure 3-40 Motion estimation error RMSE for phantom images using four different methods.

To understand how well the four methods estimate three cardiac motion components, we calculated the motion estimation error for each component separately. The global RMSEs for three motion components as well as the whole MVF are shown in Table 3-7, and the average magnitude of each component and the MVF is shown as reference. The longitudinal motion is the largest among all three components in amplitude. Although the value of average circumferential motion amplitude is similar to longitudinal motion, its contribution to the total MVF is small because it is measured in degree. All four methods have relatively small error in radial motion, as it is perpendicular to the boundary of myocardium. Both circumferential and longitudinal motion are parallel to edges, and therefore difficult to estimate without help from the feature. The error in longitudinal motion is the largest among all three components due to its direction and amplitude. 0-initial has the largest error in all three components while the S-constraint + S-initial and T-initial perform the best. S-initial performs slightly better in circumferential and longitudinal motion estimation, but the improvement is not as large as that when combined with S-constraint. Moreover, the S-constraint + S-initial method yields most accurate estimation of the circumferential motion, which is not available even with true MVF as initial estimate. Even though the feature-guided motion estimation method is slightly worse in radial and longitudinal motion estimation, its improvement in circumferential motion is more significant and the total error is comparable as T-initial.

Table 3-7 Global error RMSE for three cardiac motion components in frame 1

	Average amplitude		0-initial	S-initial	T-initial	S-constraint + S-initial
Vr(mm)	3.33	RMSE_Vr(mm)	0.81	0.63	0.52	0.76
Vc(degree)	3.80	RMSE_Vc(degree)	5.37	4.63	4.41	3.17
Vl(mm)	3.77	RMSE_Vl(mm)	3.35	2.23	0.91	1.02
MVF(mm)	5.94	RMSE_MVF(mm)	3.88	2.74	1.57	1.52

To have a close observation of the cardiac motion estimation results of four methods, we plotted the MVF in frame 1 estimated by the methods for three representative SA slices and one HLA slice. As shown in Figure 3-41, the basal SA slice of the heart is contracting and rotating in the counter-clockwise direction in frame 1. The 0-initial is able to identify the radial motion, but it fails to detect the circumferential motion. The MVFs estimated with S-initial and T-initial are comparable and both are closer to the true MVF. However, in the posterior region, they are still not able to estimate the circumferential motion accurately due to aperture problem. The MVF estimated by the feature-guided method, i.e. S-constrain + S-initial method, matches the true MVF very well generally, even for the posterior region.

In the non-twisting SA slice, which is plane where the circumferential motion is the minimum. As show in Figure 3-42, the difference between the motion estimation results of four methods is negligible. All the four methods provide reliable estimation of the radial motion. At the posterior region near the PIS, the S-constrain + S-initial method performs better than the other three methods, although the difference is small in magnitude. At the anterior region, there are discrepancy between the estimated motion vectors of all the four methods and the truth.

At apical region shown in Figure 3-43, the heart is contracting as well as rotating clockwise in contrary to the basal region. Similar to the result in the basal SA slice, the 0-initial failed to identify the circumferential motion, as it is tangential to the boundary of the myocardium. Even using the true MVF as initial estimate, the result is still not much better, since the strain energy term in the cost function of conventional optical flow algorithm penalizes this motion component. The S-constrain + S-initial method yields the best estimation of the MVF among the four methods, especially for the circumferential motion.

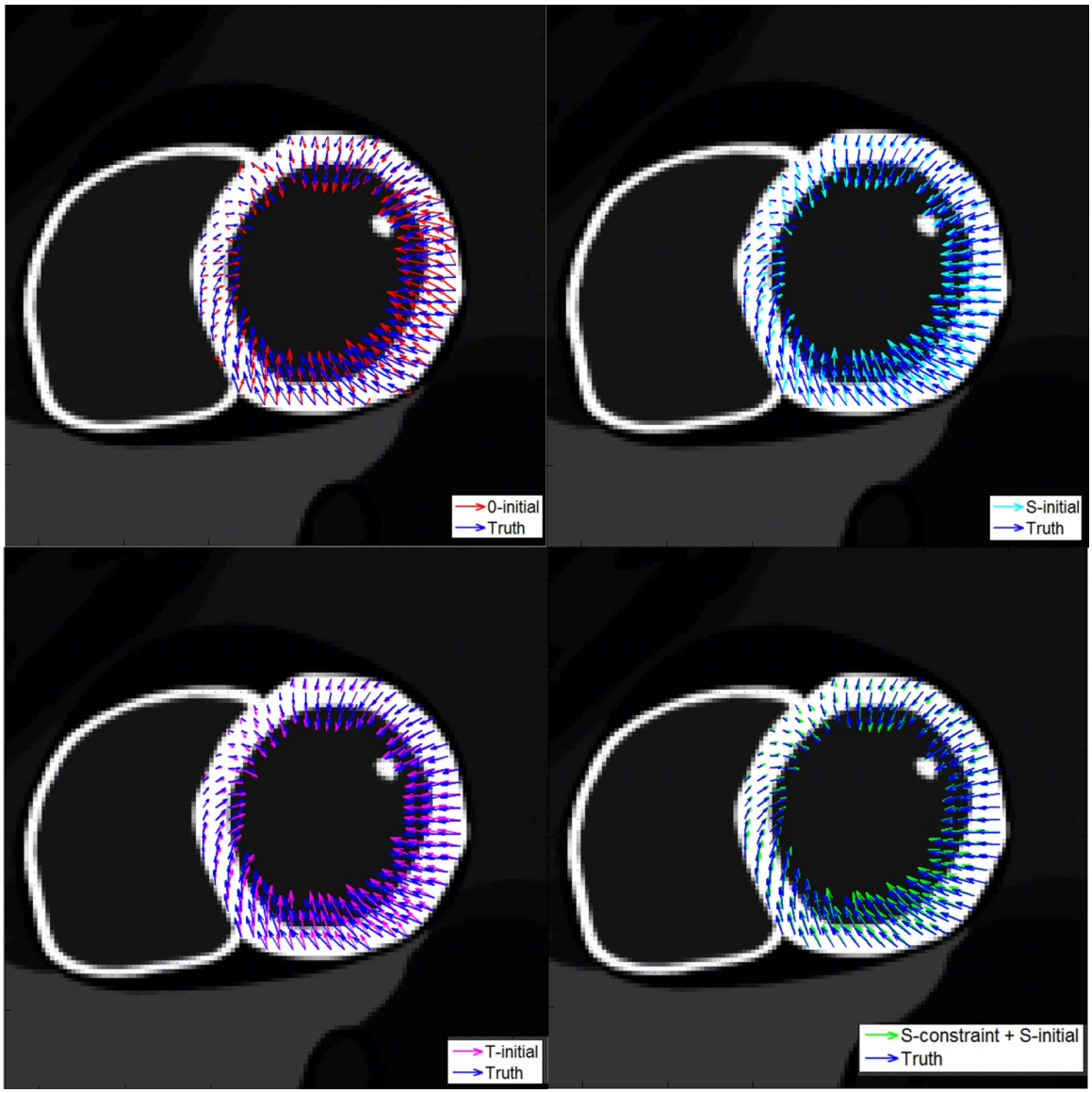

Figure 3-41 Cardiac motion estimation results using four methods for phantom image frame 1 at a basal SA slice. The true MVF is plotted in blue arrows for comparison.

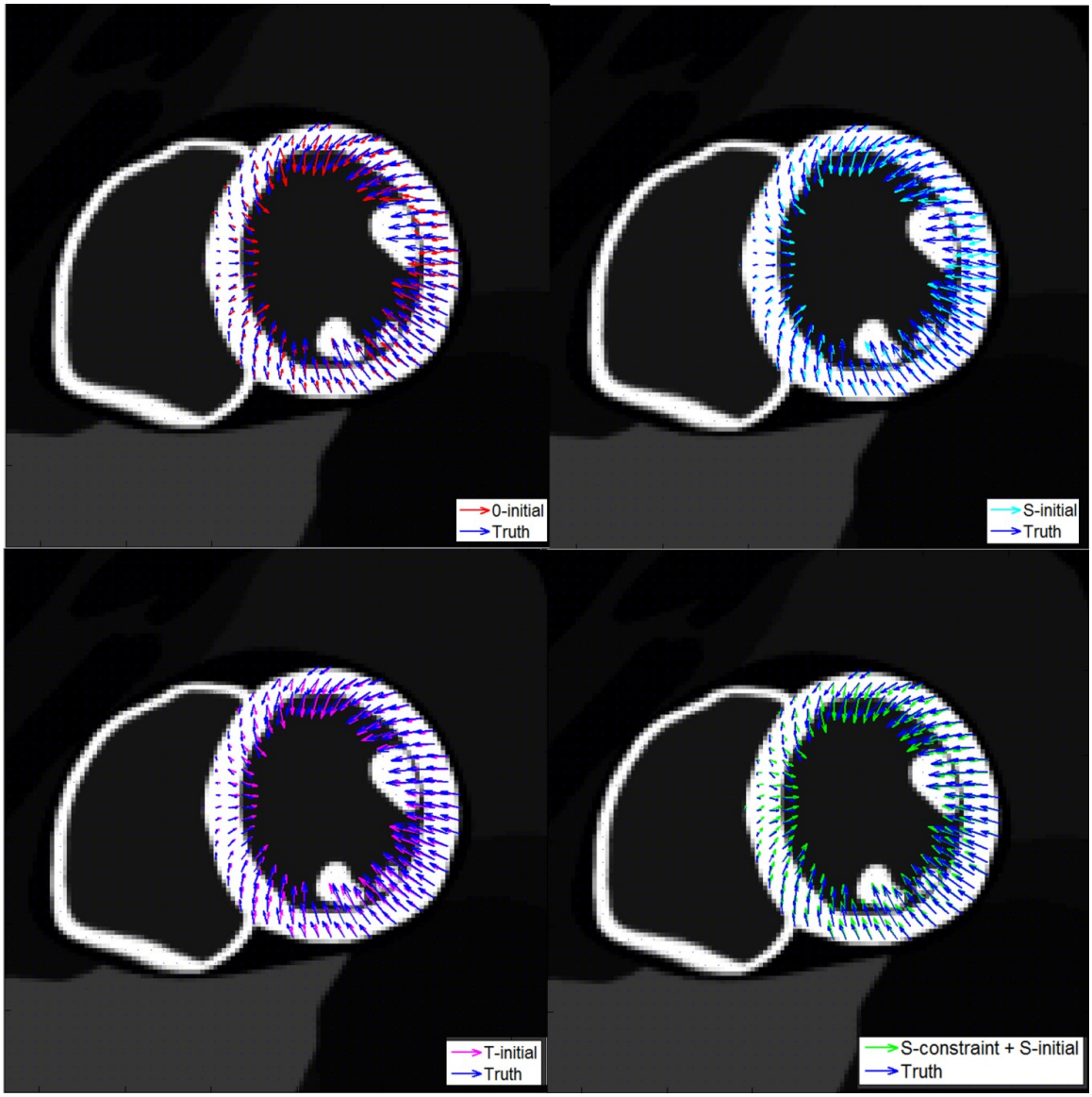

Figure 3-42 Cardiac motion estimation results using four methods for phantom image frame 1 at the non-twisting SA slice. The true MVF is plotted in blue arrows for comparison.

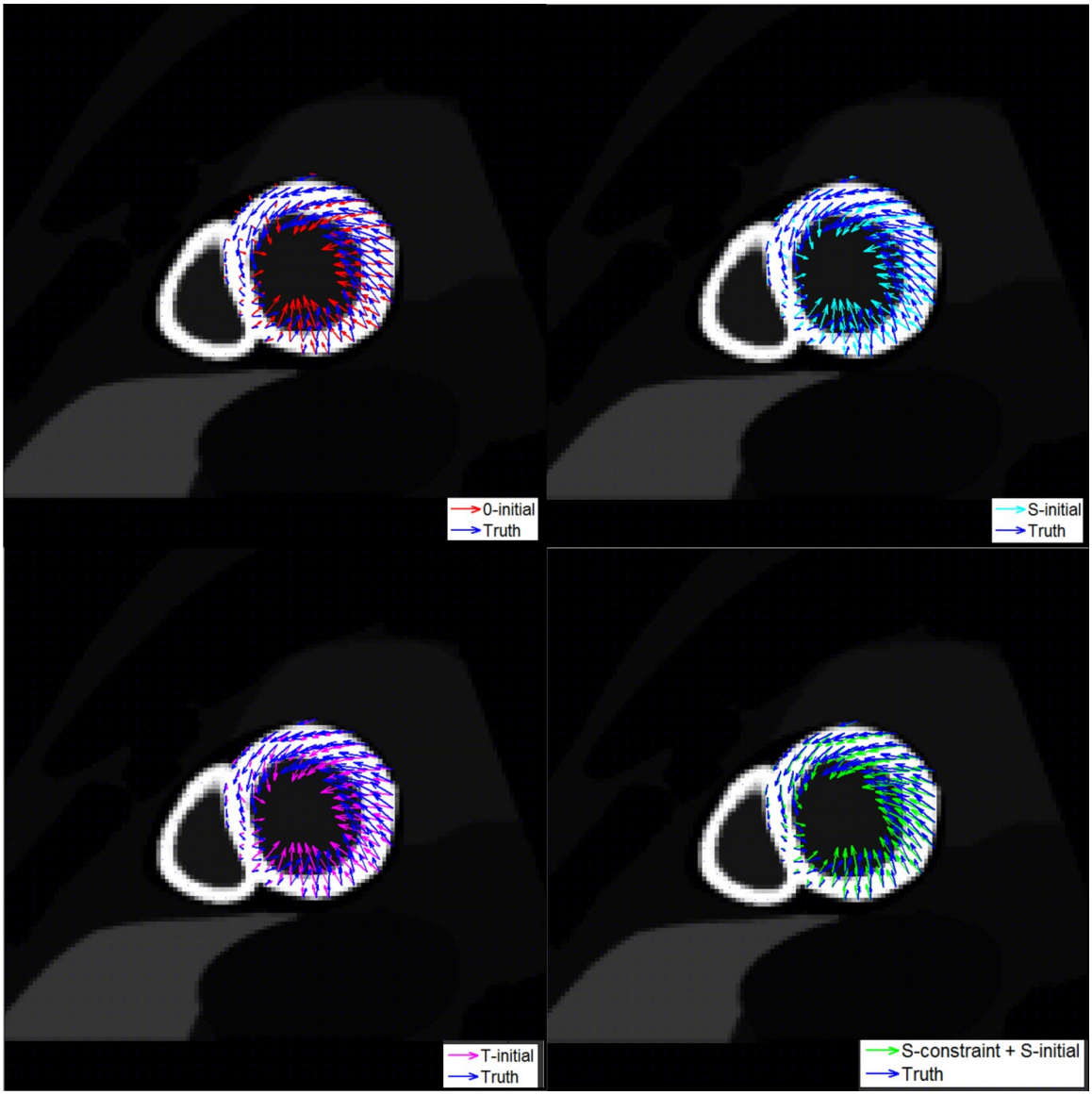

Figure 3-43 Cardiac motion estimation results using four methods for phantom image frame 1 at one apical SA slice. The true MVF is plotted in blue arrows for comparison.

Figure 3-44 shows the motion estimation result for phantom image at frame 1 in HLA view. Overall, the heart is contracting towards the apex. From apex to base, the longitudinal motion increases linearlly. The 0-initial underestimates the longitudinal motion especially for the basal region. The other three methods perform comparably well in estimating the longitudinal motion in most region of the myocardium.

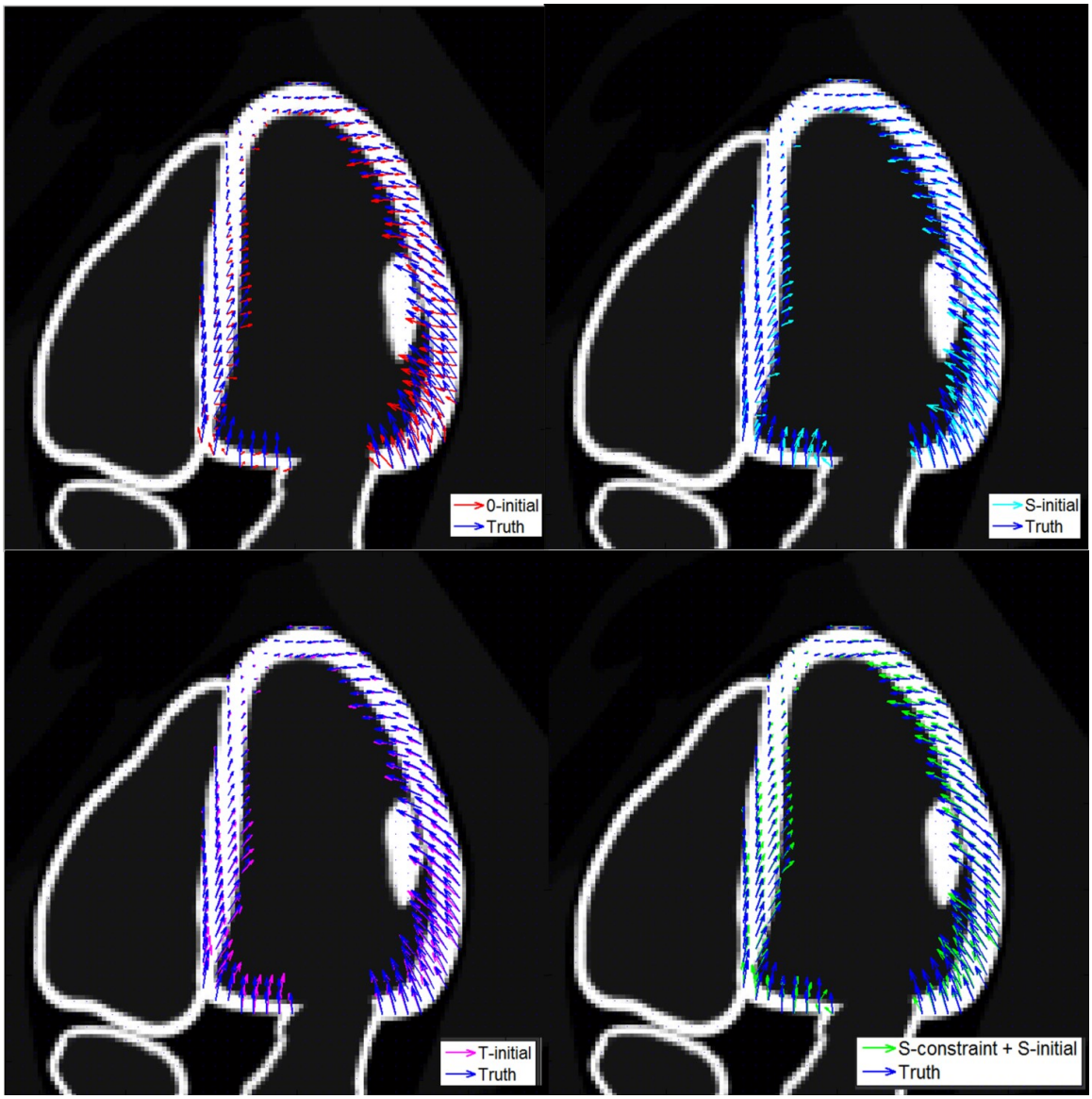

Figure 3-44 Cardiac motion estimation results using four methods for phantom image frame 1 at one HLA slice. The true MVF is plotted in blue arrows for comparison.

For the basal short-axis slice, we plot the error map of circumferential motion in Figure 3-45. It is obvious that the S-constraint + S-initial has the lowest error for most region. We also noticed that the error at the region near the posterior sulcus is smaller than the posterior region for all three initials, but without constraint, the advantage cannot be extended to other regions as the result achieved by S-constraint + S-initial method.

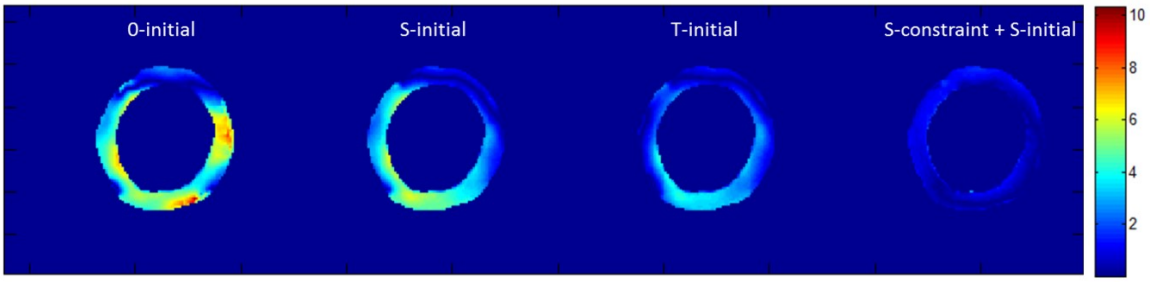

Figure 3-45 Error map of circumferential motion in basal SA slice by four methods.

Motion estimation error for the three sample slices were calculated and shown in Table 3-8, which confirms the observation in the figures above quantitatively. The average amplitude is the average absolute value of the three motion components and whole motion vector, therefore does not tell direction. The apical SA slice has the largest circumferential motion, and the smallest radial and longitudinal motion. The S-constrain + S-initial method significantly reduces the error in circumferential motion than other methods. The middle SA slice has medium radial motion and longitudinal motion, but the circumferential motion is too small to be estimated accurately. The basal SA slice has large radial and longitudinal motion, and medium circumferential motion. The circumferential motion is in the opposite direction to that in the apical SA slice. The S-constraint + S-initial method performs the best in circumferential motion estimation among four methods for both apical and basal SA slices. It also has superior accuracy in longitudinal motion estimation for all three slices. Overall, the T-initial and S-constraint + S-initial method are comparable in radial and longitudinal motion, but the later achieves more accurate estimation for the circumferential motion when it is large enough to estimate.

Table 3-8 Motion estimation error of four methods at three SA slices from results for phantom image of frame #1

Apical SA slice						
	average amplitude		0-initial	S-initial	T-initial	S-constraint + S-initial
Vr(mm)	2.25	RMSE_Vr(mm)	0.61	0.50	0.53	0.72
Vc(degree)	7.95	RMSE_Vc(degree)	8.32	7.61	6.53	2.87
Vl(mm)	1.01	RMSE_Vl(mm)	1.41	0.96	0.51	1.11
MVF(mm)	4.10	RMSE_MVF(mm)	2.91	2.44	1.94	1.58

Non-twisting SA slice						
	average amplitude		0-initial	S-initial	T-initial	S-constraint + S-initial
Vr(mm)	3.89	RMSE_Vr(mm)	1.14	0.91	0.51	0.74
Vc(degree)	0.88	RMSE_Vc(degree)	1.96	1.68	1.30	1.61
Vl(mm)	4.84	RMSE_Vl(mm)	3.72	2.36	1.08	1.02
MVF(mm)	6.69	RMSE_MVF(mm)	4.01	2.68	1.33	1.51
Basal SA slice						
	average amplitude		0-initial	S-initial	T-initial	S-constraint + S-initial
Vr(mm)	4.03	RMSE_Vr(mm)	1.05	0.66	0.51	0.78
Vc(degree)	2.82	RMSE_Vc(degree)	4.31	3.02	2.12	0.86
Vl(mm)	6.64	RMSE_Vl(mm)	5.08	3.26	1.09	1.02
MVF(mm)	8.34	RMSE_MVF(mm)	5.65	3.65	1.61	1.37

RESULTS FOR DIFFERENT SYSTEM RESOLUTIONS

GLOBAL MOTION ESTIMATION ERROR

The RMSEs obtained by four methods for noise-free simulation data of four system resolutions are plotted in Figure 3-46 to Figure 3-49.

For large-motion cardiac frames, the S-initial and S-constraint + S-initial methods are both able to achieve lower motion estimation error at the four simulated system resolutions. For small-motion cardiac frames, the improvement in motion estimation accuracy by using the feature motion is lost even for noise-free simulation of 0.6mm resolution.

It is observed that with decreased resolution, the RMSE of 0-initial tends to decrease while that of T-initial tends to increase. This phenomenon is especially prominent for frame 3, which has the largest cardiac motion in amplitude among four frames. As a result, the distinction between the best method T-initial and the worst method 0-initial becomes smaller for images of poorer resolution. Especially, at 4.5 mm

resolution, the difference in RMSE between T-initial and 0-initial is smaller than 1mm. This indicates that when the system resolution is very low, the initial estimate has limited influence on the motion estimation accuracy.

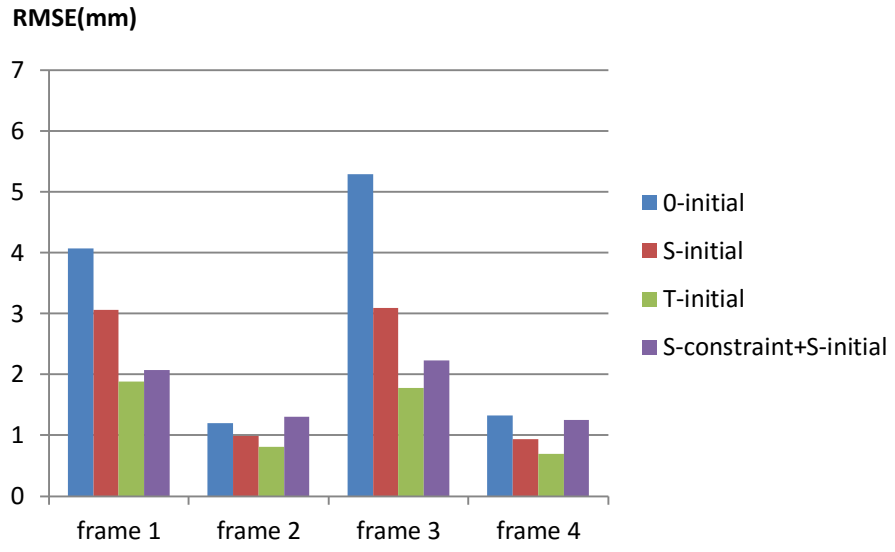

Figure 3-46 Motion estimation error RMSE for noise-free simulation data of 0.6mm resolution using four different methods.

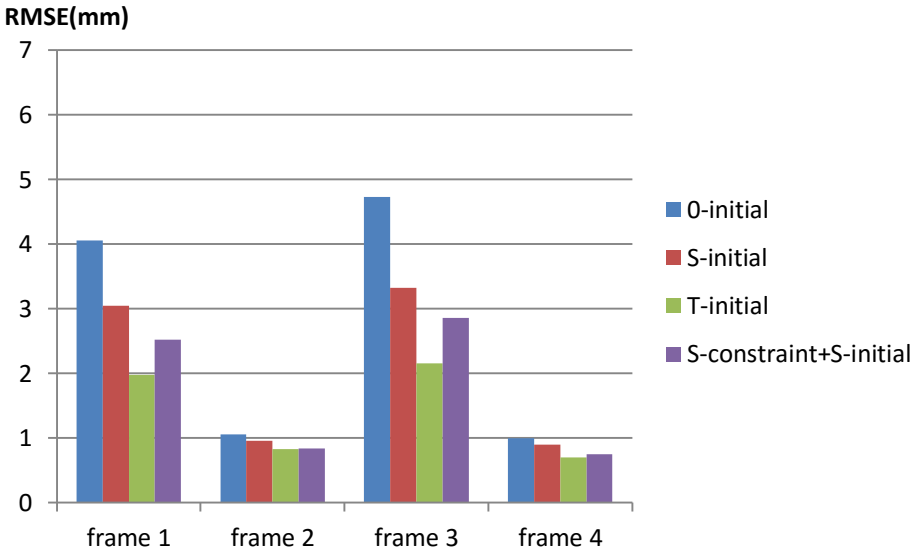

Figure 3-47 Motion estimation error RMSE for noise-free simulation data of 1.5mm resolution using four different methods.

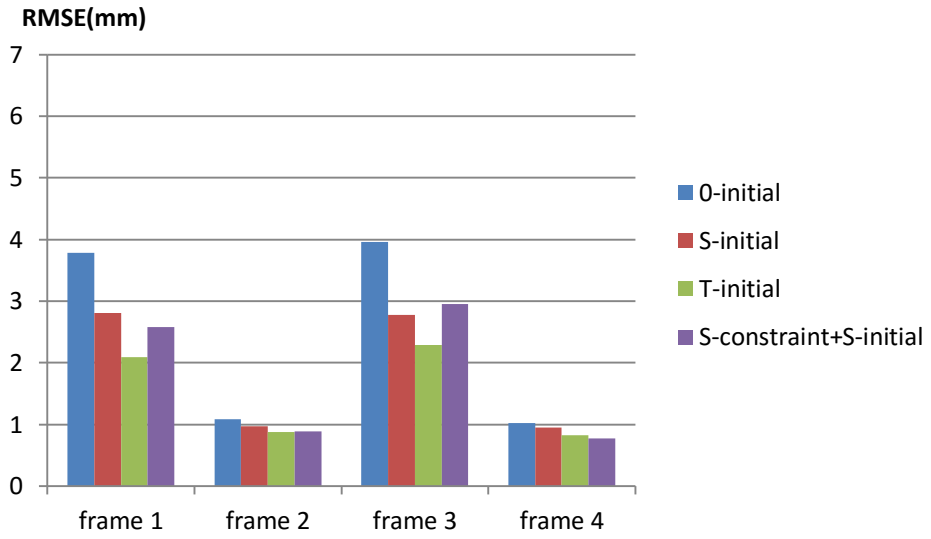

Figure 3-48 Motion estimation error RMSE for noise-free simulation data of 3mm resolution using four different methods.

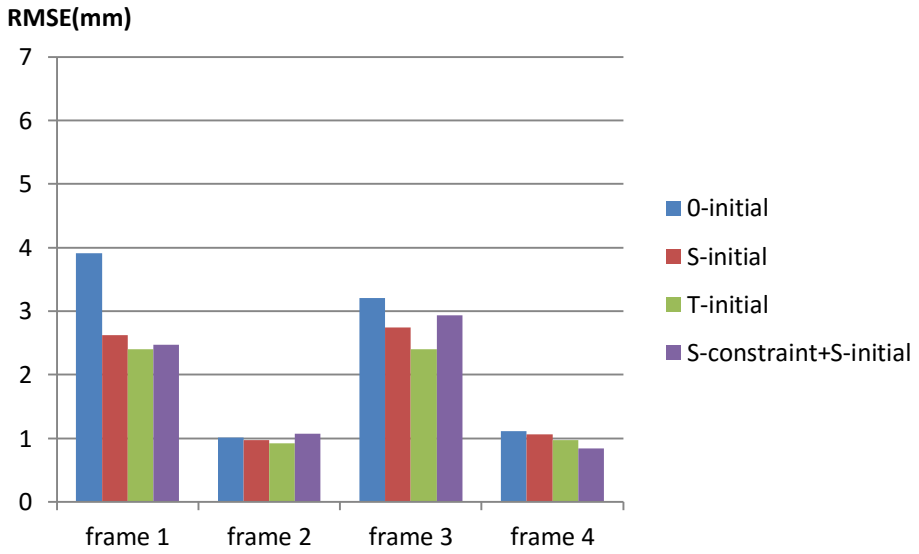

Figure 3-49 Motion estimation error RMSE for noise-free simulation data of 4.5 mm resolution using four different methods.

CARDIAC MOTION COMPONENT ANALYSIS

The global RMSEs for three motion components as well as the complete MVF by four methods in noise-free simulation data for frame 1 of different system resolutions are calculated and shown in Table 3-9. Different from the results in phantom image, the estimation of radial motion by S-constraint + S-initial method is even worse than the 0-initial for noise-free simulation data of 0.6mm resolution. This is caused by the overestimation of radial motion of the PIS, which is further extended to the whole myocardium

through cardiac motion model based initialization. Fortunately, with relatively accurate estimation of circumferential motion and longitudinal motion, the total error of S-constraint+ S-initial method is still comparable as the T-initial at 0.6mm resolution. Starting from 1.5mm resolution, the advantage of S-constraint + S-initial method in circumferential motion estimation reduces. Due to less accurate estimation of circumferential motion at lower system resolution, the error in circumferential motion by the S-constraint + S-initial method increases. Moreover, the error of radial motion by the S-constraint + S-initial method is consistently the largest for all resolutions. Although the total error is still smaller than the 0-initial, the improvement is mainly achieved by the accurate estimation of the longitudinal motion.

We also notice that the error of all three motion components by T-initial increases as the resolution degrades. This indicates that resolution has negative effect on the motion estimation accuracy even when the optical flow algorithm start with the true cardiac motion. The error in radial motion and circumferential motion by S-initial and S-constraint + S-initial also have a similar trend. However, the results for 0-initial does not follow the same trend as the other three methods except the radial motion is estimated with lower accuracy as resolution degrades from 1.5mm to 4.5 mm.

Table 3-9 Global error RMSE of three cardiac motion components in frame 1 from noise-free simulation data of different system resolutions

0.6mm resolution						
			0-initial	S-initial	T-initial	S-constraint + S-initial
Vr(mm)	3.33	RMSE_Vr(mm)	1.23	0.65	0.56	1.57
Vc(degree)	3.8	RMSE_Vc(degree)	4.92	4.82	4.64	3.01
Vl(mm)	3.77	RMSE_Vl(mm)	3.58	2.60	1.15	1.06
MVF(mm)	5.94	RMSE_MVF(mm)	3.39	2.55	1.57	1.73
1.5 mm resolution						
			0-initial	S-initial	T-initial	S-constraint + S-initial
Vr(mm)	3.33	RMSE_Vr(mm)	1.04	0.66	0.58	1.95

Vc(degree)	3.8	RMSE_Vc(degree)	4.72	5.00	4.92	4.92
Vl(mm)	3.77	RMSE_Vl(mm)	3.64	2.57	1.23	1.09
MVF(mm)	5.94	RMSE_MVF(mm)	4.06	3.04	1.98	2.53
3.0 mm resolution						
			0-initial	S-initial	T-initial	S-constraint + S-initial
Vr(mm)	3.33	RMSE_Vr(mm)	1.00	0.70	0.64	1.93
Vc(degree)	3.8	RMSE_Vc(degree)	5.51	5.70	5.11	5.30
Vl(mm)	3.77	RMSE_Vl(mm)	3.28	2.19	1.26	1.00
MVF(mm)	5.94	RMSE_MVF(mm)	3.79	2.81	2.10	2.58
4.5 mm resolution						
			0-initial	S-initial	T-initial	S-constraint + S-initial
Vr(mm)	3.33	RMSE_Vr(mm)	1.37	0.73	1.13	1.53
Vc(degree)	3.8	RMSE_Vc(degree)	5.89	6.10	5.18	5.88
Vl(mm)	3.77	RMSE_Vl(mm)	3.29	1.88	1.50	0.96
MVF(mm)	5.94	RMSE_MVF(mm)	3.91	2.62	2.40	2.47

To look into more details on the motion estimation results other than a global evaluation, we plotted the MVF estimated using the four methods along with the truth. The following figures show the results in three representatively SA slices for noise-free 4.5mm resolution simulation data at frame 1.

Figure 3-50 shows that at the basal SA slice, the heart is contracting as well as rotating in the counterclockwise direction. The S-constraint + S-initial method performed the best among all the methods. The MVF estimated with this method matches very well with the truth. The 0-initial has difficulty detecting the circumferential motion for most regions on this slice, and at the anterior-septal region, the estimated MVF point to the wrong direction. Similar situation is observed for S-initial and T-initial. Without extra constraint in the algorithm, the circumferential motion is penalized during the optimization of the cost function.

At the non-rotating plane shown in Figure 3-51, the heart is contracting but has minimal circumferential motion. Therefore, the performance of four methods is comparable. The 0-initial has large error in both anterior-septal and posterior region. The S-initial and T-initial are slightly better in these two regions. The S-constraint + S-initial method performs better than 0-initial in the posterior region, especially the region near the PIS where even the T-initial has difficulty estimating the accurate MVF. However, in the anterior region, it fails to detect the circumferential motion, which is similar to other three methods.

On the apical slice, which has significant circumferential motion, the four methods all have difficulty estimating the MVF, and no method shows obvious advantage over the rest. The feature-based method does no better than the other methods, because the extracted circumferential motion of IS is inaccurate especially at the apical region.

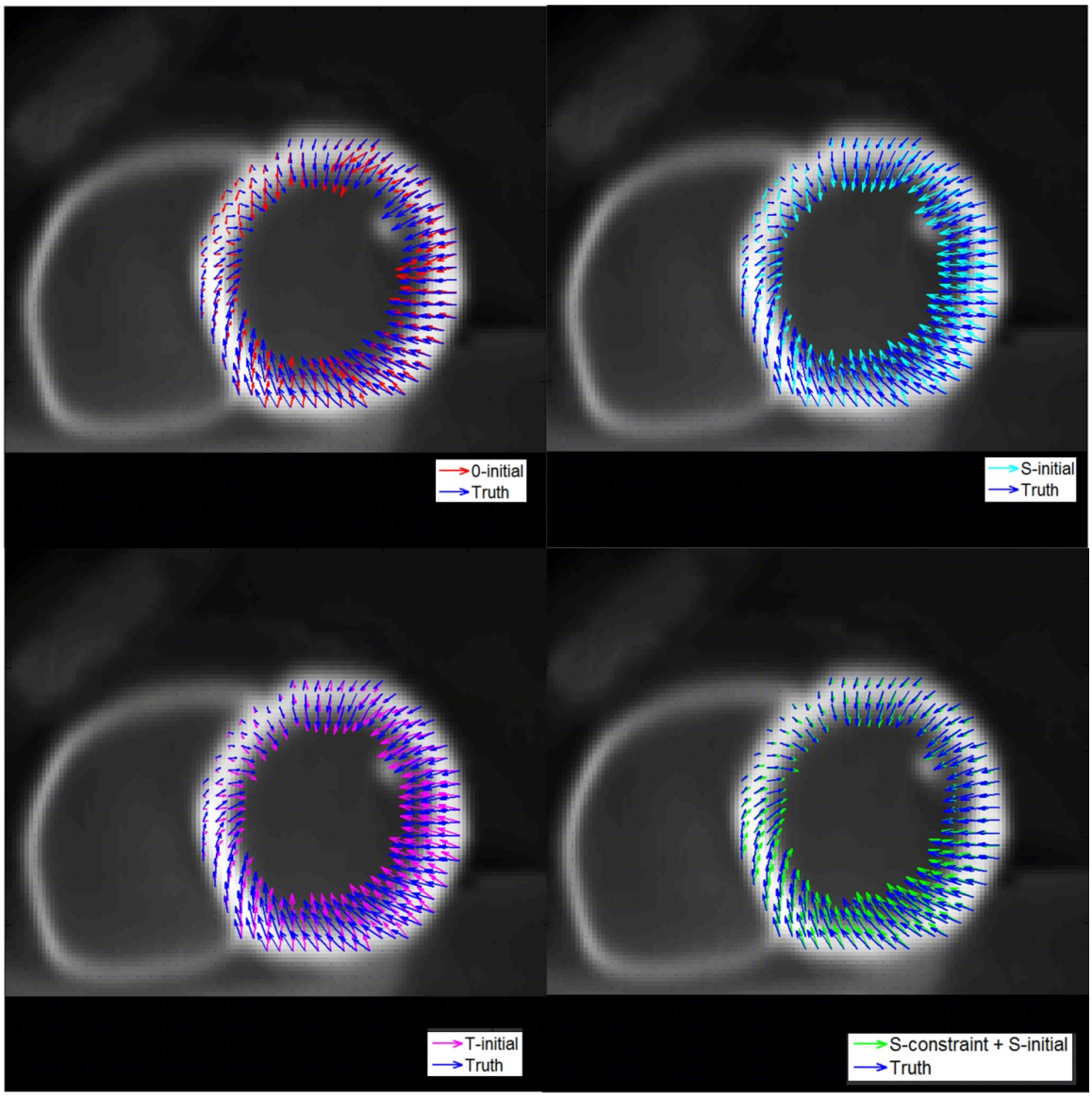

Figure 3-50 Cardiac motion estimation results using four methods for noise-free 4.5 mm resolution simulation data of frame 1 at a basal SA slice. The true MVF is plotted in blue arrows for comparison.

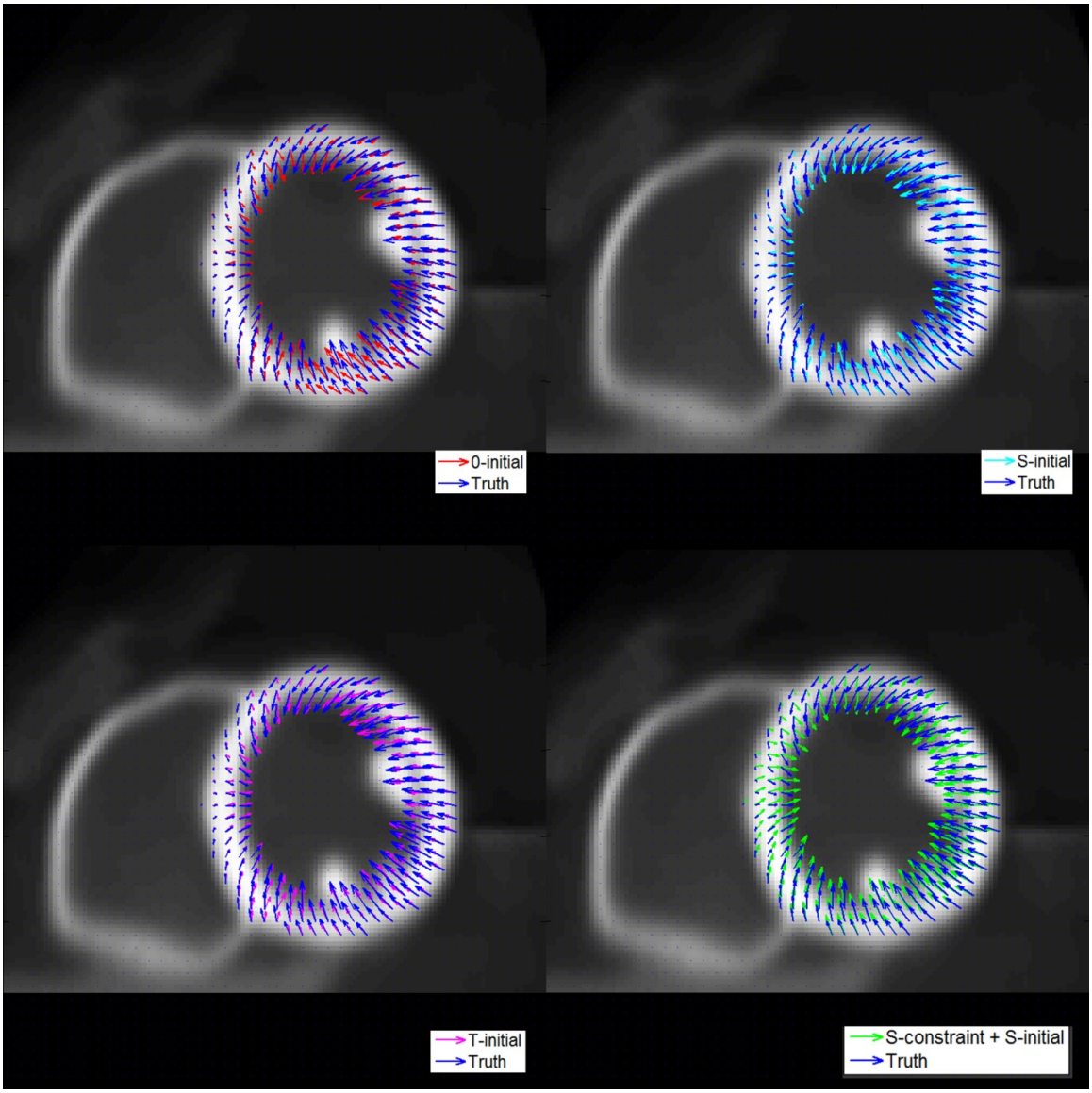

Figure 3-51 Cardiac motion estimation results using four methods for noise-free 4.5 mm resolution simulation data of frame 1 at the non-twisting SA slice. The true MVF is plotted in blue arrows for comparison.

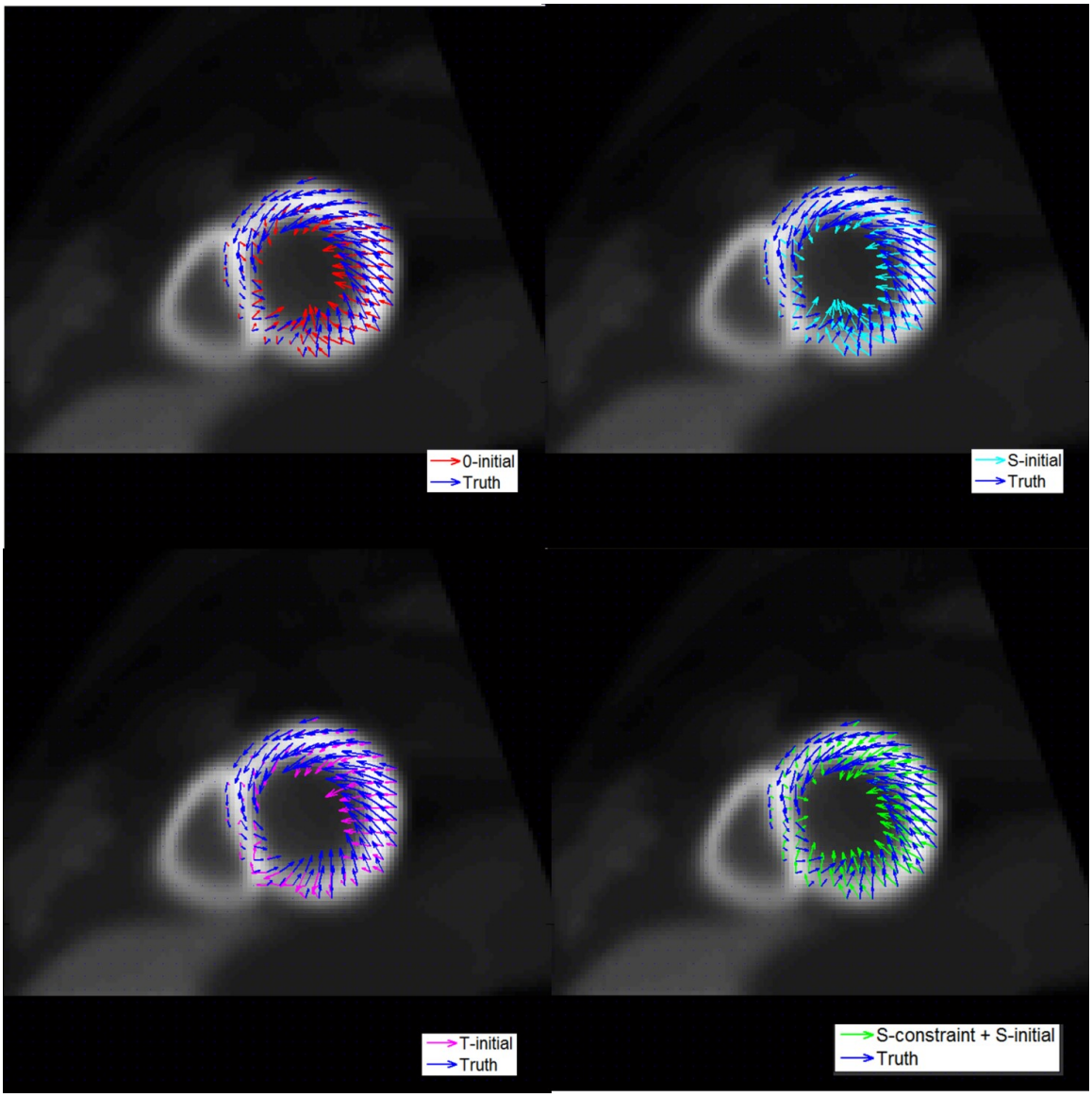

Figure 3-52 Cardiac motion estimation results using four methods for noise-free 4.5 mm resolution simulation data of frame 1 at an apical SA slice. The true MVF is plotted in blue arrows for comparison.

Although it seems that the S-constraint + S-initial method does not perform well in circumferential motion when evaluated using the global motion estimation error, its result for different regions of the heart is quite different as observed from the figures above. For quantitatively evaluation, we calculated motion estimation error for three SA slices of the 4.5mm resolution noise-free simulation data at frame 1and showed the results in Table 3-10. In the apical slice where the circumferential motion is the largest, the four methods all have difficulty estimating the circumferential motion. For the zero-rotating slice, the errors in circumferential motion by four methods are much larger than the average amplitude of the truth, with S-

constraint + S-initial yielding the largest error. However, at the basal slice, the S-constraint + S-initial method achieves the most accurate estimation of circumferential motion among all the methods. Therefore, although the global errors in circumferential motion for all the methods are similar, the feature-based method is able to achieve more accurate estimation of this component at the basal slice, which is more meaningful considering the large radius of myocardial wall at the base.

Table 3-10 Motion estimation error of four methods at three SA slices for noise-free simulation data of frame 1at 4.5 mm resolution

Apical SA slice						
			0-initial	S-initial	T-initial	S-constraint + S-initial
Vr(mm)	2.25	RMSE_Vr(mm)	0.74	0.67	1.90	1.40
Vc(degree)	7.95	RMSE_Vc(degree)	7.58	9.06	8.12	7.55
Vl(mm)	1.01	RMSE_Vl(mm)	1.34	1.13	1.37	1.10
MVF(mm)	4.10	RMSE_MVF(mm)	2.73	2.98	3.31	2.80
Non-rotating SA slice						
			0-initial	S-initial	T-initial	S-constraint + S-initial
Vr(mm)	3.89	RMSE_Vr(mm)	1.05	0.62	0.64	1.57
Vc(degree)	0.88	RMSE_Vc(degree)	1.88	1.78	1.86	2.88
Vl(mm)	4.84	RMSE_Vl(mm)	2.94	1.94	1.54	0.92
MVF(mm)	6.69	RMSE_MVF(mm)	3.25	2.20	1.89	2.31
Basal SA slice						
			0-initial	S-initial	T-initial	S-constraint + S-initial
Vr(mm)	4.03	RMSE_Vr(mm)	1.16	0.67	0.66	1.57

Vc(degree)	2.82	RMSE_Vc(degree)	3.72	3.65	3.30	0.96
Vl(mm)	6.64	RMSE_Vl(mm)	6.20	2.77	1.51	0.82
MVF(mm)	8.34	RMSE_MVF(mm)	6.57	3.41	2.36	1.85

RESULTS FOR DIFFERENT NOISE LEVELS

GLOBAL MOTION ESTIMATION ERROR

The RMSEs obtained by four methods for simulation data of 0.6mm system resolution at four noise levels (NF, 8N, 2N and 0.5N) are plotted in Figure 3-46 Figure 3-54 to Figure 3-57. The results for phantom image are shown in Figure 3-53 again for comparison. For large-motion cardiac frames, the S-initial and S-constraint + S-initial methods are both able to achieve lower motion estimation error at the four simulated noise levels. The improvement in motion estimation accuracy by using the feature motion is lost for small-motion cardiac frames even with noise-free simulation. This is because the IS motion in small-motion frames is very small and cannot be estimated accurately. Notice that at higher noise level, the error by S-constraint + S-initial method is much larger than the other methods, due to inaccurate feature extraction.

A similar phenomenon is observed from the change of RMSEs as noise increases: the RMSE of 0-initial tends to decrease while that of T-initial tends to increase. Again, this phenomenon is most prominent for frame 3, which has the largest cardiac motion among four frames. The distinction between the best method T-initial and the worst method 0-initial becomes smaller for images of higher noise level. Since noisy images were smoothed before feature extraction and motion estimation, the increase of noise is translated to the decrease of image resolution. Therefore, the influence of noise is analogous to the influence of system resolution as observed in Figure 3-46 to Figure 3-49.

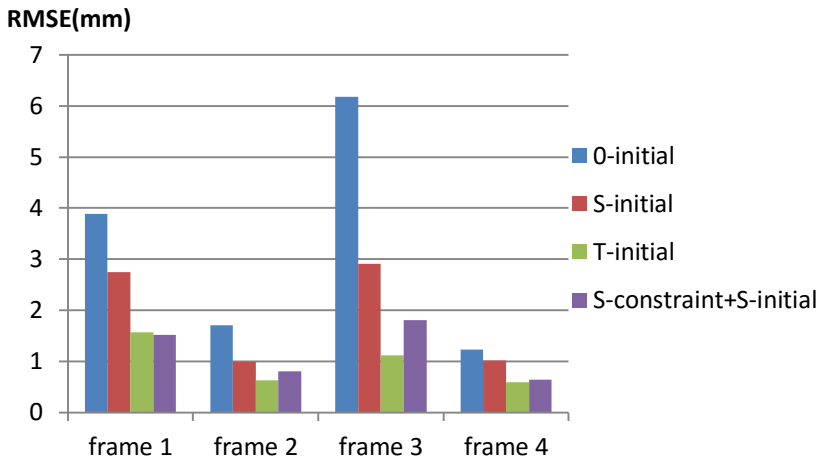

Figure 3-53 Motion estimation error RMSE for phantom images using four different methods.

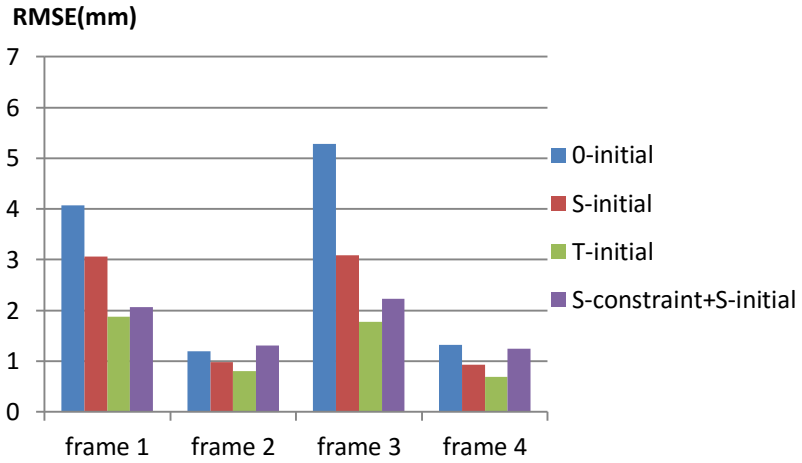

Figure 3-54 Motion estimation error RMSE for noise-free simulation data of 0.6mm resolution using four different methods.

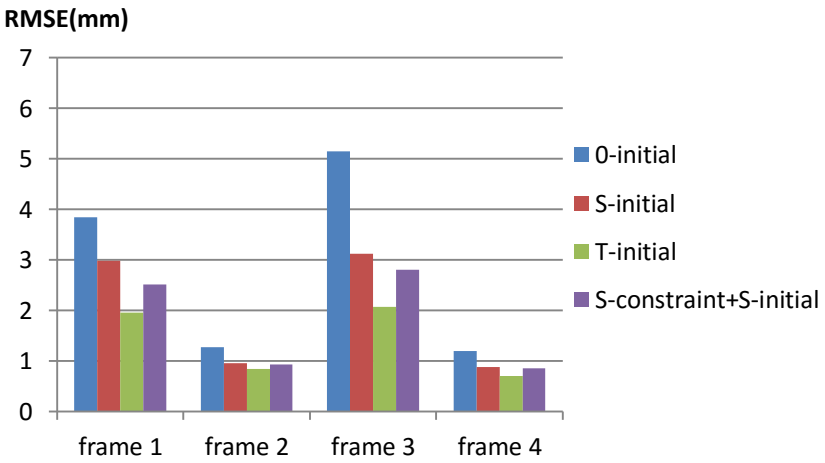

Figure 3-55 Motion estimation error RMSE for simulation data of 0.6mm resolution at noise level 8N using four different methods.

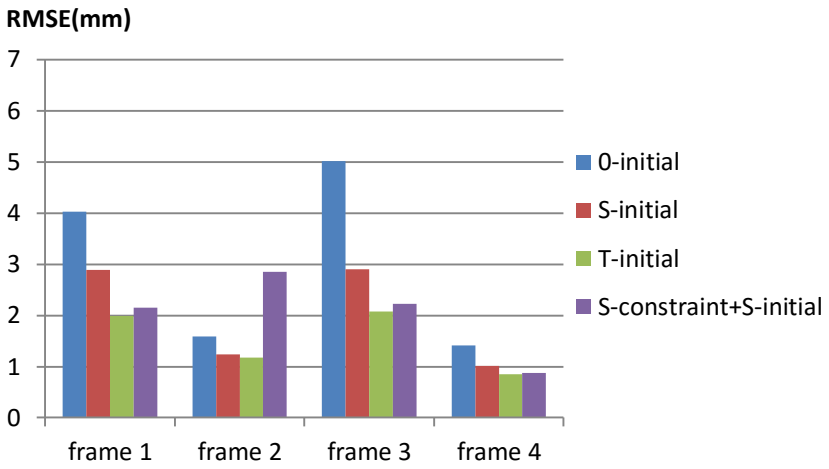

Figure 3-56 Motion estimation error RMSE for simulation data of 0.6mm resolution at noise level 2N using four different methods.

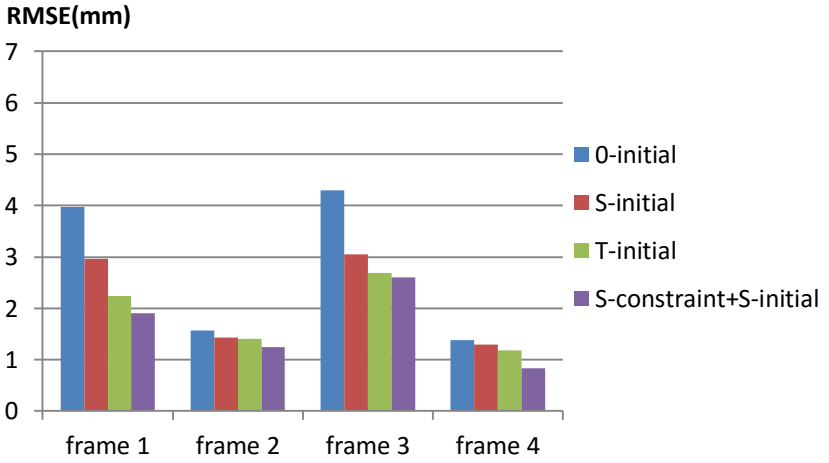

Figure 3-57 Motion estimation error RMSE for simulation data of 0.6mm resolution at noise level 0.5N using four different methods.

CARDIAC MOTION COMPONENT ANALYSIS

The global RMSEs for three motion components as well as the complete MVF by four methods in 0.6mm resolution simulation data of frame 1 at different noise levels are calculated and shown in Table 3-11. The error in radial motion estimation by the S-constraint + S-initial method is the largest among four methods at all noise levels due to overestimation of the radial motion of the PIS. However, the feature-based method is able to improve both the circumferential motion and longitudinal motion. The S-initial only method achieves comparable accuracy in radial motion and circumferential motion as the T-initial, but its error in longitudinal motion is noticeably larger. The overall motion estimation accuracy of S-constraint + S-initial

method is superior to the 0-initial, and comparable as the T-initial. For all the four methods, the error in circumferential motion shows obvious increase when the noise increases with an exception at noise level 2N.

Table 3-11 Global error RMSE of three cardiac motion components in 0.6mm simulation data of frame 1 at different noise levels.

noise -free						
			0-initial	S-initial	T-initial	S-constraint + S-initial
Vr(mm)	3.33	RMSE_Vr(mm)	1.23	0.65	0.56	1.57
Vc(degree)	3.8	RMSE_Vc(degree)	4.92	4.82	4.64	3.01
Vl(mm)	3.77	RMSE_Vl(mm)	3.58	2.60	1.15	1.06
MVF(mm)	5.94	RMSE_MVF(mm)	3.39	2.55	1.57	1.73
noise level 8N						
			0-initial	S-initial	T-initial	S-constraint + S-initial
Vr(mm)	3.33	RMSE_Vr(mm)	0.98	0.78	0.60	2.07
Vc(degree)	3.8	RMSE_Vc(degree)	5.68	5.63	5.54	4.08
Vl(mm)	3.77	RMSE_Vl(mm)	3.37	2.45	1.18	1.00
MVF(mm)	5.94	RMSE_MVF(mm)	3.85	2.98	1.96	2.52
noise level 2N						
			0-initial	S-initial	T-initial	S-constraint + S-initial
Vr(mm)	3.33	RMSE_Vr(mm)	1.03	0.73	0.68	1.68
Vc(degree)	3.8	RMSE_Vc(degree)	5.44	5.20	5.09	3.47
Vl(mm)	3.77	RMSE_Vl(mm)	3.53	2.34	1.18	0.98
MVF(mm)	5.94	RMSE_MVF(mm)	3.36	2.41	1.66	1.79
noise level 0.5N						
			0-initial	S-initial	T-initial	S-constraint + S-initial

Vr(mm)	3.33	RMSE_Vr(mm)	1.14	0.86	0.81	1.21
Vc(degree)	3.8	RMSE_Vc(degree)	6.51	5.93	5.72	4.36
Vl(mm)	3.77	RMSE_Vl(mm)	3.39	2.35	1.39	0.95
MVF(mm)	5.94	RMSE_MVF(mm)	3.98	2.97	2.24	1.90

The following figures show the results in three representatively SA slices of frame 1for 0.6mm resolution simulation data at noise level 0.5N. Figure 3-58 shows that at the basal SA slice, the S-constraint + S-initial method performs exceedingly well among all the methods. The 0-initial, S-initial and T-initial all fail to detect the circumferential motion of the myocardium at the posterior region, meanwhile they also generate inaccurate estimation of this component at the anterior septal region. At the non-rotating SA slice, the difference among four methods is negligible, except that the S-constraint + S-initial method yields overestimated radial motion at the septal region. In Figure 3-60, all of the four methods underestimate the circumferential motion on the apical slice, which is different from the results for noise-free simulation data of 0.6mm resolution at the apical SA slice. Figure 3-61 shows that although with some extent of underestimation, the S-constraint + S-initial method provides better detection of the circumferential motion than other three methods, which fail to detect it. This is because that at higher noise level, the circumferential motion of IS is underestimated at the apical region.

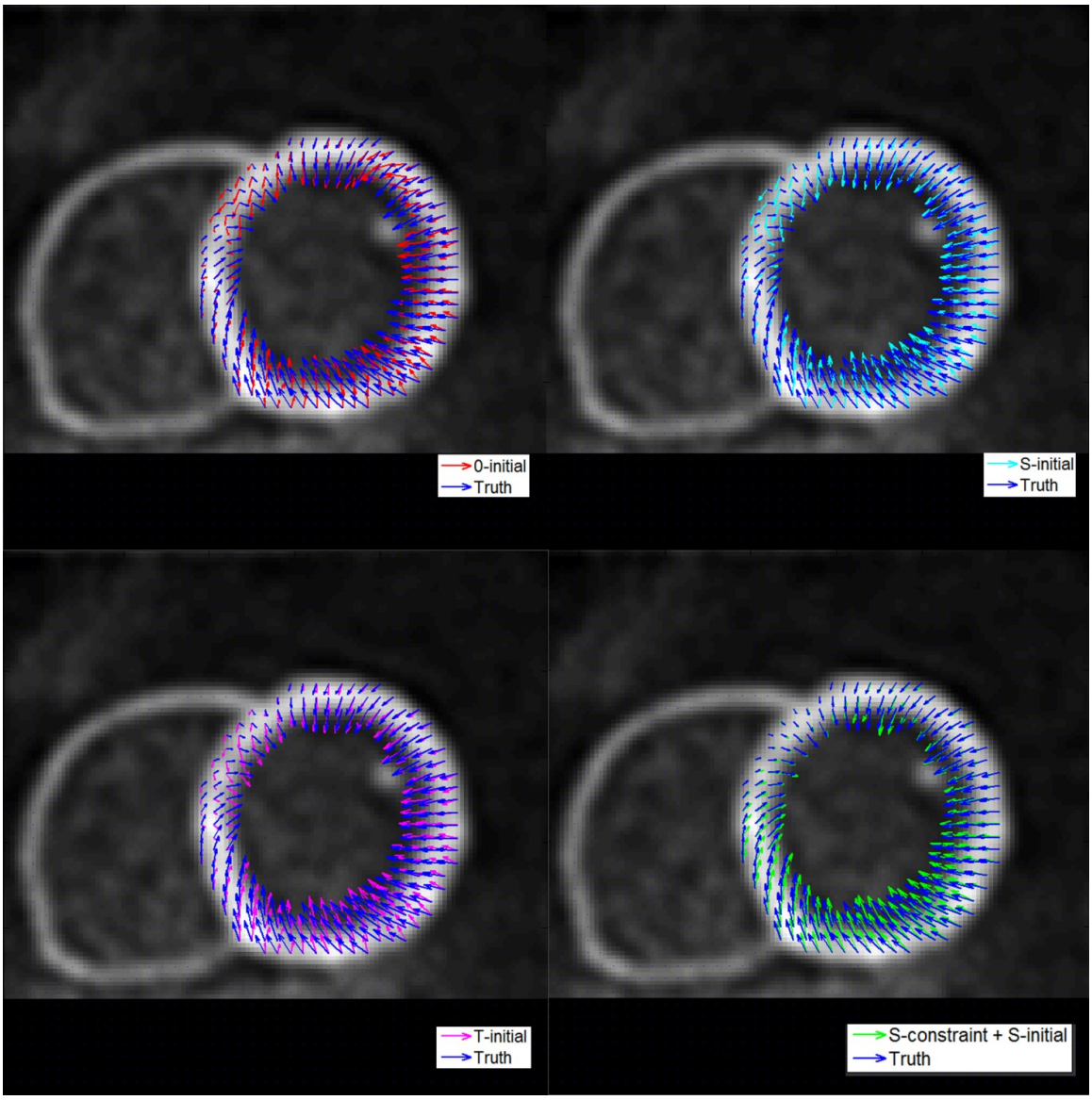

Figure 3-58 Cardiac motion estimation results using four methods for 0.6 mm resolution noise-level 0.5N simulation data of frame 1 at a basal SA slice. The true MVF is plotted in blue arrows for comparison.

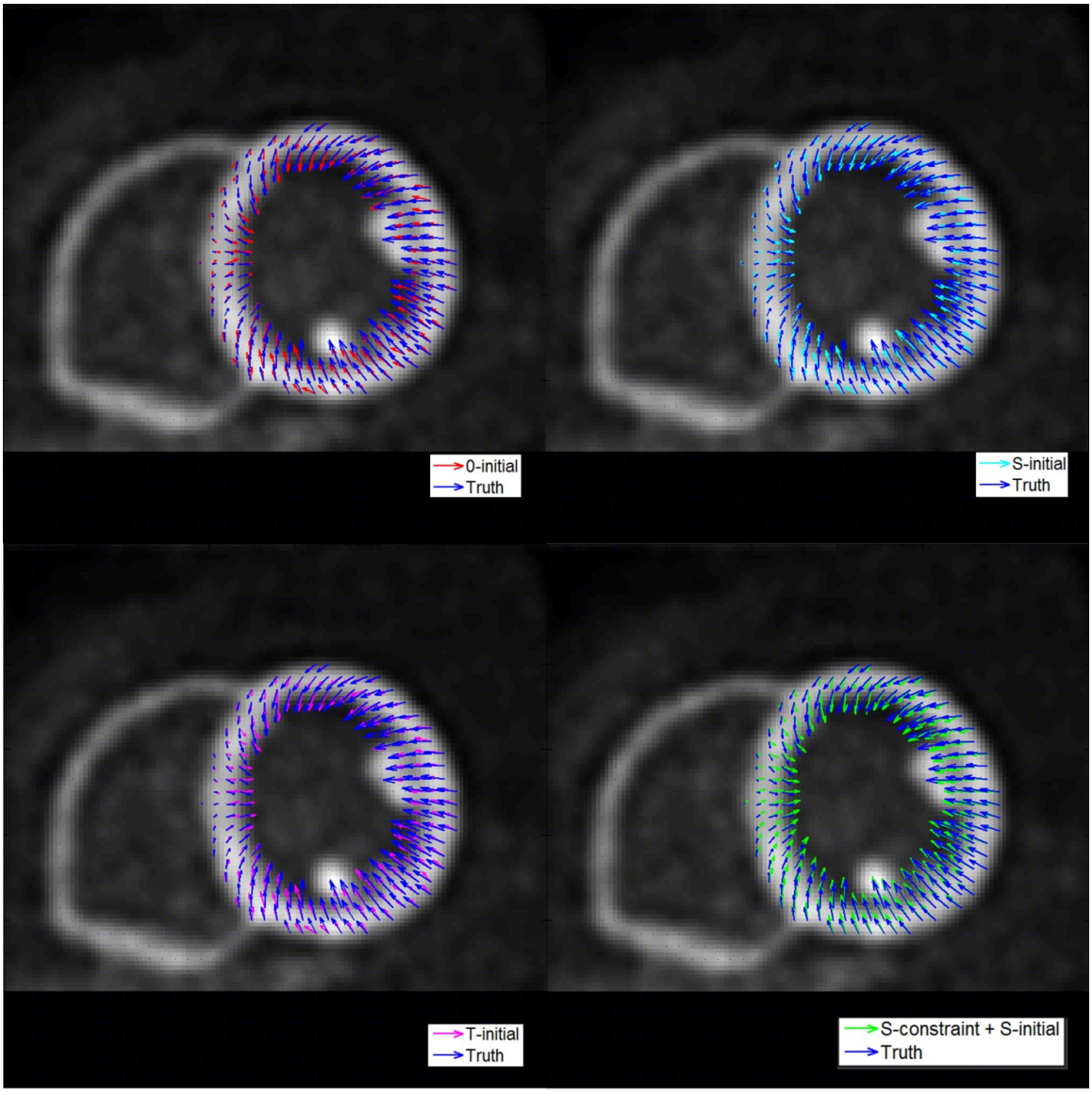

Figure 3-59 Cardiac motion estimation results using four methods for 0.6 mm resolution noise- level 0.5N simulation data of frame 1 at the non-twisting SA slice. The true MVF is plotted in blue arrows for comparison.

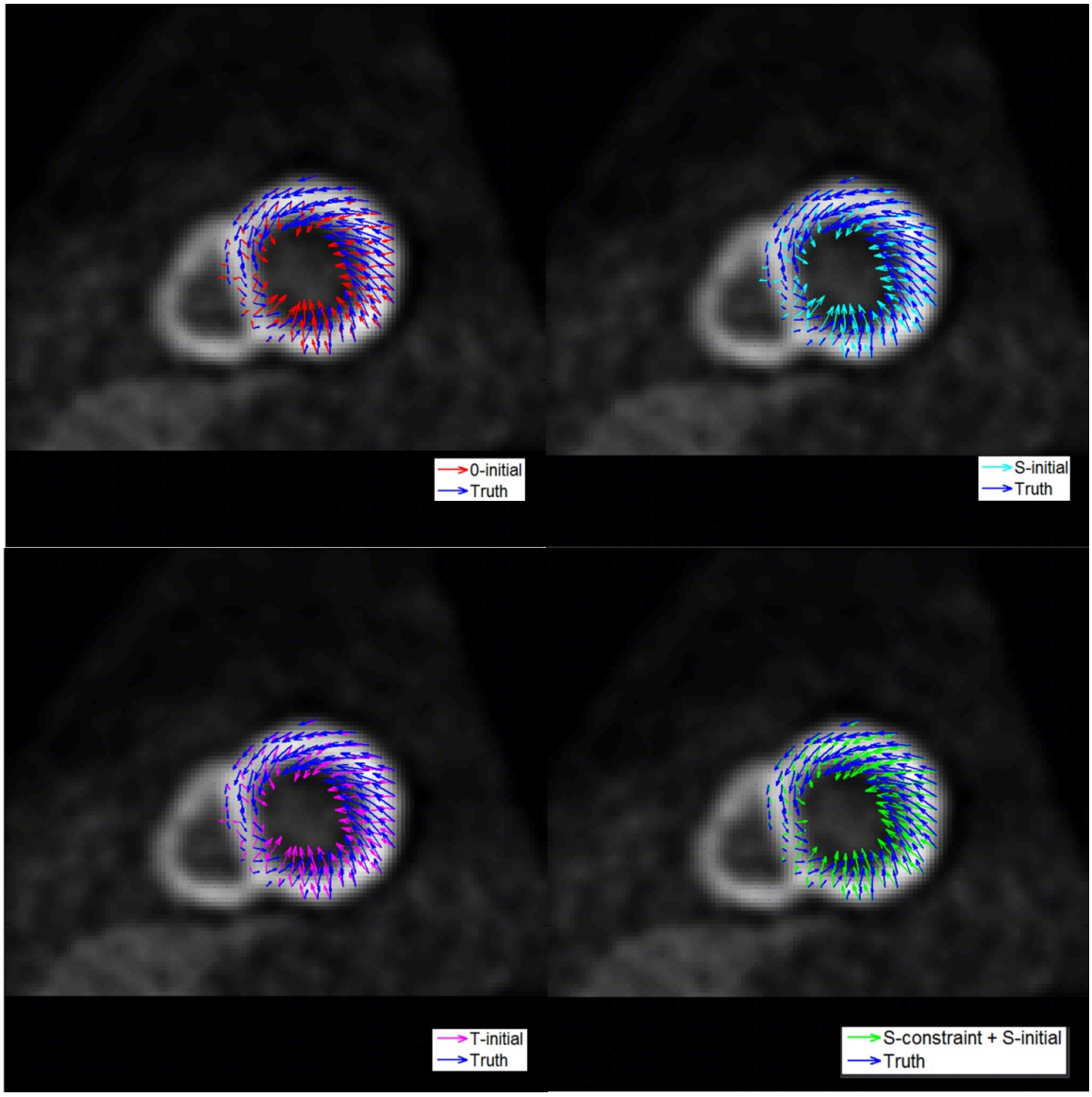

Figure 3-60 Cardiac motion estimation results using four methods for 0.6 mm resolution noise- level 0.5N simulation data of frame 1 at an apical SA slice. The true MVF is plotted in blue arrows for comparison.

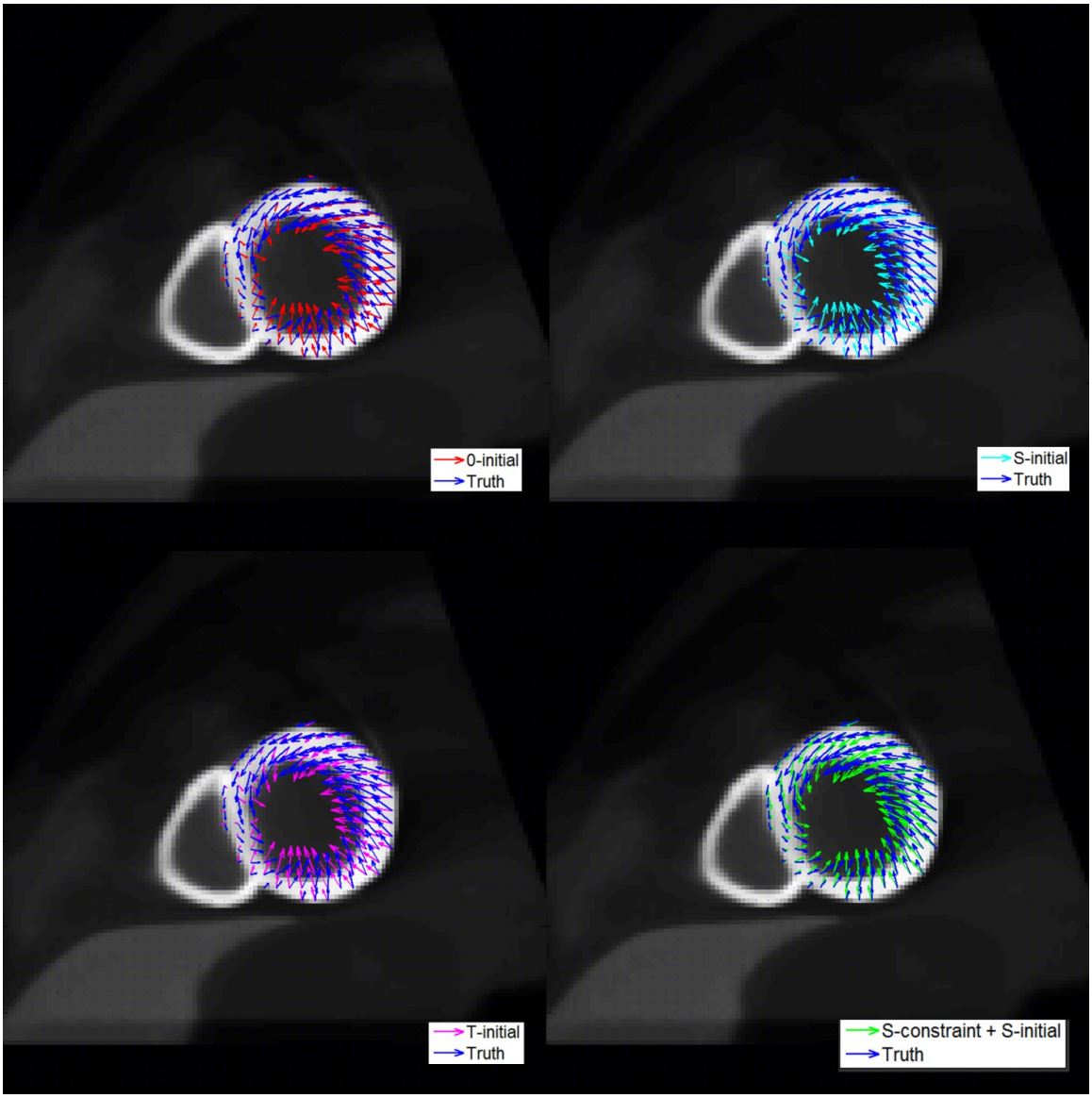

Figure 3-61 Cardiac motion estimation results using four methods for noise-free 0.6 mm resolution simulation data of frame 1 at an apical SA slice. The true MVF is plotted in blue arrows for comparison.

Quantitative evaluation of motion estimation accuracy for the three slices in frame 1 from noise-free data set and noise-level 0.5N data set is shown in the following tables. At the apical SA slice, which has large circumferential motion, the S-constraint + S-initial method achieves significantly more accurate estimation of this component than other three methods for noise-free data. However, the corresponding value of RMSE of circumferential motion for noise level 0.5N is much larger than for noise-free data, and the difference to the results of other methods is much smaller.

Table 3-12 Motion estimation error of four methods at three SA slices for 0.6mm resolution noise-free simulation data of frame 1

Apical SA slice						
			0-initial	S-initial	T-initial	S-constraint + S-initial
Vr(mm)	2.25	RMSE_Vr(mm)	0.68	0.53	0.55	1.44
Vc(degree)	7.95	RMSE_Vc(degree)	7.96	7.70	7.47	2.00
Vl(mm)	1.01	RMSE_Vl(mm)	1.23	1.02	0.72	1.16
MVF(mm)	4.10	RMSE_MVF(mm)	2.75	2.53	2.34	1.97
Non-rotating SA slice						
			0-initial	S-initial	T-initial	S-constraint + S-initial
Vr(mm)	3.89	RMSE_Vr(mm)	1.35	0.52	0.52	1.62
Vc(degree)	0.88	RMSE_Vc(degree)	1.77	1.56	1.32	1.77
Vl(mm)	4.84	RMSE_Vl(mm)	3.73	2.75	1.33	1.05
MVF(mm)	6.69	RMSE_MVF(mm)	4.05	2.91	1.55	2.13
Basal SA slice						
			0-initial	S-initial	T-initial	S-constraint + S-initial
Vr(mm)	4.03	RMSE_Vr(mm)	1.49	0.99	0.62	1.62
Vc(degree)	2.82	RMSE_Vc(degree)	3.04	3.32	3.15	1.33
Vl(mm)	6.64	RMSE_Vl(mm)	6.29	4.35	1.46	1.09
MVF(mm)	8.34	RMSE_MVF(mm)	6.62	4.76	2.24	2.08

Table 3-13 Motion estimation error of four methods at three SA slices for 0.6mm resolution simulation data of frame 1 at noise level 0.5N

Apical SA slice						
			0-initial	S-initial	T-initial	S-constraint + S-initial
Vr(mm)	2.25	RMSE_Vr(mm)	0.98	0.86	0.83	1.12
Vc(degree)	7.95	RMSE_Vc(degree)	8.39	7.76	7.55	5.05
Vl(mm)	1.01	RMSE_Vl(mm)	1.56	1.23	1.03	1.10
MVF(mm)	4.10	RMSE_MVF(mm)	3.07	2.70	2.53	2.14
Non-rotating SA slice						
			0-initial	S-initial	T-initial	S-constraint + S-initial
Vr(mm)	3.89	RMSE_Vr(mm)	1.03	0.81	0.81	1.22
Vc(degree)	0.88	RMSE_Vc(degree)	1.35	1.15	1.30	1.67
Vl(mm)	4.84	RMSE_Vl(mm)	3.53	2.60	1.65	0.92
MVF(mm)	6.69	RMSE_MVF(mm)	3.72	2.78	1.92	1.75
Basal SA slice						
			0-initial	S-initial	T-initial	S-constraint + S-initial
Vr(mm)	4.03	RMSE_Vr(mm)	1.23	0.97	0.94	1.26
Vc(degree)	2.82	RMSE_Vc(degree)	4.66	4.14	3.77	0.95
Vl(mm)	6.64	RMSE_Vl(mm)	5.62	3.64	1.75	0.84
MVF(mm)	8.34	RMSE_MVF(mm)	6.23	4.31	2.77	1.59

COMBINATION OF RESOLUTION AND NOISE

As shown in the previous sections, both resolution and noise influence the performance of feature-guided cardiac motion estimation method by affecting the accuracy of extracted motion of the feature. At 4.5mm system resolution, the feature-based method already lost its advantage in detecting the circumferential

motion both globally and regionally. At 1.5mm resolution, the global error in circumferential motion by the feature-based method is larger than 0-initial.

As show in Figure 3-62, at 3.0mm resolution and noise level 2N, the motion of extracted PIS is not very accurate for both the circumferential motion and the radial motion. Comparing with the extraction results in noise-free case, both motion components are noisier. The radial motion along the sulcus curve is less smooth, and the linearity of the circumferential motion is much reduced. The confidence of determination $R^2$of the linear regression of circumferential motion curve reduces from 0.86 in noise-free case to 0.44 at noise level 2N. S-initial was created based on the linear assumption of the circumferential motion and applied to the motion estimation of the images, ignoring its poor linearity for the moment.

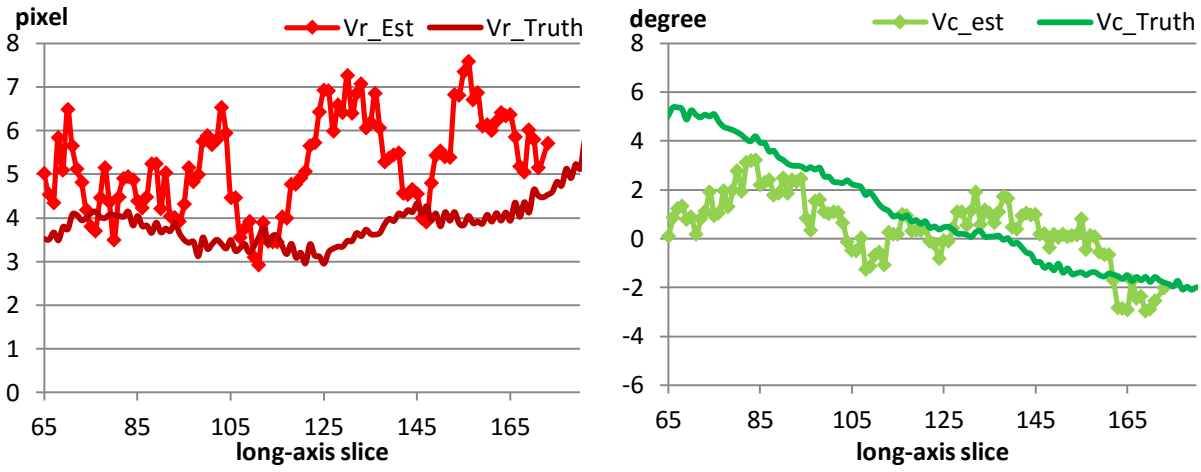

Figure 3-62 Radial (left) and circumferential (right) motion of PIS from frame 1 to 2 extracted from 3.0mm simulation data at noise level 2N. The true radial and circumferential motion are shown by darker red and darker green curves respectively.

The following figures show the results in three representatively SA slices of frame 1for 3.0mm resolution simulation data at noise level 2N. Figure 3-63 shows that at the basal SA slice, the S-constraint + S-initial method performed exceedingly well among all the methods. The 0-intial, S-initial, and even the T-initial have difficulty detecting accurate circumferential motion at the anterior and posterior region, while the S-constraint + S-initial method provides motion vectors very close to the truth. At the non-rotating SA slice shown in Figure 3-64, the difference among four methods is negligible, except that the S-constraint + S-initial method yields overestimated radial motion at the septal region, due to overestimation of the radial motion of the PIS. In Figure 3-65, all of the four methods underestimated the circumferential motion, while

the S-constraint + S-initial method provides slightly better detection of the circumferential motion than other three methods.

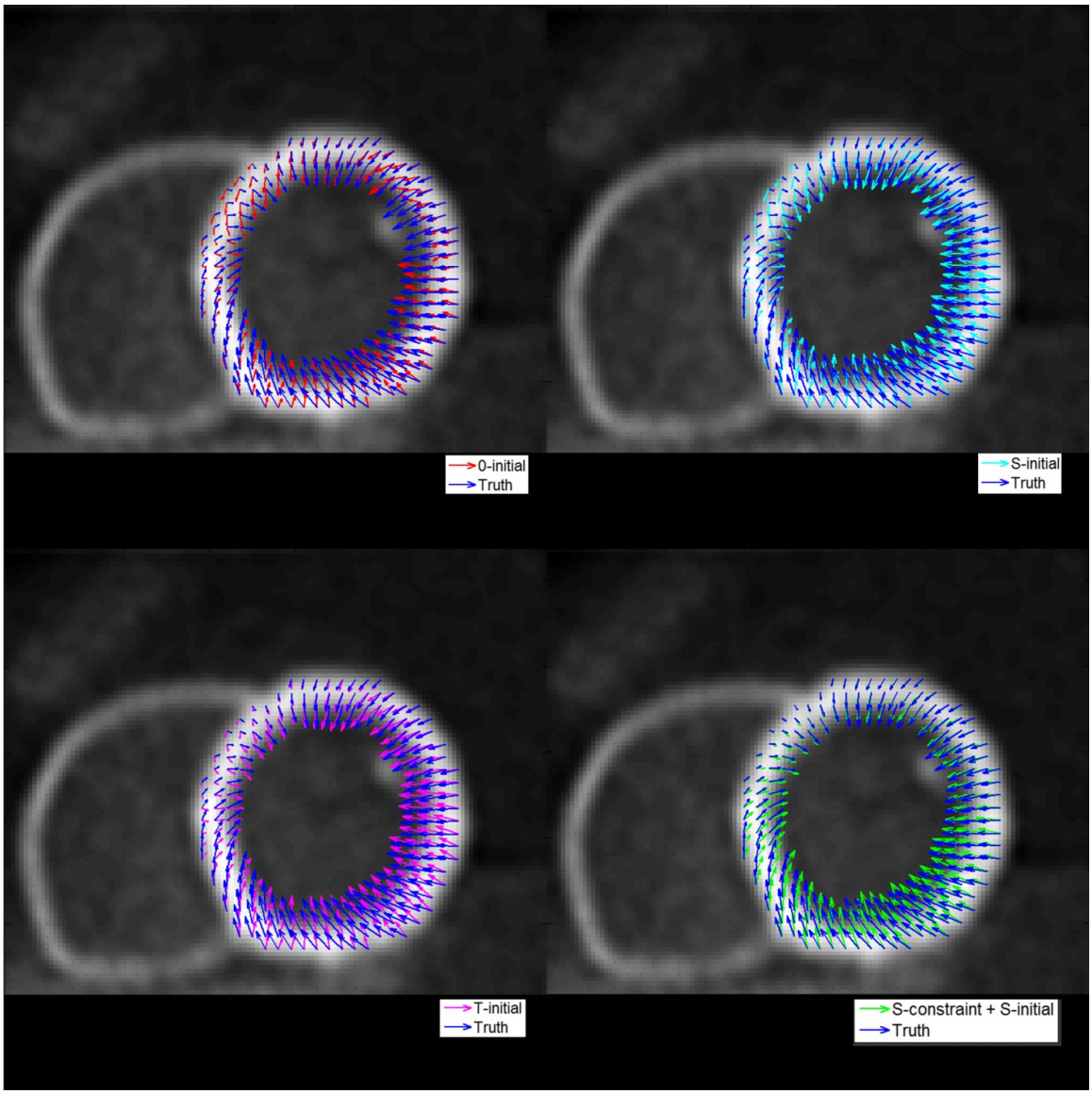

Figure 3-63 Cardiac motion estimation results using four methods for 3.0 mm resolution noise-level 2N simulation data of frame 1 at a basal SA slice. The true MVF is plotted in blue arrows for comparison.

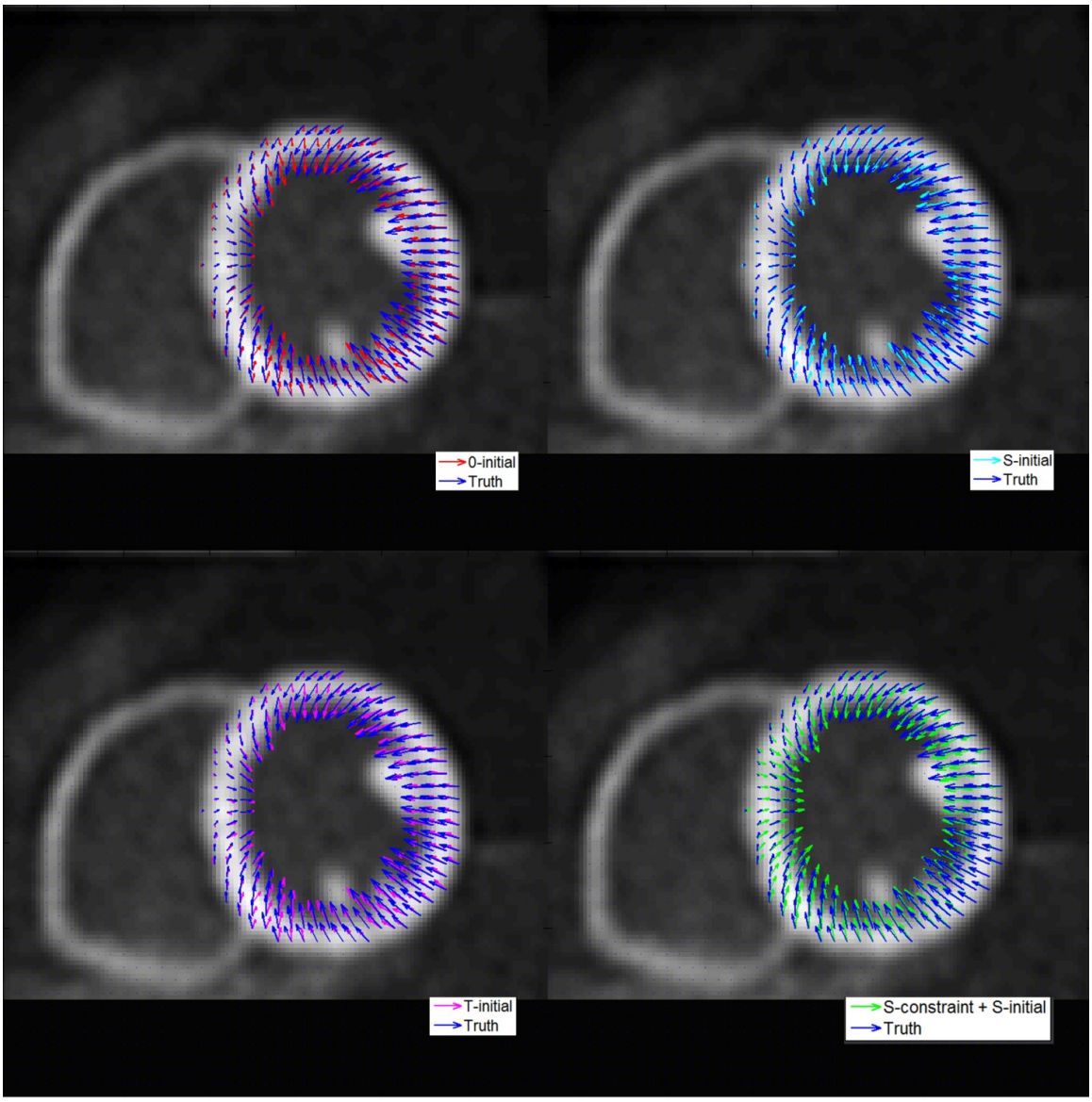

Figure 3-64 Cardiac motion estimation results using four methods for 3.0 mm resolution noise- level 2N simulation data of frame 1 at the non-twisting SA slice. The true MVF is plotted in blue arrows for comparison.

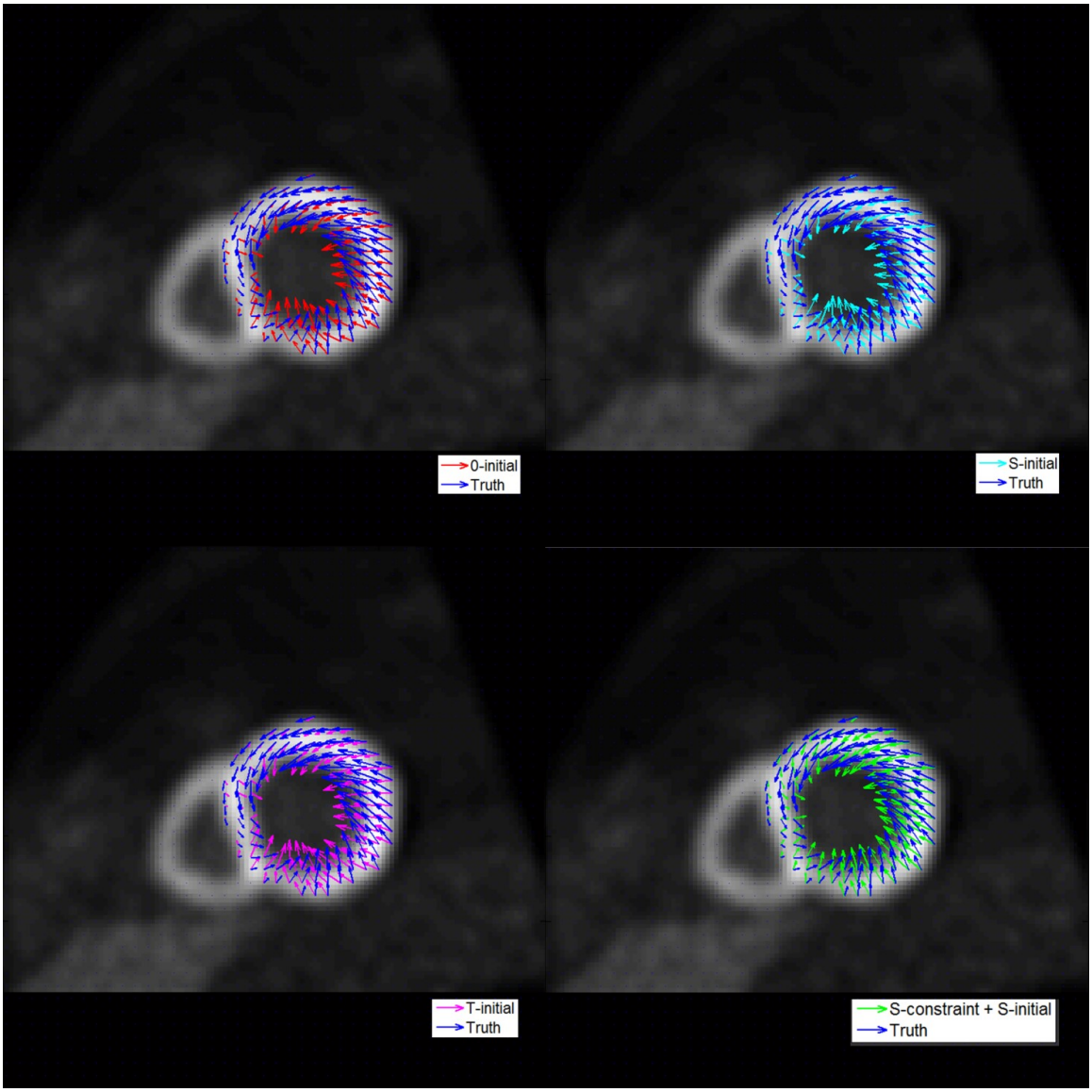

Figure 3-65 Cardiac motion estimation results using four methods for 3.0 mm resolution noise- level 2N simulation data of frame 1 at the sample apical SA slice. The true MVF is plotted in blue arrows for comparison.

Although the circumferential motion and radial motion of the sulcus are less accurate at noise level 2N than at noise-free case, the S-constraint + S-initial method performs better than all the other methods globally except for the radial motion as shown in Table 3-14. Table 3-15 shows quantitative evaluation of motion estimation accuracy for the three slices in frame 1 of this dataset, indicating that the S-constraint + S-initial method yields more accurate estimation of both circumferential and longitudinal motion than other methods in all three slices.

Table 3-14 Global error RMSE for three cardiac motion components in frame 1 for 3.0 mm resolution simulation data at noise level 2N

	Average amplitude		0-initial	S-initial	T-initial	S-constraint + S-initial
Vr(mm)	3.33	RMSE_Vr(mm)	0.96	1.23	0.68	1.40
Vc(degree)	3.80	RMSE_Vc(degree)	6.11	5.55	5.87	4.60
Vl(mm)	3.77	RMSE_Vl(mm)	2.65	1.79	1.23	0.95
MVF(mm)	5.94	RMSE_MVF(mm)	3.27	2.81	2.11	2.03

Table 3-15 Motion estimation error of four methods at three SA slices for 3.0 mm resolution noise-level 2N simulation data of frame 1

Apical SA slice						
			0-initial	S-initial	T-initial	S-constraint + S-initial
Vr(mm)	2.25	RMSE_Vr(mm)	0.66	0.62	0.66	1.29
Vc(degree)	7.95	RMSE_Vc(degree)	8.66	8.53	8.47	5.49
Vl(mm)	1.01	RMSE_Vl(mm)	1.15	1.08	0.92	1.10
MVF(mm)	4.10	RMSE_MVF(mm)	2.86	2.77	2.68	2.31
Non-rotating SA slice						
			0-initial	S-initial	T-initial	S-constraint + S-initial
Vr(mm)	3.89	RMSE_Vr(mm)	0.72	0.70	0.69	1.42
Vc(degree)	0.88	RMSE_Vc(degree)	1.72	1.76	1.78	1.44
Vl(mm)	4.84	RMSE_Vl(mm)	2.64	1.93	1.28	0.91
MVF(mm)	6.69	RMSE_MVF(mm)	2.87	2.22	1.69	1.85
Basal SA slice						

			0-initial	S-initial	T-initial	S-constraint + S-initial
Vr(mm)	4.03	RMSE_Vr(mm)	1.24	0.73	0.70	1.45
Vc(degree)	2.82	RMSE_Vc(degree)	4.20	4.27	3.69	1.34
Vl(mm)	6.64	RMSE_Vl(mm)	4.74	2.65	1.60	0.79
MVF(mm)	8.34	RMSE_MVF(mm)	5.34	3.51	2.57	1.78

The results of 3.0mm resolution at noise-free and noise level 2N in the global error of circumferential motion shown in Table 3-9 and Table 3-14 raise an important question: why the method performs better in the noisier case than in the noise-free case? To answer this question, we need to take a closer look at the estimated circumferential motion curve at these two noise levels. The equation of the linear regression line of the circumferential motion for noise-free data is $y = -0.0401\,x + 4.5287$ with $R^2 = 0.8585$, while that for noise level 2N is $y = -0.0292\,x + 3.9137$ with $R^2 = 0.4380$. The estimated circumferential motion at two noise levels and their linear regression lines are shown in Figure 3-66. Although at noise level 2N, the slope of the fitted line is smaller than that in noise-free data, the position of the zero-twisting plane matches well with the truth. On the other hand, the line for noise-free data yields circumferential motion in the opposite direction for long-axis slice from #108 to #135. As a result, the final estimation of the circumferential motion for the myocardium on these slices severely deviate from the truth, and the direction is wrong.

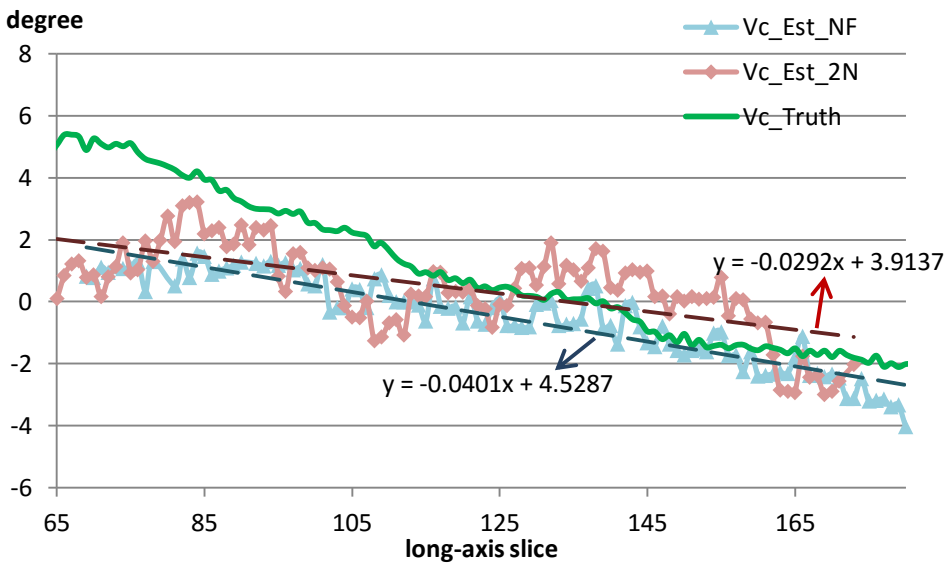

Figure 3-66 Circumferential motion of PIS from frame 1 to frame 2 calculated from 3.0mm resolution simulation data at noise-free (NF) and noise level 2N. The true circumferential motion is shown in green as reference. The linear regression line for the circumferential motion estimated at NF is shown in dark blue and that for noise level 2N is shown in dark red.

Motion estimation accuracy for the three sample SA slices in frame 1 of 3.0mm resolution noise-free simulation data is shown in Table 3-16, which confirms our explanation. Although the S-constraint + S-initial method achieves improved estimation of circumferential motion apical and basal SA slice, which is comparable as the value in Table 3-15, its error in circumferential motion at the non-rotating SA slice is significantly larger than other methods. Since the global error in circumferential motion is the summation of the error in all the voxels of myocardium, its value for noise-free data is larger than that for noise level 2N.

Table 3-16 Motion estimation error of four methods at three SA slices for 3.0 mm resolution noise-free simulation data of frame 1

Apical SA slice						
			0-initial	S-initial	T-initial	S-constraint + S-initial
Vr(mm)	2.25	RMSE_Vr(mm)	0.70	0.62	0.65	1.77
Vc(degree)	7.95	RMSE_Vc(degree)	8.54	8.67	8.64	5.66

Vl(mm)	1.01	RMSE_Vl(mm)	1.21	1.04	0.85	1.11
MVF(mm)	4.10	RMSE_MVF(mm)	2.90	2.83	2.74	2.63
Non-rotating SA slice						
			0-initial	S-initial	T-initial	S-constraint + S-initial
Vr(mm)	3.89	RMSE_Vr(mm)	0.95	0.57	0.59	2.02
Vc(degree)	0.88	RMSE_Vc(degree)	1.43	1.52	1.53	2.53
Vl(mm)	4.84	RMSE_Vl(mm)	3.13	2.33	1.38	0.97
MVF(mm)	6.69	RMSE_MVF(mm)	3.35	2.51	1.66	2.56
Basal SA slice						
			0-initial	S-initial	T-initial	S-constraint + S-initial
Vr(mm)	4.03	RMSE_Vr(mm)	1.07	0.81	0.64	1.98
Vc(degree)	2.82	RMSE_Vc(degree)	3.86	3.73	3.40	1.14
Vl(mm)	6.64	RMSE_Vl(mm)	5.99	3.49	1.53	1.01
MVF(mm)	8.34	RMSE_MVF(mm)	6.38	4.06	2.40	2.32

Our method is able to extract the motion of PIS at lower count level for 3.0mm resolution, or even 4.5mm resolution. However, the curves of both radial and circumferential motion become much noisier, and the linearity of the circumferential motion curve is further reduced as indicated by lower R^2 value. As a result, the performance of S-constraint + S-initial method is better than other methods for slices in which the estimated motion of the PIS is closer to the truth, and worse for slices with inaccurate PIS motion. The global error depends on how many slices are estimated accurately.

At higher noise level, the fitted line of the circumferential motion curve becomes less reliable, although it is possible that it is closer to the truth for some slices as shown in the example above. It is not guaranteed that

lower noise level will generate more accurate cardiac motion estimation result for circumferential motion due to the randomness of the image noise and its influence on the feature extraction.

DISCUSSION

Recalling Figure 3-28 and Figure 3-29, we can obtain the following information: The IS is located at the epicardium, which does not contract as much as the endocardium. For most long-axis slices, the radial motion of the sulcus point is under 4 pixels with 0.6mm pixel size. The error of sulcus location extraction can be as large as 2 pixels. Since the motion is calculated based on extracted sulcus location from two cardiac images, its error is the summation of the feature extraction error of two points. This explains why radial motion can be overestimated by two pixels even when the feature extraction error for one sulcus point is no larger than 1 pixel in phantom images.

As Figure 3-67 shows, the radius of the epicardium at sulcus point increases from the apical region to the base. According to Figure 3-28, the circumferential motion changes linearly from 5 degree at apical side to -3 degree at base on the epicardium. The motion of the sulcus in the direction tangential to the boundary of the epicardium on each short-axis lice is calculated using

$$V_{tangential} = \frac{V_c}{180^\circ}\pi R, \quad \text{3-18}$$

where R is the radius of epicardium at the sulcus point shown in Figure 3-67. The results are shown in Figure 3-68. The largest motion for the sulcus in tangential direction is only 4 pixels with pixel size 0.6mm; while for most slices, this value is under 3 pixels. With sulcus extraction error for each frame of cardiac image as large as 2 pixels at low system resolution, the estimation of the circumferential motion can become very inaccurate. Moreover, the circumferential motion of every point on the sulcus is required to find out the slope and intercept of the linear regression of circumferential motion for MVF initialization and feature based constraint. The accumulation of error will eventually lead the cardiac motion estimation to the wrong direction.

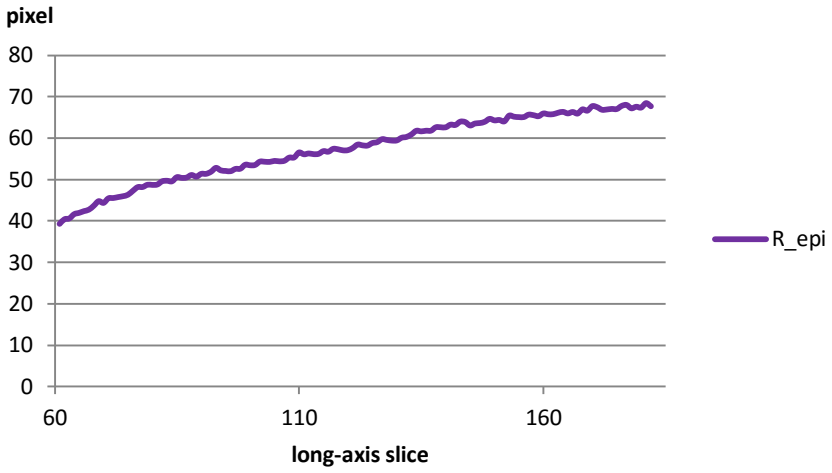

Figure 3-67 Radius of the epicardium at the sulcus points in frame 1

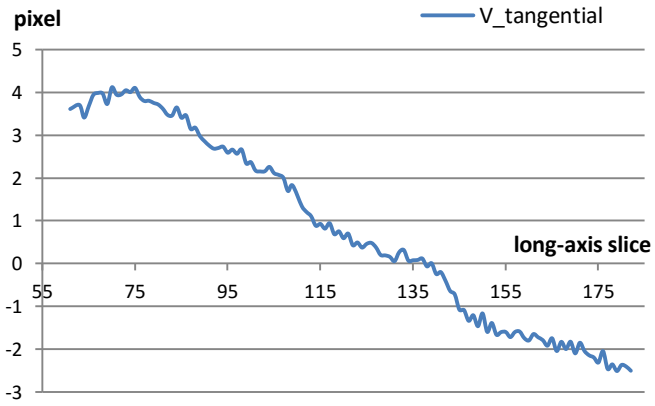

Figure 3-68 Tangential motion of the sulcus points in frame 1

For this method to achieve desirable improvement of cardiac motion estimation accuracy, the three motion components of the sulcus have to be accurate. This requires very high-resolution and finely-pixelated cardiac PET images. In addition, the cardiac motion between two frames has to be large enough; otherwise, the method will not make a difference and the error in feature extraction can overpower the true motion of the feature. Moreover, as shown in the previous sections, high image resolution is more important than high statistics, as the motion of the feature is very small compared to the pixel size.

Assuming the feature extraction is accurate, the proposed feature-guided cardiac motion estimation method performs very well even for low-resolution low-count images. We used the true motion of the PIS to create 'S-initial' and the 'S-constraint', then applied them to the simulated cardiac PET images of 4.5mm system

resolution at noise level 0.5N. Table 3-17 shows the motion estimation error in three motion components as well as the whole motion vector. The true average amplitude of three components and the MVF is also shown for reference. Since the true motion of the PIS is used, the 'S-initial' alone achieves comparable estimation accuracy as the T-initial, while the feature-based method 'S-constrain + S-initial' obtains the lowest error in all three motion components.

Table 3-17 Global error RMSE for three cardiac motion components in frame 1 for 4.5 mm resolution simulation data at noise level 0.5N

	Average amplitude		0-initial	'S-initial'	T-initial	'S-constraint + S-initial'
Vr(mm)	3.33	RMSE_Vr(mm)	1.46	1.23	1.19	0.81
Vc(degree)	3.80	RMSE_Vc(degree)	5.84	5.55	5.78	3.17
Vl(mm)	3.77	RMSE_Vl(mm)	2.32	1.79	1.62	0.88
MVF(mm)	5.94	RMSE_MVF(mm)	3.24	2.81	2.67	1.38

The motion estimation results of four methods for this data set were plotted in the following figures. With accurate sulcus motion, the S-constraint + S-initial method performs superior than all other methods including the T-initial. The estimated MVF shown by green arrows in all three sample slices matches very well with the truth. Specifically, in slices with significant circumferential motion such as the basal and the apical SA slice, the S-constraint + S-initial method achieves accurate estimation of the twisting motion, which is missed even by the T-initial.

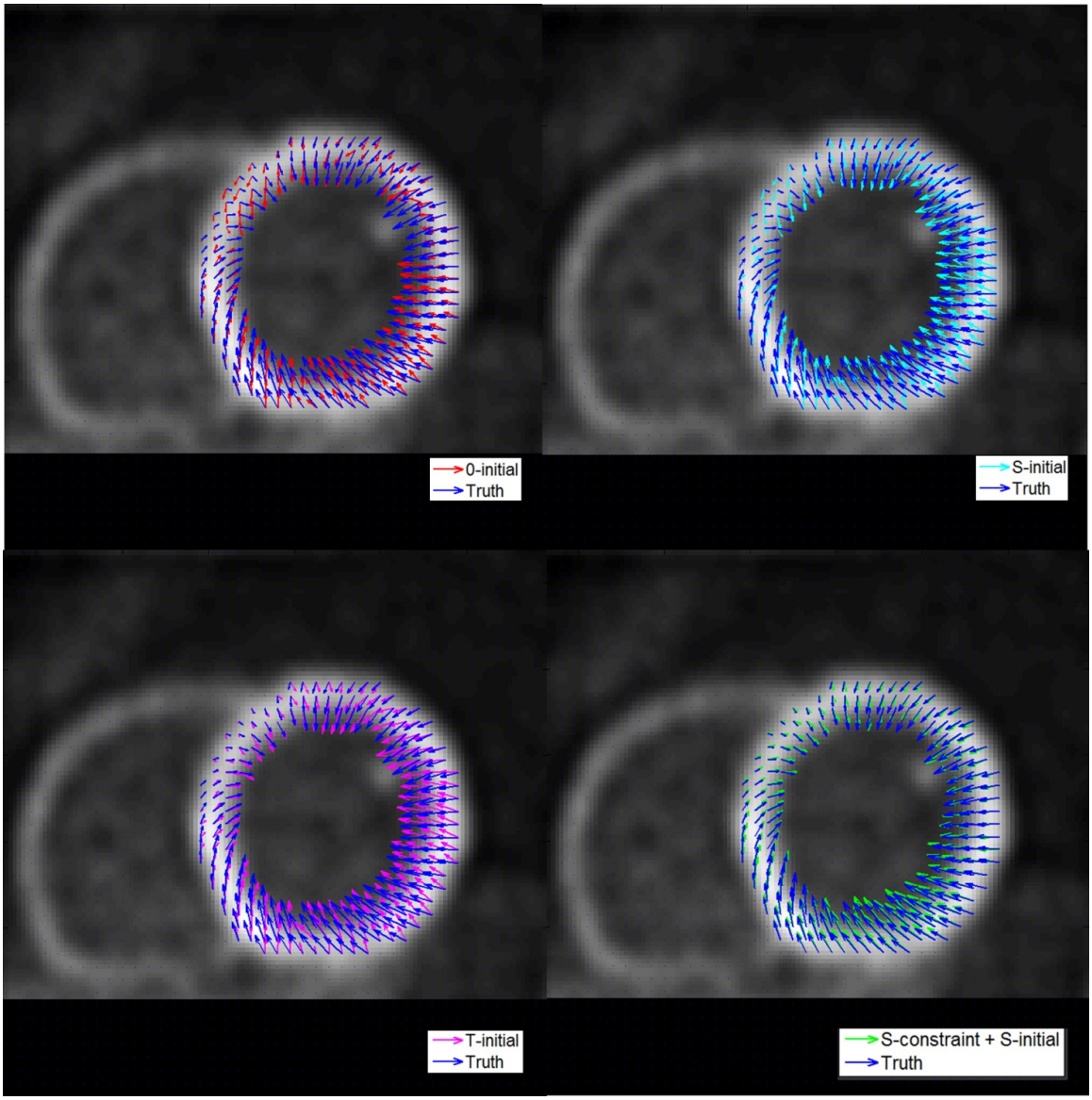

Figure 3-69 Cardiac motion estimation results at a basal SA slice using four methods for 4.5 mm resolution simulation data of frame 1at noise level 0.5N. The true MVF is plotted in blue arrows for comparison.

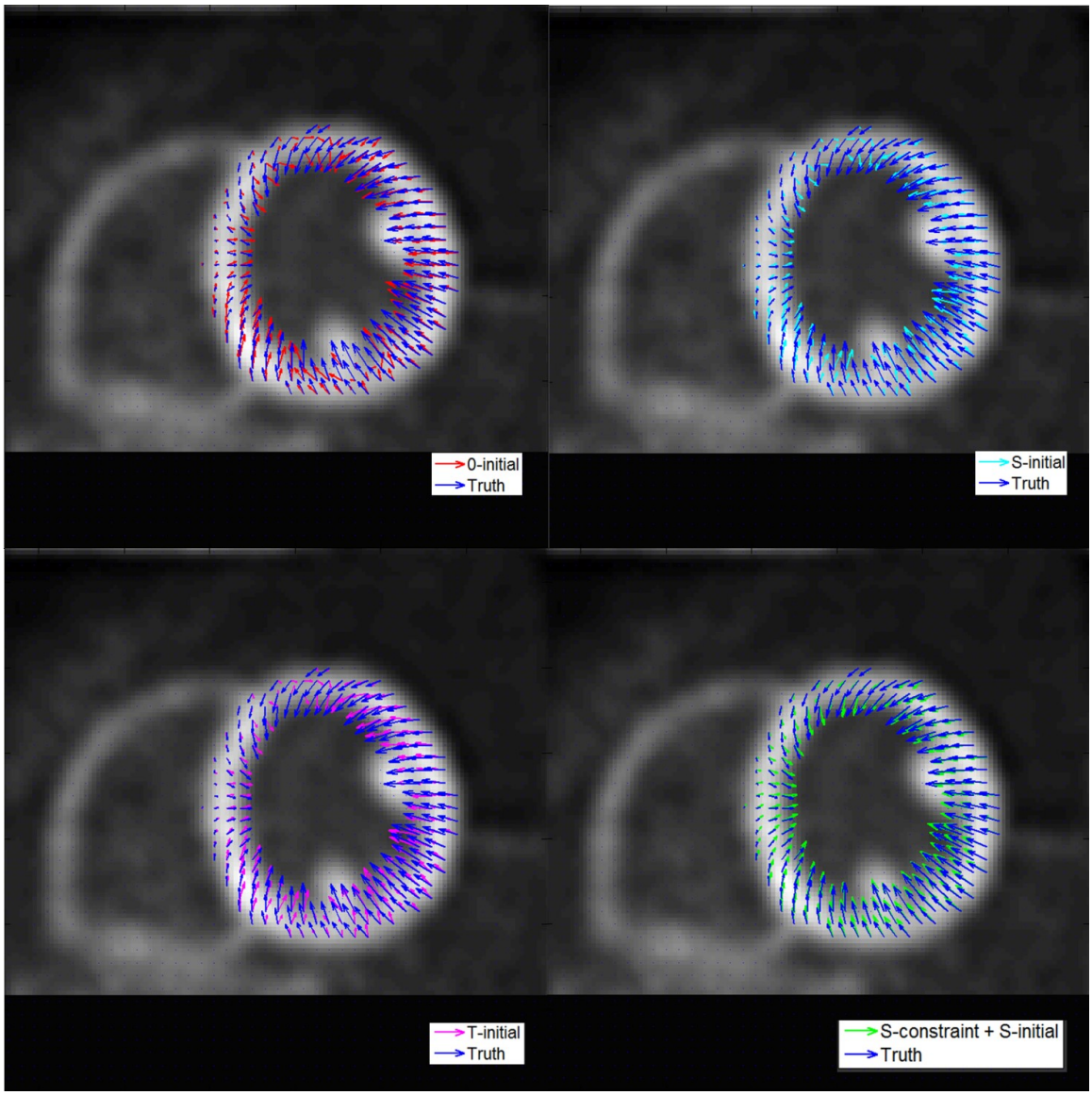

Figure 3-70 Cardiac motion estimation results at the non-rotating SA slice using four methods for 4.5 mm resolution simulation data of frame 1at noise level 0.5N. The true MVF is plotted in blue arrows for comparison.

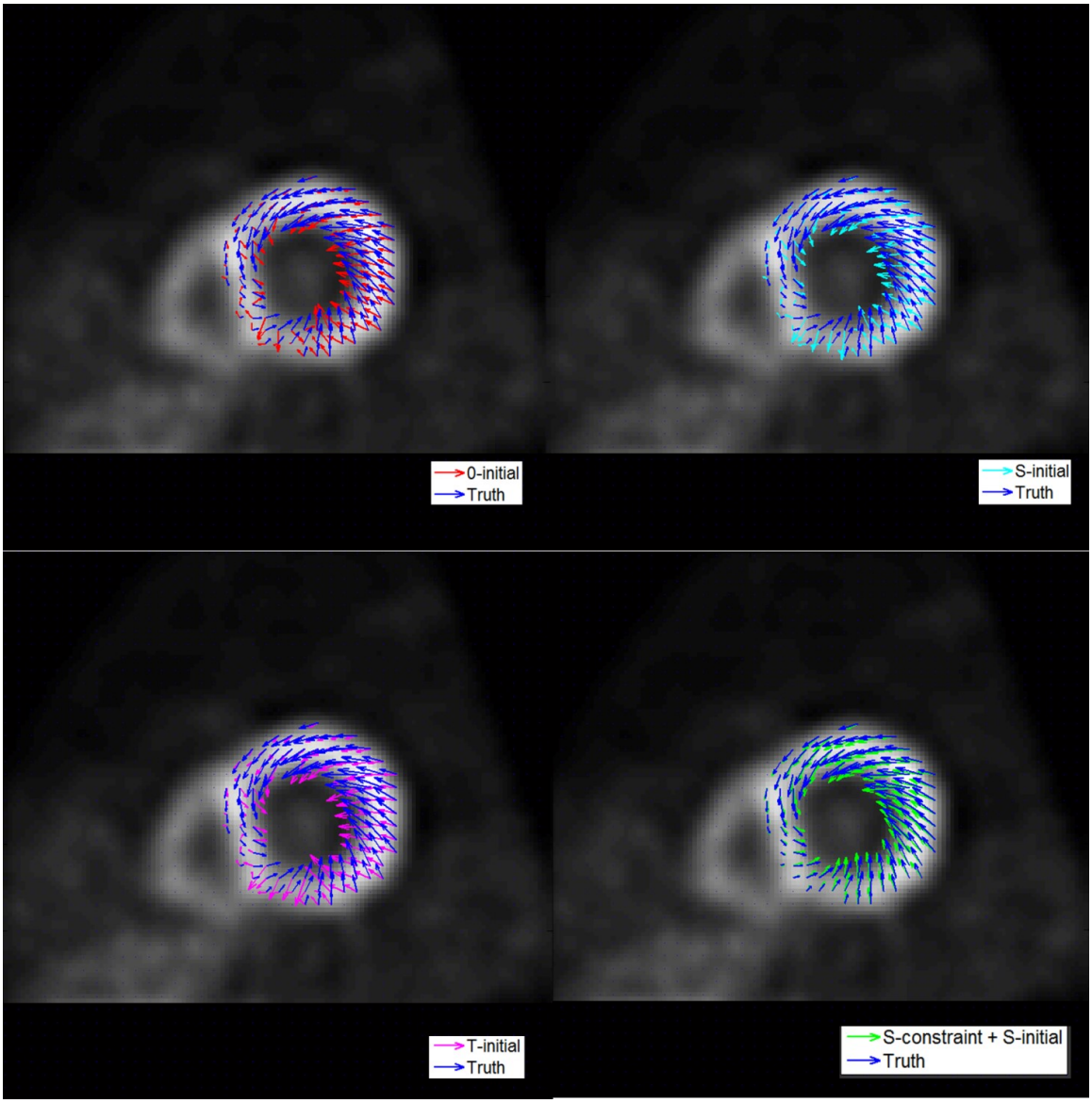

Figure 3-71 Cardiac motion estimation results at an apical SA slice using four methods for 4.5 mm resolution simulation data of frame 1at noise level 0.5N. The true MVF is plotted in blue arrows for comparison.

As for the parameters in the feature-based motion estimation algorithm, we used $\sigma = 15\ pixel$ and $\beta = 8$ for all simulation data, assuming that the motion estimate from the feature is reliable. Lowering σ and β will make the cost function more similar to that of the traditional optical-flow, and the error in motion estimation results will be larger for the simulation data assuming the motion of feature is accurate.

CONCLUSION

In this project, we proposed the idea of using anatomical features of the human heart to improve the accuracy of cardiac motion estimation for PET images. The features include the papillary muscle and the interventricular sulcus. In preliminary studies, initial estimate of the cardiac MVF was created based on the motion of the extracted features and the linear assumptions of cardiac motion model. The use of feature-based initial estimates (or initials), such as papillary muscle based initial and interventricular sulcus based initial, in combination with the conventional optical flow motion estimate algorithm, achieve more accurate cardiac MVF compared with 0-initial, by providing the optical-flow algorithm a starting motion estimate closer to the truth. In further improvement study, we proposed more accurate sulcus extraction algorithm based on B-spline interpolation and extrapolation techniques. To reduce the effect of the classical aperture problem, we developed a new feature-based cardiac motion estimation algorithm with an additional feature motion constraint. The feature-based cardiac motion estimation method proves successful for simulated cardiac PET data of high system resolution and low noise level. The results from simulation data of different resolutions show that with the degradation of system resolution and increase of noise level in the acquired data, the extracted motion estimate of the sulcus becomes less accurate, which in turn results in decrease in motion estimation accuracy. Starting from 1.5mm resolution, the feature-based method with additional constraint is not able to reduce the global error in circumferential motion, but for the basal SA slices, the method still performs better than the traditional method. For 0.6mm system resolution, the method is consistently superior at all four simulated noise levels in terms of all three cardiac motion components. In addition, we also studied the inconsistency between the calculated motion of the papillary muscle footprint and the true motion of the centroid, concluding that this is the inherent property of human heart and that papillary muscle is not a reliable feature for cardiac motion estimation.

In addition to developing and verifying feature extraction and cardiac motion estimation methods, we studied the influence of resolution and noise on the extracted motion of the interventricular sulcus. We found that the errors in radial and circumferential motion deteriorate as the system resolution degrades and the noise level increases. We also analyzed cardiac motion estimation error in details. This is the first study that quantitatively investigates cardiac motion estimation in three components from cardiac gated 4D cardiac PET images. The three cardiac motion components are radial, circumferential and longitudinal motion. Among these three cardiac motion components, the radial motion is the easiest to estimate, as it is

perpendicular to the edge of myocardium. The circumferential and longitudinal components of the cardiac motion vector field are more difficult to detect using conventional optical-flow method. The error in longitudinal motion is the largest among all three components. Although the feature-based method does not improve the detection of circumferential motion in terms of global accuracy when the resolution degrades, the improvement in longitudinal motion estimate leads to a lower total error of the whole cardiac MVF. Meanwhile, we discovered that accurate estimation of the feature's motion is crucial for the feature-based cardiac motion estimation method to achieve better result than the traditional method. Therefore, high system resolution and low noise is necessary for the feature-based method to improve the cardiac motion estimation accuracy. Although currently 0.6mm and 1.5mm resolution is not realistic for current clinical PET scanners for routine cardiac PET imaging, 4.0mm resolution is already available and a commercial PET scanner with 2.5 mm resolution is entering the US market in the very near future. Experiment results from noisy simulated PET images with 3.0mm resolution indicate that the feature-based method is able to generate more accurate motion estimation result than traditional optical-flow algorithm.

CHAPTER 4. SUMMARY AND FUTURE WORK

In this Ph.D. dissertation research, we have investigated two main topics: (1) advanced data-driven respiratory gating methods from list-mode cardiac PET data, and (2) feature-based cardiac motion estimation method for cardiac-gated cardiac PET images. Both topics are aiming at improving the quality and clinical value of cardiac PET data.

Respiratory gating is a widely used approach to reduce the influence of respiratory motion in PET images. The PET data is divided into several frames according to the respiratory status of the patient. For cardiac PET data, respiratory motion compensation requires proper gating of the data. In chapter 2, we proposed a data-driven method to extract the respiratory motion signal directly from list-mode cardiac PET data by calculating the centroid of the heart from grouping the list-mode data in 200ms dynamic frames. When available, time-of-flight (TOF) PET information is used to identify photons from a volume-of-interest (VOI) that encompassed the heart for more accurate determination of the centroid location of the heart. Moreover, a simple background correction method was also proposed to remove the background counts in the centroid location sequence, leading to an increase in the SNR of frequency spectrum of the centroid location signal.. The methods were applied to and evaluated using clinical cardiac PET data, and the results show that with TOF information and background correction, the SNR and respiratory motion amplitude of the respiratory signal is improved.

With improved image quality in terms of resolution and noise level by means of advance in hardware and motion compensation process, cardiac motion estimation becomes more and more reliable in PET imaging. In Chapter 3, we proposed feature-based cardiac motion estimation method to improve the accuracy of estimated cardiac MVF. In our preliminary studies, the motions of the papillary muscles and the interventricular sulcus was used to create initial estimation of cardiac MVF based on a linear cardiac motion model. In simulation data with eight cardiac-gated frames, the feature-based initials were shown to allow more accurate motion estimation results than the 0-intial. The idea was further developed and improved in the second half of Chapter 3. An interventricular sulcus extraction method based on B-spline interpolation and extrapolation methods was proposed to improve the accuracy of feature extraction. More importantly, a sulcus-based constraint was added to the feature-based extraction algorithm to further reduce the effect of

the aperture problem. The method was tested using simulated PET data of various resolutions and noise levels. The results show that with gated cardiac PET images with higher resolution and lower image noise, the extracted sulcus motion become more accurate, leading to more accurate estimate of the cardiac motion as compared to that using traditional methods, especially for motion parallel to the edges. It is also found that the accuracy of feature extraction is still the bottleneck of the feature-based motion estimation method. Our study demonstrated the first method using anatomical features in cardiac motion estimation. In addition, it is the first study that analyzes and evaluates cardiac motion estimation result in three motion components. We also believe that cardiac motion component analysis is useful in detection and evaluation of cardiac motion abnormalities.

There are two parameters to adjust in the feature-based motion estimation algorithm: the weight factor and the effective range of the motion constraint term. In our preliminary study, the values for the two parameters were chosen empirically. Optimization of these parameters will potentially provide further improvement of the cardiac motion estimation methods and is a topic for future exploration.

The features that can be employed in cardiac motion estimation are not limited to the anatomical structures used in this study. Tagged MR techniques which are regarded as the gold standard in cardiac motion imaging also provide detailed information about the cardiac motion as shown in Figure 4-1. Since it is very difficult and time-consuming to acquire 3D volume tagged MR images of the heart for the whole cardiac cycle, the common practice is to get 2 or 3 slices of 2D tagged images of the heart. The motion information contained in the sparsely sampled slices of co-registered tagged MR images can also be used to help 3D cardiac motion estimation for cardiac PET data.

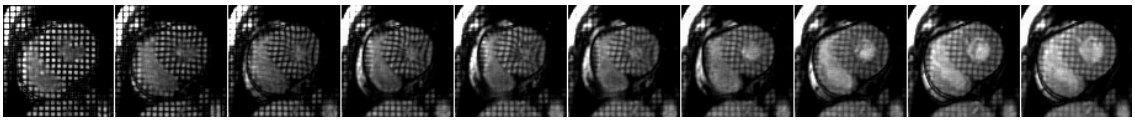

Figure 4-1 Tagged MR images of a short-axis slice of a patient's heart

Moreover, it is possible to integrate the cardiac motion model with three motion components, and even the muscle fiber mechanics in the myocardium, into the cardiac motion estimation algorithm. This requires more comprehensive understanding and knowledge about cardiac motion, which requires intensive clinical study. In this way, the estimated cardiac motion will become more biologically meaningful.

Another future extension of feature-based cardiac motion estimation is to investigate the influence of motion defects on feature extraction and motion estimation results. The cardiac motion model used in the simulation study is developed based on clinical cardiac-gated tagged MRI data of a normal patient. There are questions regarding to models of abnormal cardiac motion. For example, with regional or global motion defects, would the linear assumption about three cardiac motion components still stand? And if not, how would inaccurate cardiac motion model influence the motion estimation results.

Although currently cardiac PET images still have poor image resolution and high noise, their quality has been improving in recent years. With its ability of providing functional information of the myocardium, the additional cardiac motion information that can be extracted from the same list-mode datasets will provide additional information that can aid in clinical diagnosis without additional study and cost will have significant positive impact in patient care and health care cost.

REFERENCE

1. Levin, C.S. and E.J. Hoffman, *Calculation of positron range and its effect on the fundamental limit of positron emission tomography system spatial resolution.* Physics in Medicine and Biology, 1999. **44**(3): p. 781-799.
2. Hammer, B.E., N.L. Christensen, and B.G. Heil, *Use of a Magnetic-Field to Increase the Spatial-Resolution Positron Emission Tomography.* Medical Physics, 1994. **21**(12): p. 1917-1920.
3. Reader, A.J., et al., *One-pass list-mode EM algorithm for high-resolution 3-D PET image reconstruction into large arrays.* Ieee Transactions on Nuclear Science, 2002. **49**(3): p. 693-699.
4. Rafecas, M., et al., *Effect of noise in the probability matrix used for statistical reconstruction of PET data.* Ieee Transactions on Nuclear Science, 2004. **51**(1): p. 149-156.
5. Shibuya, K., et al., *Limit of Spatial Resolution in FDG-PET due to Annihilation Photon Non-Collinearity.* World Congress on Medical Physics and Biomedical Engineering 2006, Vol 14, Pts 1-6, 2007. **14**: p. 1667-1671.
6. Siegel, S. and M. Dahlbom, *Implementation and Evaluation of a Calculated Attenuation Correction for Pet.* Ieee Transactions on Nuclear Science, 1992. **39**(4): p. 1117-1121.
7. Kinahan, P.E., et al., *Attenuation correction for a combined 3D PET/CT scanner.* Medical Physics, 1998. **25**(10): p. 2046-2053.
8. Martinez-Moller, A., et al., *Tissue Classification as a Potential Approach for Attenuation Correction in Whole-Body PET/MRI: Evaluation with PET/CT Data.* Journal of Nuclear Medicine, 2009. **50**(4): p. 520-526.
9. Hofmann, M., et al., *MRI-Based Attenuation Correction for PET/MRI: A Novel Approach Combining Pattern Recognition and Atlas Registration.* Journal of Nuclear Medicine, 2008. **49**(11): p. 1875-1883.
10. Brasse, D., et al., *Correction methods for random coincidences in fully 3D whole-body PET: Impact on data and image quality.* Journal of Nuclear Medicine, 2005. **46**(5): p. 859-867.
11. Ollinger, J.M., *Model-based scatter correction for fully 3D PET.* Physics in Medicine and Biology, 1996. **41**(1): p. 153-176.
12. Stearns, C.W., *Scatter correction method for 3D PET using 2D fitted Gaussian functions.* Journal of Nuclear Medicine, 1995. **36**(5): p. 105.
13. Bailey, D.L. and S.R. Meikle, *A Convolution-Subtraction Scatter Correction Method for 3d Pet.* Physics in Medicine and Biology, 1994. **39**(3): p. 411-424.
14. Levin, C.S., M. Dahlbom, and E.J. Hoffman, *A Monte-Carlo Correction for the Effect of Compton-Scattering in 3-D Pet Brain Imaging.* Ieee Transactions on Nuclear Science, 1995. **42**(4): p. 1181-1185.
15. Shao, L.X., R. Freifelder, and J.S. Karp, *Triple Energy Window Scatter Correction Technique in Pet.* Ieee Transactions on Medical Imaging, 1994. **13**(4): p. 641-648.

16. Cherry, S.R., S.R. Meikle, and E.J. Hoffman, *Correction and Characterization of Scattered Events in 3-Dimensional Pet Using Scanners with Retractable Septa.* Journal of Nuclear Medicine, 1993. **34**(4): p. 671-678.
17. Watson, C.C., *New, faster, image-based scatter correction for 3D PET.* Ieee Transactions on Nuclear Science, 2000. **47**(4): p. 1587-1594.
18. Kolbitsch, C., et al., *A 3D MR-acquisition scheme for nonrigid bulk motion correction in simultaneous PET-MR.* Medical Physics, 2014. **41**(8): p. 490-503.
19. Gordon, R., R. Bender, and G.T. Herman, *Algebraic Reconstruction Techniques (Art) for 3-Dimensional Electron Microscopy and X-Ray Photography.* Journal of Theoretical Biology, 1970. **29**(3): p. 471-&.
20. Xu, X.L., J.S. Liow, and S.C. Strother, *Iterative Algebraic Reconstruction Algorithms for Emission Computed-Tomography - a Unified Framework and Its Application to Positron Emission Tomography.* Medical Physics, 1993. **20**(6): p. 1675-1684.
21. Shepp, L.A. and Y. Vardi, *Maximum likelihood reconstruction for emission tomography.* IEEE Trans Med Imaging, 1982. **1**(2): p. 113-22.
22. Lange, K. and R. Carson, *Em Reconstruction Algorithms for Emission and Transmission Tomography.* Journal of Computer Assisted Tomography, 1984. **8**(2): p. 306-316.
23. Hudson, H.M. and R.S. Larkin, *Accelerated Image-Reconstruction Using Ordered Subsets of Projection Data.* Ieee Transactions on Medical Imaging, 1994. **13**(4): p. 601-609.
24. Reader, A.J., et al., *Accelerated list-mode EM algorithm.* Ieee Transactions on Nuclear Science, 2002. **49**(1): p. 42-49.
25. Reader, A.J., et al., *Regularized one-pass list-mode EM algorithm for high resolution 3D PET image reconstruction into large arrays.* 2001 Ieee Nuclear Science Symposium, Conference Records, Vols 1-4, 2002: p. 1853-1858.
26. Nuyts, J., et al., *Simultaneous maximum a-posteriori reconstruction of attenuation and activity distributions from emission sinograms.* IEEE Trans Med Imaging, 1999. **18**(5): p. 393-403.
27. Rezaei, A., et al., *Simultaneous Reconstruction of Activity and Attenuation in Time-of-Flight PET.* Ieee Transactions on Medical Imaging, 2012. **31**(12): p. 2224-2233.
28. Defrise, M., A. Rezaei, and J. Nuyts, *Time-of-flight PET data determine the attenuation sinogram up to a constant.* Physics in Medicine and Biology, 2012. **57**(4): p. 885-899.
29. Schindler, T.H., et al., *Cardiac PET Imaging for the Detection and Monitoring of Coronary Artery Disease and Microvascular Health.* Jacc-Cardiovascular Imaging, 2010. **3**(6): p. 623-640.
30. Schwaiger, M., *Myocardial Perfusion Imaging with Pet.* Journal of Nuclear Medicine, 1994. **35**(4): p. 693-698.
31. Di Carli, M.F., et al., *Clinical myocardial perfusion PET/CT.* Journal of Nuclear Medicine, 2007. **48**(5): p. 783-793.

32. Petibon, Y., et al., *Towards coronary plaque imaging using simultaneous PET-MR: a simulation study.* Physics in Medicine and Biology, 2014. **59**(5).
33. Medina, R., et al., *The Value of Echocardiographic Regional Wall Motion Abnormalities in Detecting Coronary-Artery Disease in Patients with or without a Dilated Left-Ventricle.* American Heart Journal, 1985. **109**(4): p. 799-803.
34. Ghosh, N., et al., *Assessment of myocardial ischaemia and viability: role of positron emission tomography.* European Heart Journal, 2010. **31**(24): p. 2984-2995.
35. Okumura, W., et al., *Usefulness of fasting F-18-FDG PET in identification of cardiac sarcoidosis.* Journal of Nuclear Medicine, 2004. **45**(12): p. 1989-1998.
36. Fukushima, K., et al., *Molecular Hybrid Positron Emission Tomography/Computed Tomography Imaging of Cardiac Angiotensin II Type 1 Receptors.* Journal of the American College of Cardiology, 2012. **60**(24): p. 2527-2534.
37. Delso, G., et al., *Performance Measurements of the Siemens mMR Integrated Whole-Body PET/MR Scanner.* Journal of Nuclear Medicine, 2011. **52**(12): p. 1914-1922.
38. Nehrke, K., et al., *Free-breathing cardiac MR imaging: Study of implications of respiratory motion-initial results.* Radiology, 2001. **220**(3): p. 810-815.
39. Nehmeh, S.A., et al., *Deep-inspiration breath-hold PET/CT of the thorax.* Journal of Nuclear Medicine, 2007. **48**(1): p. 22-26.
40. Chen, S. and B.M. Tsui. *Accuracy analysis of image-based respiratory motion estimation and compensation in respiratory-gated PET reconstruction*. in *Nuclear Science Symposium Conference Record, 2008. NSS'08. IEEE*. 2008. IEEE.
41. Le Meunier, L., et al., *PET/CT imaging: Effect of respiratory motion on apparent myocardial uptake.* Journal of Nuclear Cardiology, 2006. **13**(6): p. 821-830.
42. Chen, S. and B.M.W. Tsui, *Accuracy Analysis of Image-based Respiratory Motion Estimation and Compensation in Respiratory-gated PET Reconstruction.* 2008 Ieee Nuclear Science Symposium and Medical Imaging Conference (2008 Nss/Mic), Vols 1-9, 2009: p. 3566-3569.
43. Klein, G.J., et al., *Real-time system for respiratory-cardiac gating in positron tomography.* Ieee Transactions on Nuclear Science, 1998. **45**(4): p. 2139-2143.
44. Nehmeh, S.A., et al., *Effect of respiratory gating on quantifying PET images of lung cancer.* J Nucl Med, 2002. **43**(7): p. 876-81.
45. Buther, F., et al., *List Mode-Driven Cardiac and Respiratory Gating in PET.* Journal of Nuclear Medicine, 2009. **50**(5): p. 674-681.
46. Feng, T. and B.M.W. Tsui, *Non-Rigid Respiratory Motion Correction for 4D Gated PET Sinogram Data.* 2013 Ieee Nuclear Science Symposium and Medical Imaging Conference (Nss/Mic), 2013.
47. Chun, S.Y., et al., *MRI-Based Nonrigid Motion Correction in Simultaneous PET/MRI.* Journal of Nuclear Medicine, 2012. **53**(8): p. 1284-1291.

48. Feng, T., et al., *Development and evaluation of two 4D image reconstruction methods with dual respiratory and cardiac motion compensation for gated myocardial perfusion PET.* IEEE Nuclear Science Symposium and Medical Imaging (NSS/MIC) Conference Record, 2014.
49. Li, X.A., C. Stepaniak, and E. Gore, *Technical and dosimetric aspects of respiratory gating using a pressure-sensor motion monitoring system.* Medical Physics, 2006. **33**(1): p. 145-154.
50. Boucher, L., et al., *Respiratory gating for 3-dimensional PET of the thorax: Feasibility and initial results.* Journal of Nuclear Medicine, 2004. **45**(2): p. 214-219.
51. McKibben, C.K. and N.V. Reo, *A piezoelectric respiratory monitor for in vivo NMR.* Magnetic Resonance in Medicine, 1992. **27**(2): p. 338-42.
52. Wang, Y., et al., *Navigator-echo-based real-time respiratory gating and triggering for reduction of respiration effects in three-dimensional coronary MR angiography.* Radiology, 1996. **198**(1): p. 55-60.
53. Dasari, P., et al., *MRI Investigation of the Linkage Between Respiratory Motion of the Heart and Markers on Patient's Abdomen and Chest: Implications for Respiratory Amplitude Binning List-Mode PET and SPECT Studies.* Ieee Transactions on Nuclear Science, 2014. **61**(1): p. 192-201.
54. Visvikis, D., et al., *A posteriori respiratory motion gating of dynamic PET images.* 2003 Ieee Nuclear Science Symposium, Conference Record, Vols 1-5, 2004: p. 3276-3280.
55. Schleyer, P.J., et al., *Retrospective data-driven respiratory gating for PET/CT.* Physics in Medicine and Biology, 2009. **54**(7): p. 1935-1950.
56. Bundschuh, R.A., et al., *Postacquisition detection of tumor motion in the lung and upper abdomen using list-mode PET data: A feasibility study.* Journal of Nuclear Medicine, 2007. **48**(5): p. 758-763.
57. Würslin, C., et al., *Respiratory motion correction in oncologic PET using T1-weighted MR imaging on a simultaneous whole-body PET/MR system.* Journal of Nuclear Medicine, 2013. **54**(3): p. 464-471.
58. Klein, G.J., B.W. Reutter, and R.H. Huesman, *Four-dimensional affine registration models for respiratory-gated PET.* Nuclear Science, IEEE Transactions on, 2001. **48**(3): p. 756-760.
59. Lamare, F., et al., *Respiratory motion correction for PET oncology applications using affine transformation of list mode data.* Physics in Medicine and Biology, 2007. **52**(1): p. 121.
60. Reyes, M., et al., *Model-based respiratory motion compensation for emission tomography image reconstruction.* Physics in Medicine and Biology, 2007. **52**(12): p. 3579-600.
61. PA, V.d.E., *Marker-guided registration of electomagnetic dipole data with tomographic images*, in *Information processing in medical imaging*, H.D. Colchester ACF, Editor 1991, Springer Verlag: Heidelburg. p. 142-153.
62. Fenlon, M.R., et al., *Locking acrylic resin dental stent for image-guided surgery.* Journal of Prosthetic Dentistry, 2000. **83**(4): p. 482-5.

63. West, J., et al., *Comparison and evaluation of retrospective intermodality brain image registration techniques.* J Comput Assist Tomogr, 1997. **21**(4): p. 554-66.
64. Bookstein, F.L. *Thin-plate splines and the atlas problem for biomedical images*. in *Information Processing in Medical Imaging*. 1991. Springer.
65. Pelizzari, C.A., et al., *Accurate three-dimensional registration of CT, PET, and/or MR images of the brain.* Journal of Computer Assisted Tomography, 1989. **13**(1): p. 20-26.
66. Besl, P.J. and N.D. McKay. *Method for registration of 3-D shapes*. in *Robotics-DL tentative*. 1992. International Society for Optics and Photonics.
67. Monga, O. and S. Benayoun, *Using partial derivatives of 3D images to extract typical surface features.* Computer vision and image understanding, 1995. **61**(2): p. 171-189.
68. Kybic, J. and M. Unser, *Fast parametric elastic image registration.* IEEE Trans Image Process, 2003. **12**(11): p. 1427-42.
69. Lemieux, L., et al., *Voxel‐based localization in frame‐based and frameless stereotaxy and its accuracy.* Medical Physics, 1994. **21**(8): p. 1301-1310.
70. Maes, F., et al., *Multimodality image registration by maximization of mutual information.* Medical Imaging, IEEE Transactions on, 1997. **16**(2): p. 187-198.
71. Rueckert, D., et al., *Nonrigid registration using free-form deformations: application to breast MR images.* Medical Imaging, IEEE Transactions on, 1999. **18**(8): p. 712-721.
72. Thevenaz, P. and M. Unser, *Optimization of mutual information for multiresolution image registration.* IEEE Trans Image Process, 2000. **9**(12): p. 2083-99.
73. Bai, W. and M. Brady, *Motion correction and attenuation correction for respiratory gated PET images.* IEEE Trans Med Imaging, 2011. **30**(2): p. 351-65.
74. Studholme, C., D.L. Hill, and D.J. Hawkes, *Automated three-dimensional registration of magnetic resonance and positron emission tomography brain images by multiresolution optimization of voxel similarity measures.* Medical Physics, 1997. **24**(1): p. 25-35.
75. Horn, B.K.P. and B.G. Schunck, *Determining Optical-Flow.* Artificial Intelligence, 1981. **17**(1-3): p. 185-203.
76. Song, S.M. and R.M. Leahy, *Computation of 3-D Velocity-Fields from 3-D Cine Ct Images of a Human Heart.* Ieee Transactions on Medical Imaging, 1991. **10**(3): p. 295-306.
77. Klein, G.J. and R.H. Huesman, *Elastic material model mismatch effects in deformable motion estimation.* Ieee Transactions on Nuclear Science, 2000. **47**(3): p. 1000-1005.
78. Klein, G.J. and R.H. Huesman, *Four-dimensional processing of deformable cardiac PET data.* Medical Image Analysis, 2002. **6**(1): p. 29-46.
79. Klein, G.J., et al., *Tracking cardiac twist in gated PET imagery.* 2001 Ieee Nuclear Science Symposium, Conference Records, Vols 1-4, 2002: p. 2040-2044.
80. Nichols, K., et al., *Detection of wall motion abnormalities by myocardial perfusion gated SPECT torque measurements.* Journal of Nuclear Medicine, 2001. **42**(5): p. 59p-59p.

81. Nichols, K., et al., *Feasibility of detecting cardiac torsion in myocardial perfusion gated SPECT data.* Journal of Nuclear Cardiology, 2002. **9**(5): p. 500-507.
82. Mair, B.A., D.R. Gilland, and J. Sun, *Estimation of images and nonrigid deformations in gated emission CT.* Ieee Transactions on Medical Imaging, 2006. **25**(9): p. 1130-1144.
83. Gilland, D.R., et al., *Simultaneous reconstruction and motion estimation for gated cardiac ECT.* Ieee Transactions on Nuclear Science, 2002. **49**(5): p. 2344-2349.
84. Cao, Z.X., et al., *Three-dimensional motion estimation with image reconstruction for gated cardiac ECT.* Ieee Transactions on Nuclear Science, 2003. **50**(3): p. 384-388.
85. Ter-Pogossian, M.M., et al., *Photon time-of-flight-assisted positron emission tomography.* J Comput Assist Tomogr, 1981. **5**(2): p. 227-39.
86. Defrise, M., V.Y. Panin, and M.E. Casey, *New Consistency Equation for Time-of-Flight PET.* Ieee Transactions on Nuclear Science, 2013. **60**(1): p. 124-133.
87. Brasse, D., et al., *Correction methods for random coincidences in fully 3D whole-body PET: impact on data and image quality.* J Nucl Med, 2005. **46**(5): p. 859-67.
88. Adams, R. and L. Bischof, *Seeded Region Growing.* IEEE transactions on pattern analysis and machine intelligence, 1994. **16**(6): p. 641-647.
89. Preparata, F.P. and M.I. Shamos, *Convex Hulls: Basic Algorithms*, in *Computational Geometry: An Introduction*1985, Springer New York: New York, NY. p. 95-149.
90. Palmes, P.P., et al., *Myocardial longitudinal motion by tissue velocity imaging in the evaluation of patients with myocardial infarction.* Journal of the American Society of Echocardiography, 2000. **13**(9): p. 818-826.
91. Buchalter, M.B., et al., *Noninvasive Quantification of Left-Ventricular Rotational Deformation in Normal Humans Using Magnetic-Resonance-Imaging Myocardial Tagging.* Circulation, 1990. **81**(4): p. 1236-1244.
92. Buckberg, G.D., *Rethinking the cardiac helix - a structure/function journey: overview.* European Journal of Cardio-Thoracic Surgery, 2006. **29**: p. S2-S3.
93. Tang, J., et al., *Quantitative study of cardiac motion estimation and abnormality classification in emission computed tomography.* Medical Engineering & Physics, 2011. **33**(5): p. 563-572.
94. Segars, W.P., et al., *4D XCAT phantom for multimodality imaging research.* Medical Physics, 2010. **37**(9): p. 4902-4915.
95. Thielemans, K., et al., *STIR: software for tomographic image reconstruction release 2.* Physics in Medicine and Biology, 2012. **57**(4): p. 867-883.
96. Hellier, P. and C. Barillot. *Cooperation between local and global approaches to register brain images*. in *Information Processing in Medical Imaging*. 2001. Springer.
97. Cachier, P., et al. *Multisubject non-rigid registration of brain MRI using intensity and geometric features*. in *Medical Image Computing and Computer-Assisted Intervention–MICCAI 2001*. 2001. Springer.

98. Kybic, J. and M. Unser, *Fast parametric elastic image registration.* Ieee Transactions on Image Processing, 2003. **12**(11): p. 1427-1442.

99. Chen, C.L., et al., *Integration of SimSET photon history generator in GATE for efficient Monte Carlo simulations of pinhole SPECT.* Medical Physics, 2008. **35**(7): p. 3278-84.

100. Harrison, R.L., et al. *Preliminary Experience With The Photon History Generator Module Of A Public-domain Simulation System For Emission Tomography*. in *Nuclear Science Symposium and Medical Imaging Conference, 1993., 1993 IEEE Conference Record.* 1993.

101. Jan, S., et al., *GATE: a simulation toolkit for PET and SPECT.* Physics in Medicine and Biology, 2004. **49**(19): p. 4543-61.

102. Chen, C.L., et al., *Integration of SimSET photon history generator in GATE for efficient Monte Carlo simulations of pinhole SPECT.* Medical Physics, 2008. **35**(7): p. 3278-3284.

CURRICULUM VITAE

JIZHE WANG

Birth date and place: January 31, 1991, Henan, China, P.R.

500 W University Parkway, APT 5L · Baltimore, MD 21210
(443)-924-9968(c)
wangjizhe0702@gmail.com

EDUCATION

Johns Hopkins University, Baltimore, MD, USA, 2016
Ph.D. in Engineering, Electrical and Computer Engineering Department, 2016
Area of Specialization: Medical Imaging Physics. *Advisor: Dr. Benjamin M.W. Tsui*
M.S. in Engineering, Electrical and Computer Engineering Department, 2013

Zhejiang University, Hangzhou, Zhejiang, China, P.R., 2011
"Engineering +English" Double-Degree Program, Chu Kochen Honors College
B. E. in Automation, College of Electrical Engineering
B. A. in English, College of Foreign Language Culture and International Communication

RESEARCH EXPERTISE AND INTERESTS

My areas of expertise are imaging science and imaging physics of multiple modalities including CT, PET, SPECT and MR, data-driven respiratory and cardiac gating, motion estimation, motion compensation, Monte Carlo simulation, and cardiac motion modeling.
I am also interested in:
– System design/modeling and simulation
– Kinetic modeling
– Quantitative reconstruction and image correction methods
– Tracer evaluation

RESEARCH EXPERIENCE

Division of Medical Imaging Physics, Department of Radiology
Johns Hopkins University, 2011 - 2016
Research Assistant, *Supervisor: Dr. Benjamin M.W. Tsui*

Feature-guided cardiac motion estimation for gated cardiac PET imaging, 2011 - 2016

- Designed methods to extract unique anatomical features of human heart such as the interventricular sulcus and papillary muscles from cardiac PET images
- Created realistic cardiac motion model based on clinical observation of cardiac motion to describe spatial variation of radial, circumferential and longitudinal motion of human heart
- Developed optical-flow based cardiac motion estimation algorithm with motion information from anatomical features and cardiac motion model, which achieved more

accurate estimation of three cardiac motion components than traditional optical flow algorithm in simulation study

Motion compensation for list-mode cardiac PET data with Philips Healthcare, 2014 - 2016

- Developed advanced data-driven respiratory gating methods for TOF list-mode cardiac PET data and improved respiratory motion signal quality
- Validated the respiratory motion signal by data-driven methods with signal from external device
- Implemented data-driven respiratory gating and dual respiratory and cardiac motion compensation for dual gated cardiac images

Evaluation of the imaging performance of a novel prostate scanner developed by ProxiScan®, 2011

- Designed and implemented experiments to evaluate the performance of the scanner in terms of system resolution and sensitivity

TECHNICAL SKILLS AND LANGUAGE

Computer skills: MALAB, C/C++, Python, JAVA, EndNote, Linux, ImageJ, MIPAV, Shell scripts

Familiar with simulation software packages: GATE (Geant4 Application for Tomographic Emission) and STIR (Software for Tomographic Image Reconstruction)

Language: Fluent in English and Chinese

JOURNAL PUBLICATIONS AND MANUSCRIPTS

1. Tao Feng, **Jizhe Wang**, George Fung, and Benjamin Tsui. "Non-rigid dual respiratory and cardiac motion correction methods after, during, and before image reconstruction for 4D cardiac PET." Physics in medicine and biology61, no. 1 (2015): 151.

2. Tao Feng, **Jizhe Wang**, and Benjamin MW Tsui. "Theory and realization of a 2D high resolution and high sensitivity SPECT system with an angle-encoding attenuator pattern." Physics in medicine and biology 61.7 (2016): 2730.

3. **Jizhe Wang**, Jingyan Xu, Tao Feng and Benjamin M.W. Tsui. "Development and evaluation of a new data-driven respiratory motion signal extraction method for list-mode cardiac PET data with TOF information". Manuscript in preparation.

4. **Jizhe Wang**, George S.K. Fung, Tao Feng, Benjamin M.W. Tsui, "Development and preliminary implementation of a feature-guided cardiac motion estimation method". Manuscript in preparation.

CONFERENCE PAPERS

1. **Jizhe Wang**, Tao Feng, Benjamin M.W. Tsui, "Development and Evaluation of Data-Driven Respiratory Gating Methods with Simulated List-Mode PET Data" *2015 IEEE Nuclear Science Symposium and Medical Imaging Conference (NSS/MIC)*, San Diego, CA, 2015.

2. **Jizhe Wang**, Lingzhi Hu, Tao Feng, Jingyan Xu, Lingxiong Shao and B. M. W. Tsui, "Improved spatial and temporal resolution of gated myocardial perfusion PET using post

reconstruction dual respiratory and cardiac motion compensation," *2014 IEEE Nuclear Science Symposium and Medical Imaging Conference (NSS/MIC)*, Seattle, WA, 2014, pp. 1-4. doi: 10.1109/NSSMIC.2014.7430789

3. **Jizhe Wang**, G. S. K. Fung, T. Feng and B. M. W. Tsui, "An interventricular sulcus guided cardiac motion estimation method," *2013 IEEE Nuclear Science Symposium and Medical Imaging Conference (2013 NSS/MIC)*, Seoul, 2013, pp. 1-7. doi: 10.1109/NSSMIC.2013.6829054

4. **Jizhe Wang**, George S. K. Fung; Tao Feng; Benjamin M. W. Tsui, "A papillary muscle guided motion estimation method for gated cardiac imaging", *Proc. SPIE 8668, Medical Imaging 2013: Physics of Medical Imaging, 86682G (19 March 2013)*, doi:10.1117/12.2007505

CONFERENCE PRESENTATIONS

1. **Jizhe Wang**, Tao Feng, and Benjamin M.W. Tsui, "A new cardiac motion vector field estimation method based on the optical-flow method with additional constraint from motion of an anatomical feature in 4D cardiac PET", Oral presentation in SNMMI 2016.

2. **Jizhe Wang**, and Benjamin M.W. Tsui, "A B-spline Based Cardiac Feature Extraction Method", Oral presentation in SNMMI 2016.

3. **Jizhe Wang**, Tao Feng, Benjamin M.W. Tsui, "Development and Evaluation of Data-Driven Respiratory Gating Methods with Simulated List-Mode PET Data", Poster presentation in NSS/MIC IEEE 2015.

4. Tao Feng, **Jizhe Wang**, Benjamin M.W. Tsui, "Development and Evaluation of Four PET Image-Based Dual Respiratory and Cardiac Motion Estimation Methods", Oral presentation in NSS/MIC IEEE 2015.

5. Benjamin M. Tsui, Jingyan Xu, **Jizhe Wang**, Tao Feng, M. R. Abraham, Stefan L. Zimmerman, Thomas H. Schindler, "Extraction of Cardiac Motion and Myocardial Contractility from 4D Cardiac PET Images", Oral presentation in SNMMI 2015.

6. **Jizhe Wang**, Tao Feng, Jingyan Xu, Amy E. Perkins, Benjamin M. Tsui, "An improved data-driven method for respiratory motion signal detection and magnitude estimation from noisy list-mode cardiac PET data", Oral presentation in SNMMI 2015.

7. **Jizhe Wang**, Lingzhi Hu, Tao Feng, Jingyan Xu, Lingxiong Shao, Benjamin M. W. Tsui, "Improved spatial and temporal resolution of gated myocardial perfusion PET using post reconstruction dual respiratory and cardiac motion compensation", Poster presentation in NSS/MIC IEEE 2014.

8. **Jizhe Wang**. George, S.K. Fung, Tao Feng, Benjamin M.W. Tsui, "An interventricular sulcus guided cardiac motion estimation mssethod", Oral presentation in NSS/MIC IEEE 2013.

9. Tao Feng, George S.K. Fung, Jingyan Xu**, Jizhe Wang**, Benjamin Tsui, "Maximum likelihood based joint 4D motion vector field estimation and image reconstruction in 4D PET", Oral presentation in SNMMI 2013.

10. **Jizhe Wang**, George S.K. Fung, Tao Feng, Benjamin Tsui, "A feature guided cardiac motion estimation method in PET", Oral presentation in SNMMI 2013.

11. **Jizhe Wang**, George S. K. Fung, Tao Feng, Benjamin M. W. Tsui, “A papillary muscle guided motion estimation method for gated cardiac imaging”, Poster presentation in SPIE 2013.